

CONTENTS

Wojciech Horak, Marcin Szczęch, Bogdan Sapiński <i>Magnetorheological Fluids Behavior in Oscillatory Compression Squeeze: Experimental Testing And Analysis</i>	221
Arkadiusz Trąbka <i>Effect of Pulse Shape and Duration on Dynamic Response of a Forging System</i>	226
Kamil Krasuski, Stepan Savchuk <i>The Impact of Troposphere Correction for Designation of the Ellipsoidal Height of Aircraft at Approach to Landing Procedure ...</i>	233
Heorhiy Sulym, Iaroslav Pasternak, Mariia Smal, Andrii Vasylyshyn <i>Mixed Boundary Value Problem for an Anisotropic Thermoelastic Half-Space Containing Thin Inhomogeneities</i>	238
Krzysztof L. Molski <i>Stress Concentration at Load-Carrying Fillet Welded Cruciform Joints Subjected to Tensile and Bending Loads</i>	245
Heorhiy Sulym, Nataliia Ilchuk, Iaroslav Pasternak <i>Heat Conduction in Anisotropic Medium with Perfectly Conductive Thread-Like Inclusions</i>	251
Krzysztof Wałęsa, Ireneusz Malujda, Dominik Wilczyński <i>Shaping the Parameters of Cylindrical Belt Surface in the Joint Area</i>	255
Olga Porkuian, Vladimir Morkun, Natalia Morkun, Oleksandra Serdyuk <i>Predictive Control of the Iron ore Beneficiation Process Based on the Hammerstein Hybrid Model</i>	262
Dariusz Szpica, Michal Korbut <i>Modelling Methodology of Piston Pneumatic Air Engine Operation</i>	271
<i>Abstracts</i>	279

MAGNETORHEOLOGICAL FLUIDS BEHAVIOUR IN OSCILLATORY COMPRESSION SQUEEZE: EXPERIMENTAL TESTING AND ANALYSIS

Wojciech HORAK*, Marcin SZCZECH*, Bogdan SAPIŃSKI**

*Faculty of Mechanical Engineering and Robotics, Department of Machine Design and Technology, AGH University of Science and Technology, al. Mickiewicza 30, 30-059 Cracow, Poland

** Faculty of Mechanical Engineering and Robotics, Department of Process Control, AGH University of Science and Technology, al. Mickiewicza 30, 30-059 Cracow, Poland

horak@agh.edu.pl, szczech@agh.edu.pl, deep@agh.edu.pl

received 2 October 2019, revised 6 November 2019, accepted 5 December 2019

Abstract: This article deals with experimental testing of magnetorheological fluid (MRF) behaviour in the oscillatory squeeze mode. The authors investigate and analyse the influence of excitation frequency and magnetic field density level on axial force in MRFs that differ in particle volume fraction. The results show that, under certain conditions, the phenomenon of self-sealing can occur as a result of the magnetic field gradient and a vacuum in the working gap of the system.

Key words: magnetorheological fluid, oscillatory compression, magnetic field, squeeze force

1. INTRODUCTION

Magnetorheological fluids (MRFs) are non-uniform suspensions of micro-sized ferromagnetic particles in the carrier fluid. In engineering applications, hydrocarbon or silicon oil bases are primarily used as carrier fluids. Owing to the magnetic properties of these materials, it is possible to control their rheological parameters by interacting with an external magnetic field. MRFs are used in applications with controlled characteristics, such as vibration dampers, brakes and clutches (Chengye et al., 2011; Farjoud et al., 2008; Guldbakke and Hesselbach, 2006; Kubik et al., 2017). Depending on the type of device, four basic modes of MRF operation can be distinguished: shear mode and valve mode, the essence of which is shear excitation; gradient pinch mode (Goncalves and Carlson, 2009), which is similar to valve flow but at a highly non-uniform magnetic field; and compression mode, in which a complex state of deformation occurs. The compression mode is characterised by the possibility of obtaining significant forces at very small displacements (at a maximum of about a few millimetres). Stresses obtained in MRF when squeezed may approach up to 200 kPa (Tao, 2011). This feature can be advantageous for the development of new MR (magnetorheological) devices, especially dampers (Liu et al., 2019), mounts (Farjoud et al., 2011; Goldasz and Sapiński, 2011) and bearings (Guldbakke and Hesselbach, 2006), for which the ability to generate large forces and to provide a wide variability range of the performance parameters are of particular importance. Analysis of the MRF squeeze working condition is a complex issue. This is primarily due to the large number of factors affecting the process, that is, squeeze-strengthening effect (Liu et al., 2019; Wang et al., 2019), clumping effect or aggregation of MRF particles (Farjoud et al., 2008; Farjoud et al., 2011), complex deformation state (Horak, 2018; Laun et al., 2008), displaced carrier fluid from the squeeze zone (Laun et al., 2008; Szczech and Horak, 2017),

pressure generated in the MRF under the action of the applied magnetic field (Guo et al., 2012; Horak, 2018), the cavitation effects (Kuzhir et al., 2008) and the complex force progression during the compression process (Guo et al., 2013; Gstöttenbauer et al., 2008; Horak, 2018).

The present article summarises the experimental results and analysis of three MRFs differing in composition, operated in the oscillatory squeeze mode with a constant volume. The purpose of the experiments was to determine the behaviour of MRFs at variable excitation frequencies and magnetic field density. Attention has been paid to the influence of spatial magnetic field distribution on the variability of the value as well as the direction of the squeeze force.

2. CHARACTERISATION OF INVESTIGATED MAGNETORHEOLOGICAL FLUIDS

In this article, we present the results of laboratory tests on the behaviour of selected MRFs operating in the oscillatory compression mode with a constant sample volume.

Tab. 1. Properties of tested MRFs

	Unit	MRF-18	MRF-22	MRF-27
Magnetic particle (by volume)	(%)	18.3	22	27.5
Dynamic viscosity ($T_v = 25^\circ\text{C}$, $B = 0\text{T}$, $\dot{\gamma} = 100\text{ s}^{-1}$)	(mPa·s)	80.1	130	276
Density	(g/cm ³)	2.137	2.312	2.702
Saturation magnetisation	(kA/m)	~220	~270	~360

Three fluids produced based on oil (hydrocarbon), differing in the content of ferromagnetic particles, were investigated. The MRF-22 is a commercially available fluid marked MRF-122 by Lord Co.; the other two fluids have been obtained by adding or subtracting the base oil to specific samples. Selected physical properties of these fluids are presented in Table 1, and the magnetisation curves are shown in Figure 1. The names of the examined fluids express the volumetric percentage of magnetic particles.

Increasing the amount of ferromagnetic particles in the MRF primarily results in increased magnetisation of saturation. Between MRF-18 and MRF-22, there is a 23% difference in magnetic saturation, and between MRF-18 and MRF-27, the difference is 64%. In addition, the examined fluids differ significantly in their zero-field viscosity. Between MRF-18 and MRF-27, there is a nearly 3.5-fold difference in this parameter.

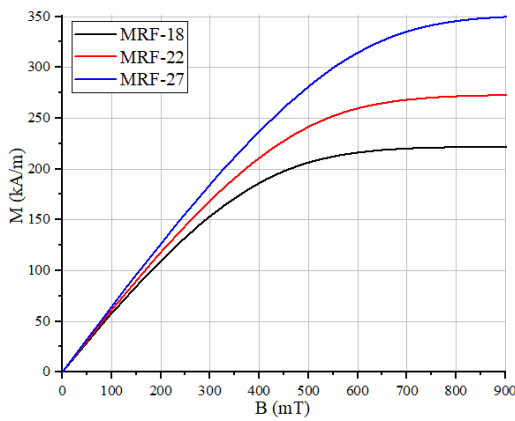


Fig. 1. Magnetisation versus magnetic field density of tested MRFs

In the magnetic field density up to the range of approximately $B = 400$ mT, all the tested MRFs have an approximate linear $M = f(B)$ characteristic. It can also be noted that in the analysed range of magnetic field density ($B < 670$ mT), only MRF-18 and MRF-22 should reach the saturation state.

3. EXPERIMENTS

Experiments were conducted in the specially designed experimental setup (Fig. 2a) consisting of a frame (1) supporting a linear servomotor (7), allowing the main position of the measuring system to be changed.

The oscillatory movement of the upper plate (4) is generated by a connecting rod (8) mounted on a cranked shaft (9), driven by a rotary servomotor (11) with timing belt transmission (10). The range of the oscillating plate movement is determined by the crank value 'e'. The force sensor (6) used for measuring the tensile and compression forces is attached to the shaft supported by two linear bearings (5). The position of the movable plate is measured by a non-contact laser sensor (3).

The MRF sample is placed inside the test cell (2) (Fig. 2b) directly above an electromagnet core (17) between a movable plate made of a paramagnetic material (4). The stationary plate (14) is made of a paramagnetic material and reduces ejection of the MRF from the gap. The magnetic circuit is closed by the cell housing (13, 15). The magnetic flux density in the measuring gap is altered by the current in the electromagnet coil (16). In the

electromagnet core and in the cell housing, ducts for the coolant were made. This ensures the temperature stabilisation of the system. All experiments were conducted at the constant temperature of 25°C. The diameter of the movable plate d_p was 50 mm, whereas the diameter of the electromagnet core d_c was 45 mm (see Fig. 2c), initial gap height h was 2 mm and the range of motion of the movable plate Δh was 1 mm (compression rate, $\epsilon = 0.5$).

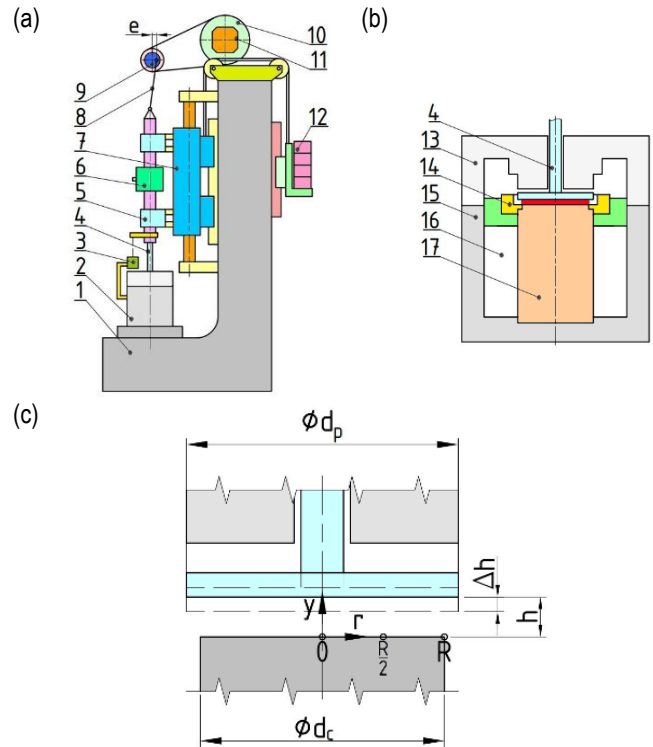


Fig. 2. Schematic diagram: (a) experimental setup, (b) test cell and (c) test geometry

3.1. Scenario

The distribution of the magnetic field density in the working gap was measured by using a teslameter at three points on the diameter of the electromagnet core front face for $r = 0, R/2$ and R (see Fig. 2c); the measurement results are presented in Figure 3a.

Near the symmetry axis of the system, lower magnetic field density occurs than at the edge of the analysed geometry. For a more detailed investigation of magnetic field spatial distribution, a numerical simulation was carried out by using the finite element method. Figure 3b compares the measurement and numerical simulation results ($I = 2$ A, dashed line marked in Fig. 3a). A good convergence of simulation to measurement was obtained, with the results presented in Figure 3a also consistent with the analyses presented in Figure 3b. More detailed information about the magnetic field spatial distribution is presented in Szczęch and Horak (2017). The curves of magnetic field density versus current measured at three points are shown in Figure 3b. Owing to the occurrence of the magnetic field density gradient, it should be expected that the higher B values near the edge of the electromagnet core may result in the self-sealing effect of the system (Szczęch and Horak, 2017).

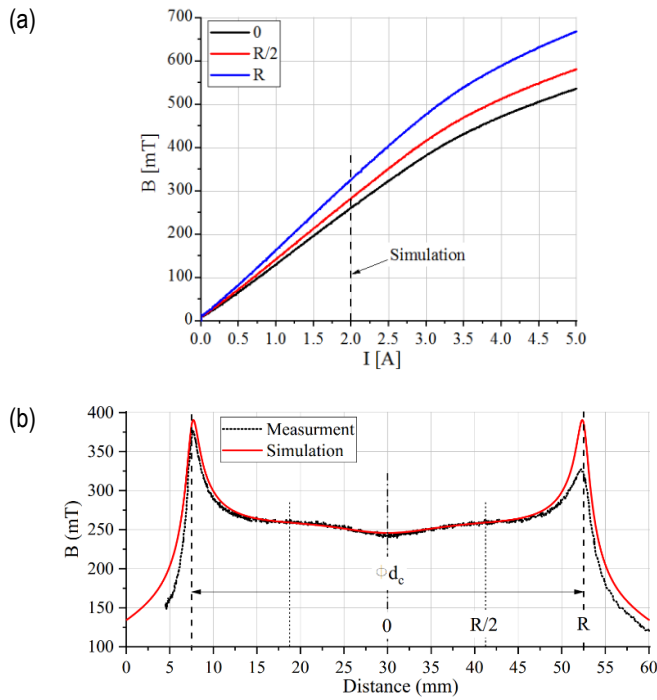


Fig. 3. (a) Magnetic field density versus current measured at three points of the electromagnet core face and (b) distribution of the magnetic field density across the bottom measuring plate

The study was based on measuring the force exerted by the MRF on an oscillatory moving plate during the increase in the magnetic flux density in the range of $B = 0$ to 670 mT (corresponding to the power supply current of the electromagnet $I = 0$ –5 A). A linear ramp of the current was set for 180 s. Each experiment has been carried out at five extortion frequencies $f = 0.1, 0.5, 1, 2$ and 3 Hz. Tests were performed for a constant MRF volume, $V = 1$ mL, which corresponds to the filling rate of the working gap 63% (calculated in relation to $h_{min} = 1$ mm).

4. RESULTS AND DISCUSSION

The study concerns a comparative analysis of MRFs behaviour. The aim of the study was to determine the range of force variation observed when MRFs are subjected to extortion by oscillatory compression. An example of the measurement result with a determined upper and lower force envelope is shown in Figure 4. The negative sign of the forces indicates that the MRF is in the compression phase, and the positive sign of force refers to the case when the MRF resists the moving plate upwards.

The graphs of maximum compression forces (lower envelopes) of the tested MRFs are presented in Figure 5. For all the tested fluids up to approximately $I = 1$ A (i.e. $B = 150$ mT), no significant influence of the composition of samples or the oscillation frequency on the value of the compression force is observed. For higher electromagnet current values, higher forces are obtained for fluids with a higher particle content. The lowest values of compression force are observed for MRF-18 (up to about 365 N) for fluids with higher magnetisation values (MRF-22 and MRF-27) 450 N and 605 N, respectively. A directly proportional relationship between the value of magnetisation of the fluid magnetisation saturation and the observed maximum compression force is visible.

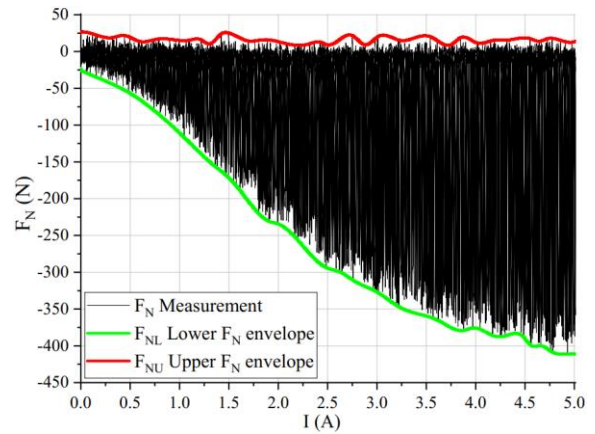


Fig. 4. Sample measurement result with marked upper and lower envelopes (MRF-22, $f = 1$ Hz)

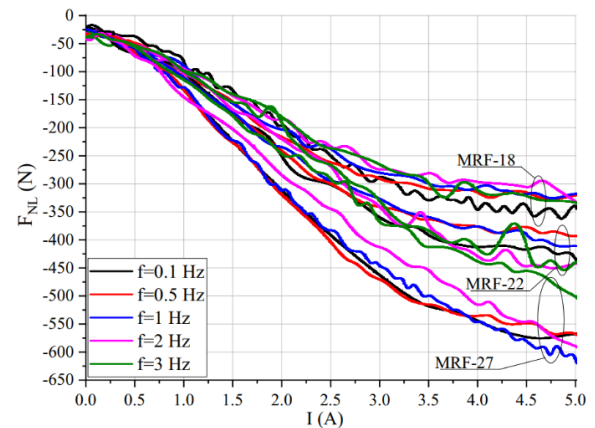


Fig. 5. Lower measured force envelopes F_{NL} versus current I

The graphs of maximum 'tensile' forces (upper envelopes) of the tested MR liquids are shown in Figure 6. For all the tested liquids for $I < 1.5$ A ($B < 250$ mT), no significant influence of the frequency and composition of the tested fluids on the measured force is observed. Negative sign force values are observed at the lowest oscillation frequency ($f = 0.1$ Hz) and for $I > 2.5$ A ($B > 400$ mT), indicating that, in this case, the MRF 'pushes' the movable measuring plate out also during the return motion. This may be related to the magnetostatic pressure (Horak et al., 2017; Liu et al., 2019; Mazlan, 2007), which may be related to the influence of columnar structures of magnetic particles on the measuring plate in this case. In the case of the MRF-18 and MRF-22 samples, no significant differences in the measured force were observed (approximately $F_{NLmax} = -17$ N), whereas for fluids with the highest number of particles, double force ($F_{NLmax} = -34$ N) was obtained.

In each of the analysed cases, the increase in frequency to 0.5 and 1 Hz resulted in stabilisation of the measured force. Under these test conditions, there is no significant effect of a change in the magnetic field strength on the measured force. The observed positive values of the force (about 20 N) result from the inertia of the measuring system. Preliminary tests carried out without MRF showed the occurrence of forces of up to approximately 15 N.

In the case of force frequency $f = 2$ and 3 Hz and the current intensity $I > 2.5$ A ($B > 400$ mT), significant force values with a positive return can be observed. The value of the force increases as the oscillation frequency increases. This phenomenon is visible in all tested fluids. The occurrence of this may be associated with

a vacuum inside the working gap of the measuring system.

The maximum force was observed for MRF-22, $F_{NUmax} = 94 \text{ N}$, which indicates the pressure of about $p = 60 \text{ Pa}$. This effect can be compared to that which occurs in magnetic fluid seals. The presence of a magnetic field gradient on the edge of the core (see Fig. 3c) may result in the formation of a tight barrier from the MRF between the surface of the electromagnet core and the surface of the moving plate. It should be noted that the values of positive forces are so large that they should be considered when developing devices working in the discussed working conditions.

In Figure 7, graphs of measured force values of (F_N) as a function of displacement of a moving plate (Δh) are presented. In the case of $f = 0.1 \text{ Hz}$, relatively high values of the compression force can be observed for the initial position of the movable plate ($\Delta h = 0 \text{ mm}$). In this case, the maximum force value was around $F_N = -100 \text{ N}$. Similarly, for $f = 0.5 \text{ Hz}$, this force is noticeable and is around $F_N = -50 \text{ N}$. This behaviour can be explained by the influence of the internal structure of the MRF on the measuring plate. With an increase in the oscillation frequency, the value of this force decreases.

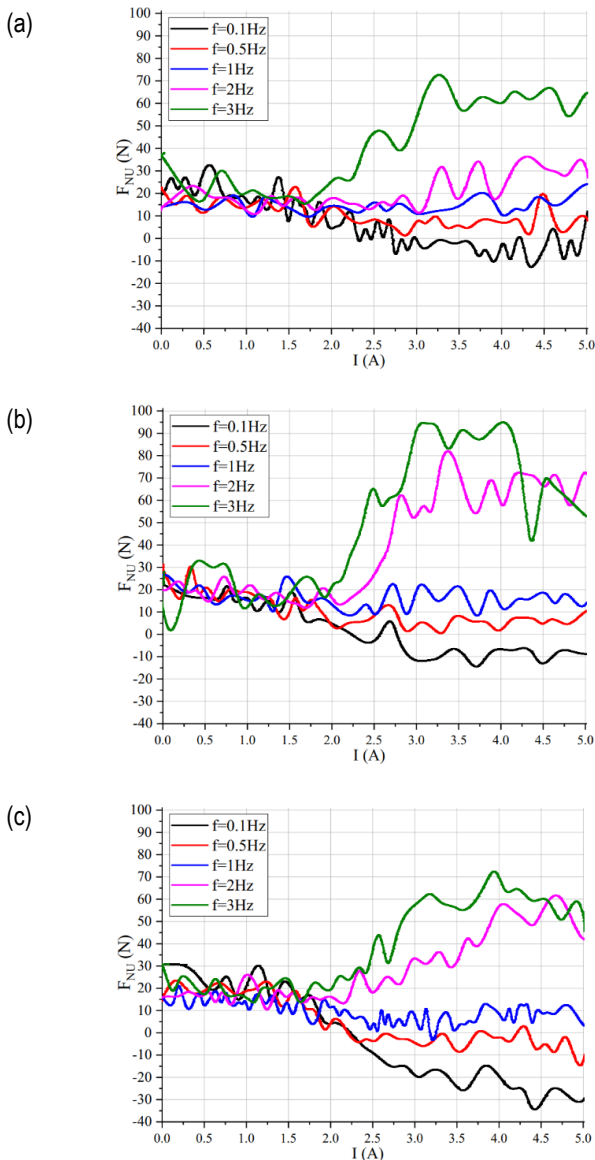


Fig. 6. Upper measured force envelopes F_{NU} versus current I , (a) MRF-18, (b) MRF-22 and (c) MRF-27

For $f \geq 1 \text{ Hz}$, the force in the initial compression phase does not change as the frequency increases. In addition, there are no noticeable differences in the measured compression force for individual MRFs with a low compression rate (ϵ). In Figure 7d and e, areas of positive force values are visible. It can be noticed that the area of its occurrence covers the range of movement of the plate from $\Delta h = 0.95$ to 0.7 mm . Therefore, the vacuum occurs only in the case of a significant degree of compression of the tested fluids (0.95 at the beginning and 0.7 at the end).

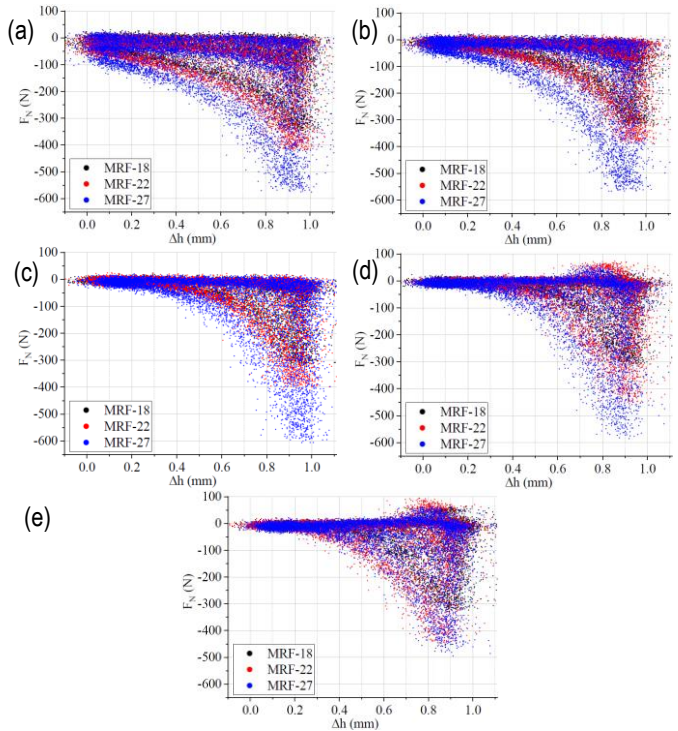


Fig. 7. Measured force F_N versus Δh , (a) $f = 0.1 \text{ Hz}$, (b) $f = 0.5 \text{ Hz}$, (c) $f = 1 \text{ Hz}$, (d) $f = 2 \text{ Hz}$ and (e) $f = 3 \text{ Hz}$

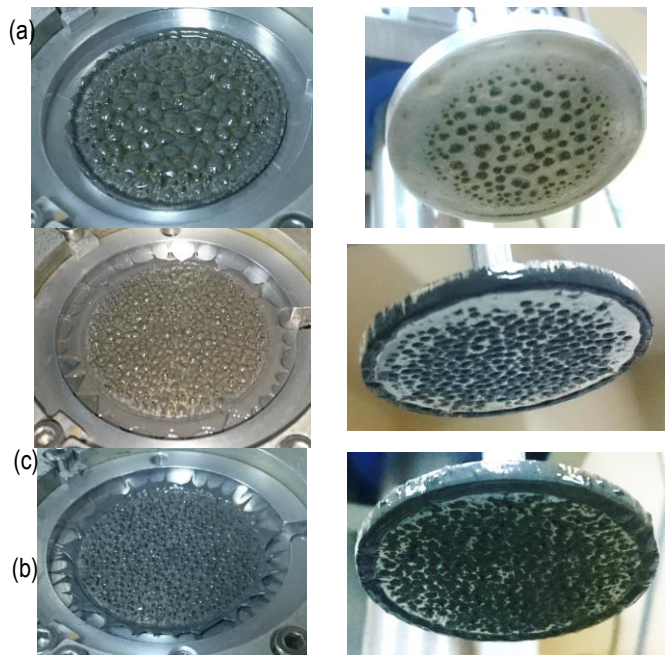


Fig. 8. Photographs of the MRFs after the test; (a) MRF-18, (b) MRF-22 and (c) MRF-27

The photographs also show a change in the structure of the tested fluids, depending on their composition. For the fluid with the lowest content of particles (MRF-18, Fig. 8a), the base fluid precipitations are clearly visible. The concentrations of the MRF are smaller and more dispersed with higher content of magnetic particles (cf. Fig. 8a, b and c).

5. CONCLUSIONS

The results of the experiments and their analysis lead us to the following conclusions:

- The maximum compressive force is obtained for the greatest displacement and is related to the number of magnetic particles and, thus, to the magnetisation curve of the MRF. The volumetric percentage of particles in the carrier fluid can be used as an indicator to estimate the ability of MRF to produce normal compression force.
- The increase in the compression force as a function of displacement is similar to an exponential shape, with the increase in the compression frequency causing the rate of increase to be lower in the range $\Delta h = 0$ to 0.3 mm, probably because of the ability to change the internal structure of the particles in the MRF as a result of the deformation. It should be noted that the lower frequency favours the creation of structures.
- Static force is visible in the low enforcement frequency range (up to 0.5 Hz). This process is described in detail in Horak et al. (2017) and Horak (2018).
- In the analysed case, the increase in the compression frequency and magnetisation of saturation encourages the movement of fluids outside the working gap (Fig. 8). This effect was observed only at the frequency of 3 Hz, and the loss of the liquid constituted about 8% of the applied volume.
- Significant ‘tensile’ forces on the MRF can be generated in the analysed system. This phenomenon may be related to the phenomenon of self-sealing of the measurement gap because of the magnetic field gradient. The result is a vacuum in the working gap of the system. This phenomenon is visible only at higher frequencies of oscillations, that is, from 2 Hz. In addition, positive forces occur only in the case of a significant degree of MRF compression ($\Delta h = 0.95\text{--}0.7$ mm).

REFERENCES

1. **Chengye L., Fengyan Y., Kejun J.** (2011), Design and finite element analysis of magnetic circuit for disk MRF brake, *Advanced Materials Research*, 181-182, 22–527.
2. **Farjoud A., Vahdati N., Fah Y.** (2008), MR-fluid yield surface determination in disc-type MR rotary brakes, *Smart Materials and Structures*, 17(3), 1–8.
3. **Farjoud A., Craft M., Burke W., Ahmadian M.** (2011), Experimental investigation of MR squeeze mounts, *Journal of Intelligent Material Systems and Structures*, 22, 1645–1652.
4. **Guo C., Gong X., Xuan S., Zong L and Peng C.** (2012), Normal forces of magnetorheological fluids under oscillatory shear, *J. Magn. Mater.*, 324, 1218.
Guo C., Gong X., Xuan S., Yan Q. and Ruan X. (2013), Squeeze Squeeze behavior of magnetorheological fluids under constant volume and uniform magnetic field, *Smart Materials and Structures*, 22(4), 045020.
6. **Gstöttenbauer N., Kainz A., Manhartgruber B.** (2008), Experimental and numerical studies of squeeze mode behaviour of magnetic fluid, Proc. IMechE Part C, *J. Mechanical Engineering Science*, 222(12), 2395-2407
7. **Guldbakke J. M., Hesselbach, J.** (2006), Development of bearings and a damper based on magnetically controllable fluids, *J. Phys., Condens. Matter*, 18(38), 2959–2972.
8. **Goldasz J., Sapiński B.** (2011), Model of a squeeze mode magnetorheological mount, *Solid State Phenomena*, 177, 116–124.
9. **Goncalves F.D., Carlson J.D.** (2009) An alternate operation mode for MR fluids – magnetic gradient pinch, *Journal of Physics, Conference Series*, 149(1), 012050.
10. **Horak W. Sapiński B., Szczęch M.** (2017), Analysis of force in MR fluids during oscillatory compression squeeze, *Acta Mechanica et Automatica*, 11 (1), 64–68.
11. **Horak W.** (2018) Modeling of magnetorheological fluid in quasi-static squeeze flow mod, *Smart Materials and Structures*, 27 (6), 065022.
12. **Kubík M., Macháček O., Strecker Z., Roupec, J, Mazúrek I.** (2017), Design and testing of magnetorheological valve with fast force response time and great dynamic force range, *Smart Material and Structures*, 26(4), 047002.
13. **Kuzhir P., López-López M. T., Vertelov G., Pradille C., Bossis G.** (2008), Oscillatory squeeze flow of suspensions of magnetic polymerized chains, *J. Phys., Condens. Matter*, 20204132.
14. **Laun H.M., Gabriel C., Schmidt G.** (2008), Primary and secondary normal stress differences of a magnetorheological fluid (MRF) up to magnetic flux densities of 1 T, *Journal of Non-Newtonian Fluid Mechanics*, 148(1), 47-56.
15. **Liu W., Luo Y., Yang B., Lu W.** (2019), Design and Mechanical Model Analysis of Magnetorheological Fluid Damper, *American Journal of Mechanics and Applications*, 4(1), 15-19.
16. **Mazlan S.** (2007), The performance of magnetorheological fluid in squeeze mode, *Smart Materials and Structures*, 16(5), 1678-1682.
17. **Szczęch M., Horak W.** (2018), Analysis of the magnetic field distribution in the parallel plate rheometer measuring system, *Tribologia*, 49(2), 117-122.
18. **Tao R.** (2011), Super-strong magnetorheological fluids, *Journal of Physics: Condensed Matter*, 13(50), 979–999.
19. **Wang N., Liu X., Zhang X.,** (2019), Squeeze-Strengthening Effect of Silicone Oil-Based Magnetorheological Fluid with Nanometer Fe₃O₄ Addition in High-Torque Magnetorheological Brake, *Journal of Nanoscience and Nanotechnology*, 1, 19(5), 2633-2639.
20. **Zhang X. J., Farjud A., Ahmadian M., Guo K. H., Craft M.** (2011), Dynamic Testing and Modelling of an MR Squeeze Mount, *Journal of Intelligent Material Systems and Structures*, 22, 1717-1728.

This work is supported by AGH University of Science and Technology under research programs No. 16.16.130.942.

EFFECT OF PULSE SHAPE AND DURATION ON DYNAMIC RESPONSE OF A FORGING SYSTEM

Arkadiusz TRĄBKA*

*Faculty of Mechanical Engineering and Computer Science, Department of Engineering Fundamentals,
 University of Bielsko-Biala, ul. Willowa 2, 43-309 Bielsko-Biala, Poland

atrabka@ath.bielsko.pl

received 26 June 2018, revised 6 December 2019, accepted 10 December 2019

Abstract: Forging hammers are machines whose operation causes negative effects both at the place of their foundation (the soil settlement) and in their surroundings (e.g., vibrations propagating to the other devices, noise, etc.). Knowledge of the parameters characterizing the time history of the force that arises as a result of impact of a ram on a shaped material is of fundamental importance for the correct analysis of both the structure of the hammer and its impact on the surroundings. In the paper, the effect of the shape and duration of a pulse load on the dynamic response of a hammer-foundation forging system was assessed. An analytical method of description of the forces that arise as a result of impact of the ram on the forged material, using different forms of pulses was presented. The forces defined in this way as loads in a mathematical model of three degrees of freedom forging system were used. The equations of motion derived from d'Alembert's principle were solved numerically in the Matlab program. The analyses for eight forms of the pulse loads with the same pulse sizes but different durations were performed. The results in the graphs were presented. It was found, among other things, that a greater impact on the maximum displacement, velocity and acceleration of each component of the hammer-foundation system as well as on the maximum forces transmitted to the soil has the duration of a pulse than its shape.

Key words: Dynamic response, impact load, pulse shape, pulse duration, forging hammer

1. INTRODUCTION

Forging hammers are impact action devices. They shape materials using the energy generated before the tool touches them.

There are basically two types of forging hammers: gravity hammers and power hammers (Major, 1980). The first group includes drop hammers and single-acting steam hammers, where during the downstroke, the ram is accelerated by gravity and builds up the impact energy. The second group includes double-acting hammers, where during the downstroke, in addition to gravity, the ram is accelerated by steam or compressed air. Of these types, the power hammers are most commonly used because they can easily produce high-energy impacts.

The following basic elements can be distinguished in the general diagram of a forging hammer with high-energy impact (Fig. 1): a ram consisting of a rod and a piston 1, an upper anvil 2 and, if necessary, an upper die 3 attached to it, a frame 4 with guides 5 and the ram drive mechanism 6, an anvil block 7 with a lower anvil 8 and, if applicable, a lower die 9 attached to it.

Due to the impact nature of the action, high-energy impacts and the need to protect the environment against the negative effects of the forging hammers operation (the soil load, vibrations and noise), spring-damping elements and a foundation are placed under the anvil block. Depending on the type of foundation, the spring-damping elements placed under the anvil block may be pads made of oak beams or a hard felt, or these may be sets of viscous-spring vibro-isolators (Lipiński, 1985; Major, 1980). Nowadays, foundations are most often made either as systems of reinforced concrete structures (Fig. 2a), sometimes replaced with steel supporting structures (Fig. 6a), connected by spring-

damping elements, or as reinforced concrete foundation troughs placed directly on the soil (Fig. 2b).

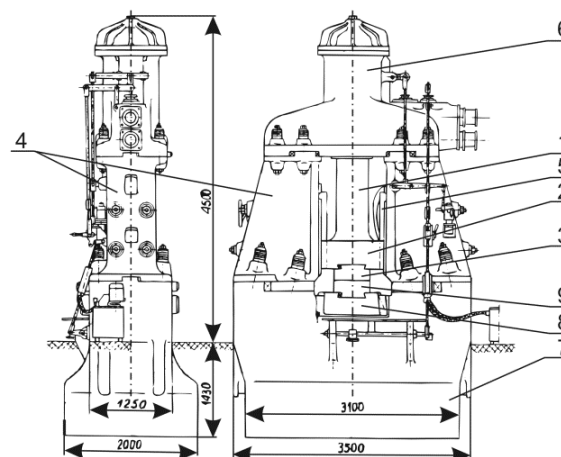


Fig. 1. Structural diagram of a forging hammer with high-energy impact (Majewski and Trąbka, 2006)

The forging process starts with the initiation of the ram movement. The ram hits the forged material at a certain velocity, causing it to deform. At the moment of the impact a part of the kinetic energy, which is accumulated in the ram, changes into the work of plastic deformation of the forged material, and the remaining unused part of the energy gives the ram a return velocity, and above all causes vibrations and elastic deformations of the anvil and foundation. Then the vibrations are transmitted through the foundation to the soil and surroundings.

The influence of the impact loads on the dynamics of forging devices, as well as the surroundings, for many years has been the subject of discussions, the results of which are presented at scientific conferences, for example, 'International Conference on Structures Under Shock and Impact', are made available as books (Altan et al., 1969; Dresig and Holzweißig, 2010; Gryboś, 1969; Harris ed. and Piersol ed., 2002; Lipiński, 1985; Major, 1980), and above all, are published as articles in scientific journals.

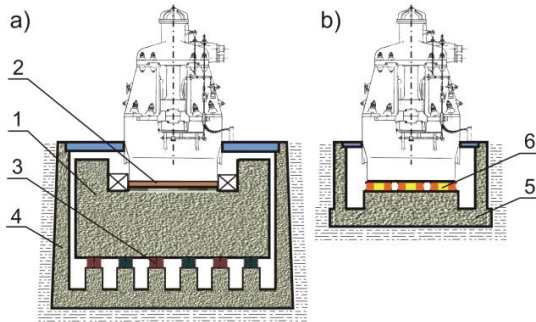


Fig. 2. Examples of foundations for forging hammers: a) a reinforced concrete foundation block 1 with a sub-anvil block pad 2 based on a spring-rubber isolation system 3 in a reinforced concrete foundation trough 4, b) a reinforced concrete foundation trough 5 placed directly on the soil with a set of viscous-spring vibro-isolators 6

Chehab and El Naggar (2003) assumed that the dynamical systems analysed by them set in motion the impact force with a rectangular pulse shape. Using the models with one and two degrees of freedom, they investigated the possibility of reducing the negative impact of the hammers on the surroundings. Leopa (2011) in turn, for a three-mass system, analysed the influence of the impact pulse duration of 0.1s, 0.03s and 0.007s, respectively, on the frequency representation of the considered load. He carried out the analyses for pulse loads of the shapes: haversine and trapezoidal. The influence of the pulse shape generated during an impact on the dynamic response of the forging hammer foundation was investigated in Prolović et al. (2004). The analyses were carried out for models with one and two degrees of freedom. The pulse loads with rectangular, trapezoidal, parabolic and semi-sinusoidal shapes were considered. The same pulse duration was assumed (0.001s). The study of the dynamic response of a one-mass model of a forging hammer both on changes in the shape of the pulse load (rectangular, semi-sinusoidal and symmetric triangular), as well as changes in its duration are presented in Chehab and El Naggar (2004). The same kind of analysis, but used in the study of the dynamics of one and two-mass models of foundations for presses, was presented in Zheng et al. (2014).

Based on the papers found, it can be seen that all processes that occur during forging depend strictly on the load transferred from the ram to the forged material. This load has the form of a pulse and is characterized by its size, shape and duration. The authors of individual papers conduct the dynamic analyses of forging processes either for the selected load durations, or one, or at most several forms of the time history of the forging force. Although in some papers, attempts of the more general analyses are undertaken (Chehab and El Naggar, 2004; Zheng et al., 2014), in relation to the hammer-foundation forging systems, it is carried out using maximally simplified models with one degree of freedom (Chehab and El Naggar, 2004).

Since among the found papers, there was no comprehensive study on the assessment of the effect of the duration and shape of

the pulse on the quantities particularly important for assessing the impact of the forging hammer on the surroundings (the maximum displacements, velocities and accelerations of the foundation and the forces transmitted to the soil), in this paper, an analysis was carried out in the above-mentioned scope. The forging system with three degrees of freedom was assessed. The analyses for eight forms of the pulse loads with the same pulse sizes but different durations were performed. The pulse durations were changed from 0.001 s to 0.2 s every 0.001 s. The dynamic responses of the forging system for unfavourable forging conditions, that is, cold forging of steel at maximum velocity were determined.

2. IMPACT LOADS

The forces that arise during the blows of the ram of the forging hammer against the forged material are the reaction of the system absorbing the impact energy to the impact load (Gryboś, 1969). These forces reach very high values and their durations τ are very short. They are referred to as the so-called pulse loads, and their size S (1) is determined as equal to the area under the curve representing the time history of the pulse load $P(t)$ (Fig. 3).

$$S = \int_0^\tau P(t)dt \quad (1)$$

where: S – the pulse size, $P(t)$ – the time history of the pulse, τ – the pulse duration.

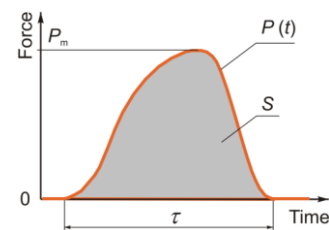


Fig. 3. Pulse load

If the pulse durations τ are extremely short, that is, satisfy the condition $\tau < 0.1 \cdot T_{min}$ (where: T_{min} is the smallest period of natural vibration of the system), they are referred to as sudden pulses (Harris ed. and Piersol ed., 2002; Lipiński, 1985). The sudden pulses are fully characterized only by their size S . In the description of this type of loads, the shapes of the force time histories are omitted. However, it is assumed that the forces act only at selected points in time (the loads are defined using the Dirac delta function).

If the pulse durations τ satisfy the condition $0.1 \cdot T_{min} \leq \tau \leq T_{max}$ (where: T_{max} is the largest period of natural vibration of the system), the pulses are called short-term (Lipiński, 1985). In this case, the response of the system is affected by the characteristics of the pulse loads. The short-term pulses are characterized by their shape, defined as the time history of the pulse $P(t)$, size S or amplitude P_m , as well as duration τ (Harris ed. and Piersol ed., 2002; Lipiński, 1985; Prolović et al., 2004).

The pulse loads resulting from the blows can take different shapes (Fig. 4). The differences between them result, among others, from the size and shape of the forged material, its temperature and mechanical properties, elastic properties of the materials used to make elements of the forging system, the contact surface geometry and the impact energy (Gryboś, 1969). A large number of factors affecting the time histories of forging forces

makes their theoretical determination very difficult, therefore, they are determined experimentally (Bieliajew and Popow, 1967).

For theoretical considerations, the real non-linear time histo-

ries of the pulses are approximated in various ways, including straight lines or trigonometric functions (Fig. 5).

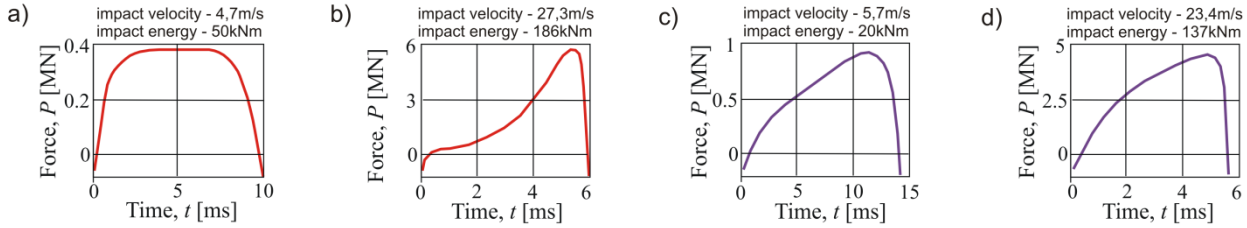


Fig. 4. Time histories of forging forces obtained experimentally by Bielajew and Popow (1967): a), b) for steel, c), d) for duralumin

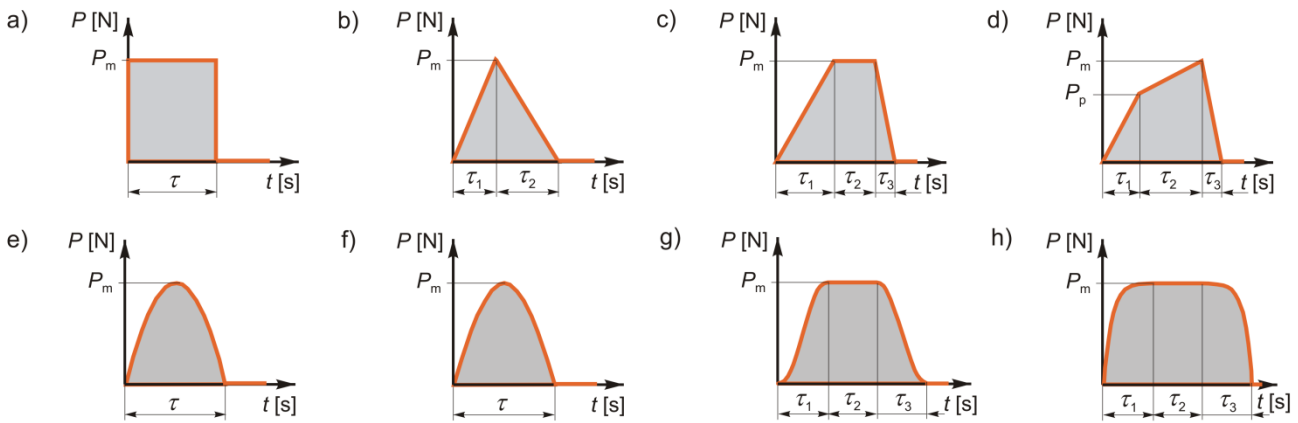


Fig. 5. Shapes of pulse loads: a) rectangular (type A), b) triangular (type B), c) trapezoidal (type C), d) triangular-trapezoidal (type D), e) parabolic (type E), f) semi-sinoidal (type F), g) versed sine-rectangular (type G), h) exponential-rectangular (type H)

The approximate time histories $P(t)$ of the pulses can be presented in analytical notation as follows:

- Rectangular pulse (Fig. 5a):

$$P(t) = \begin{cases} P_m = \frac{S}{\tau} & \text{for } 0 \leq t \leq \tau \\ 0 & \text{for } t > \tau \end{cases} \quad (2)$$

- Triangular pulse (Fig. 5b):

$$P(t) = \begin{cases} P_m \cdot \frac{t}{\tau_1} = \frac{2 \cdot S}{\tau_1 + \tau_2} \cdot \frac{t}{\tau_1} & \text{for } 0 \leq t \leq \tau_1 \\ P_m \cdot \frac{\tau_1 + \tau_2 - t}{\tau_2} = \frac{2 \cdot S}{\tau_1 + \tau_2} \cdot \frac{\tau_1 + \tau_2 - t}{\tau_2} & \text{for } \tau_1 < t \leq \tau_1 + \tau_2 \\ 0 & \text{for } t > \tau_1 + \tau_2 \end{cases} \quad (3)$$

- Trapezoidal pulse (Fig. 5c):

$$P(t) = \begin{cases} P_m \cdot \frac{t}{\tau_1} = \frac{2 \cdot S}{\tau_1 + 2 \cdot \tau_2 + \tau_3} \cdot \frac{t}{\tau_1} & \text{for } 0 \leq t \leq \tau_1 \\ P_m = \frac{2 \cdot S}{\tau_1 + 2 \cdot \tau_2 + \tau_3} & \text{for } \tau_1 < t \leq \tau_1 + \tau_2 \\ P_m \cdot \frac{\tau_1 + \tau_2 + \tau_3 - t}{\tau_3} = \frac{2 \cdot S}{\tau_1 + 2 \cdot \tau_2 + \tau_3} \cdot \frac{\tau_1 + \tau_2 + \tau_3 - t}{\tau_3} & \text{for } \tau_1 + \tau_2 < t \leq \tau_1 + \tau_2 + \tau_3 \\ 0 & \text{for } t > \tau_1 + \tau_2 + \tau_3 \end{cases} \quad (4)$$

- Triangular-trapezoidal pulse (Fig. 5d):

$$P(t) = \begin{cases} u_{P_m} \cdot P_m \cdot \frac{t}{\tau_1} & \text{for } 0 \leq t \leq \tau_1 \\ u_{P_m} \cdot P_m + (P_m - u_{P_m} \cdot P_m) \cdot \frac{t - \tau_1}{\tau_2} & \text{for } \tau_1 < t \leq \tau_1 + \tau_2 \\ P_m \cdot \frac{\tau_1 + \tau_2 + \tau_3 - t}{\tau_3} & \text{for } \tau_1 + \tau_2 < t \leq \tau_1 + \tau_2 + \tau_3 \\ 0 & \text{for } t > \tau_1 + \tau_2 + \tau_3 \end{cases} \quad (5)$$

where: $P_m = \frac{2 \cdot S}{u_{P_m} \cdot (\tau_1 + \tau_2) + \tau_2 + \tau_3}$

- Parabolic pulse (Fig. 5e):

$$P(t) = \begin{cases} 4 \cdot P_m \cdot \frac{t}{\tau} \cdot \left(1 - \frac{t}{\tau}\right) & \text{for } 0 \leq t \leq \tau \\ 0 & \text{for } t > \tau \end{cases} \quad (6)$$

- Semi-sinusoidal pulse (Fig. 5f):

$$P(t) = \begin{cases} P_m \cdot \sin\left(\pi \cdot \frac{t}{\tau}\right) & \text{for } 0 \leq t \leq \tau \\ 0 & \text{for } t > \tau \end{cases} \quad (7)$$

- Versed sine-rectangular pulse (Fig. 5g):

$$P(t) = \begin{cases} \frac{P_m}{2} \cdot \left(1 - \cos\left(\pi \cdot \frac{t}{\tau_1}\right)\right) & \text{for } 0 \leq t \leq \tau_1 \\ P_m & \text{for } \tau_1 < t \leq \tau_1 + \tau_2 \\ \frac{P_m}{2} \cdot \left(1 + \cos\left(\pi \cdot \frac{t - \tau_1 - \tau_2}{\tau_3}\right)\right) & \text{for } \tau_1 + \tau_2 < t \leq \tau_1 + \tau_2 + \tau_3 \\ 0 & \text{for } t > \tau_1 + \tau_2 + \tau_3 \end{cases} \quad (8)$$

where: $P_m = \frac{2 \cdot S}{\tau_1 + 2 \cdot \tau_2 + \tau_3}$

- Exponential-rectangular pulse (Fig. 5h):

$$P(t) = \begin{cases} P_m \cdot \frac{1 - e^{-2 \cdot \pi \cdot \frac{t}{\tau_1}}}{1 - e^{-2 \cdot \pi}} & \text{for } 0 \leq t \leq \tau_1 \\ P_m & \text{for } \tau_1 < t \leq \tau_1 + \tau_2 \\ P_m \cdot \frac{1 - e^{-2 \cdot \pi \cdot \left(1 - \frac{t - \tau_1 - \tau_2}{\tau_3}\right)}}{1 - e^{-2 \cdot \pi}} & \text{for } \tau_1 + \tau_2 < t \leq \tau_1 + \tau_2 + \tau_3 \\ 0 & \text{for } t > \tau_1 + \tau_2 + \tau_3 \end{cases} \quad (9)$$

where: $P_m = \frac{S}{\tau_1 \cdot \left(\frac{1}{1 - e^{-2 \cdot \pi}} - \frac{1}{2 \cdot \pi}\right) + \tau_2 + \tau_3 \cdot \left(\frac{1}{1 - e^{-2 \cdot \pi}} - \frac{1}{2 \cdot \pi}\right)}$

In equations (2÷9): $P(t)$ – the time history of the pulse, P_m – the pulse amplitude, u_{P_m} – the scaling factor (can take values in the range 0÷1), S – the pulse size, τ , τ_1 , τ_2 and τ_3 – the pulse durations (as indicated in Fig. 5).

The pulse amplitudes P_m can be determined based on the size of the pulses S and transformed formulas (2÷9) for the areas of the figures representing the approximate time histories of the pulses.

The pulse size S for forging, in the absence of measurement data, according to the information contained in Lipiński (1985) can be estimated based on the empirical relationship (10).

$$S = (1 + R) \cdot m_B \cdot v_B = (1 + R) \cdot m_B \cdot \sqrt{\frac{2 \cdot E_p}{m_B}} \quad (10)$$

where: m_B – the mass of the ram with the upper die block, v_B – the velocity of the ram at the moment of impact, E_p – the total energy of the impact of the hammer, R – the coefficient of restitution (the coefficient of impact elasticity). The value of R varies between 0 and 1, depending upon whether the colliding bodies are of plastic character ($R = 0$), or the impact is completely elastic ($R = 1$) (Gryboś, 1969; Lipiński, 1985; Major, 1980).

3. CONSIDERED FORGING SYSTEM

The real forging system (Fig. 6a) containing a steam-air die forging hammer MPM 16000 B – type 1, and a foundation consisting of a viscous-elastic pad 2, a steel frame 3, a viscous-spring isolation system 4 and a foundation trough 5, which rests on an elastic subsoil, was selected as the object of considerations. For the above structure, a physical model with three degrees of freedom was adopted (Fig. 6b).

Replacing the real object with the physical model, it was assumed, among other things, that the hammer, the steel frame and the foundation trough are coaxially located, non-deformable material bodies with linear relative motion. The Kelvin-Voigt body, defined by a spring and a dashpot connected in parallel, fulfils the role of constraints between the material bodies. The masses of the material bodies are concentrated in material points, while the elastic and damping constraints are considered as weightless.

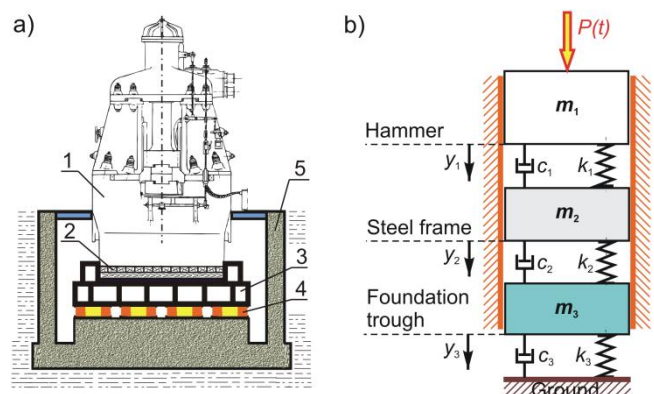


Fig. 6. a) Structural diagram of a real forging system, b) Physical model of the forging system

4. MATHEMATICAL MODEL AND ITS PARAMETERS

The mathematical model of the forging system consisting of three mass elements (Fig. 6b) was written in the form of the motion equations (11), which were derived based on the d'Alembert principle for the case of forced-damped vibrations.

$$\begin{aligned}
 m_1 \cdot \ddot{y}_1 + c_1 \cdot (\dot{y}_1 - \dot{y}_2) + k_1 \cdot (y_1 - y_2) &= P(t) \\
 m_2 \cdot \ddot{y}_2 + c_1 \cdot (\dot{y}_2 - \dot{y}_1) + k_1 \cdot (y_2 - y_1) + \\
 + c_2 \cdot (\dot{y}_2 - \dot{y}_3) + k_2 \cdot (y_2 - y_3) &= 0 \\
 m_3 \cdot \ddot{y}_3 + c_2 \cdot (\dot{y}_3 - \dot{y}_2) + k_2 \cdot (y_3 - y_2) + \\
 + c_3 \cdot \dot{y}_3 + k_3 \cdot y_3 &= 0
 \end{aligned}
 \tag{11}$$

where: m_1, m_2, m_3 – the masses of the hammer, steel frame and foundation trough, respectively, c_1, c_2, c_3 – the damping constants of the viscous-elastic pad, viscous-spring isolation system and soil, respectively, k_1, k_2, k_3 – the stiffness of the viscous-elastic pad, viscous-spring isolation system and soil, respectively, $P(t)$ – the time history of the pulse, $\ddot{y}_i, \dot{y}_i, y_i$ – the acceleration, velocity and displacement of the i -th mass ($i = 1, 2, 3$), respectively.

The differential equations of motion (11) with initial conditions (12) were solved numerically in the Matlab program.

$$t = 0; \quad y_1 = y_2 = y_3 = 0; \quad \dot{y}_1 = \dot{y}_2 = \dot{y}_3 = 0 \tag{12}$$

The subsequent time histories of the pulses $P(t)$ described by equations (2-9) as the load were assumed. The integration of the equations was performed using the fourth order Runge-Kutta technique and own calculation scripts.

As the solution of the differential equations the time histories of the displacements, velocities and accelerations of individual elements of the forging system were obtained.

The force transmitted to the soil can be evaluated from equation (13) (Chehab and El Naggar, 2003; Chehab and El Naggar, 2004; Zheng et al., 2014).

$$P_S = c_3 \cdot \dot{y}_3 + k_3 \cdot y_3 \tag{13}$$

where: P_S – the force transmitted to the soil, c_3 – the damping constant of the soil, k_3 – the stiffness of the soil, \dot{y}_3 – the velocity of the foundation trough, y_3 – the displacement of the foundation trough.

The parameters of the numerical model were adopted on the basis of the data characterizing the real foundation of the die forging hammer MPM 16000 B - type, as shown in Fig. 6a. The parameters of the model are summarized in Table 1.

Tab. 1. Parameters of the computational model

Parameter	Value [kg]	Parameter	Value [N/m]	Parameter	Value [N·s/m]
m_1	168000	k_1	$950 \cdot 10^6$	c_1	$1.84 \cdot 10^6$
m_2	18500	k_2	$183 \cdot 10^6$	c_2	$3.6 \cdot 10^6$
m_3	248200	k_3	$8329 \cdot 10^6$	c_3	$12.26 \cdot 10^6$

5. ANALYSIS PARAMETERS, RESULTS AND DISCUSSION

To investigate the effect of the shape and duration of the pulse load on the dynamic response of the hammer-foundation forging system and the forces transmitted to the surroundings, comprehensive analyses were performed.

A single hit of the ram was analysed. The analyses involved eight forms of the pulse loads (Fig. 5) with the same pulse sizes $S = 79793 \text{ N} \cdot \text{s}$ but different durations.

The pulse size was determined on the basis of equation (10) (Lipiński, 1985) assuming that the impact of the ram and the upper die block with the total mass $m_B = 8085 \text{ kg}$ occurs with the maximum kinetic energy, which for the considered die hammer is $E_p = 175000 \text{ J}$, and the coefficient of restitution R has the value, which according to Dresig and Holzweißig (2010), Lipiński (1985) and Major (1980), corresponds to performing heavy works on the die hammers, that is, cold forging of steel ($R = 0.5$).

The pulse durations τ were changed from 0.001 s to 0.2 s every 0.001 s. The lower limit value was adopted based on the literature data (Altan et al., 1969; Leopa, 2011), while the upper limit was calculated based on the condition of occurrence of the short-term pulses (see chapter 2). For the triangular pulse, it was adopted that $\tau_1 = \tau_2$, while for the pulses: trapezoidal, triangular-trapezoidal, versed sine-rectangular as well as exponential-rectangular, it was assumed that $\tau_1 = \tau_3 = 0.2 \cdot \tau$. For the triangular-trapezoidal pulse, it was assumed, furthermore, that $u_{Pm} = 0.7$.

On the basis of the results, the pulse amplitudes, the maximum displacements, velocities and accelerations of the individual elements of the computational model as well as the maximum forces transmitted to the soil were determined.

The pulse amplitudes are shown in Fig. 7 as a function of the shape and duration of the pulses.

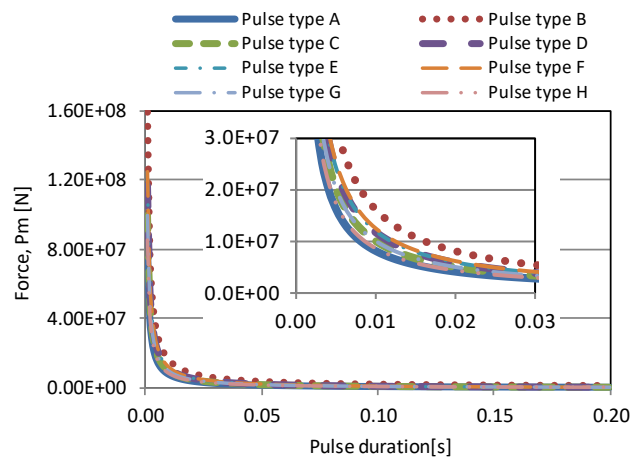


Fig. 7. The pulse amplitudes as function of shape and duration of pulses

Fig. 7 shows that for the same pulse sizes, regardless of their duration, the force reaches the highest value for the triangular pulse, while the maximum forces corresponding to the remaining pulses are lower by 21% for the semi-sinusoidal pulse, by 26% for the triangular-trapezoidal and parabolic pulse, by 37% for the versed sine-rectangular and trapezoidal pulse, by 50% for rectangular and exponential-rectangular pulse, respectively.

The maximum displacements, velocities and accelerations of the hammer and foundation trough in dependence of the shape and duration of the pulses are shown in Figs. 8–10.

The displacements, velocities and accelerations of the hammer and foundation trough reach the highest values for pulses with the shortest duration (Figs. 8–10). When the duration of the pulses increases, these values decrease. At the same time, depending on the pulse shape, the differences between the maximum displacements of the individual elements increase.

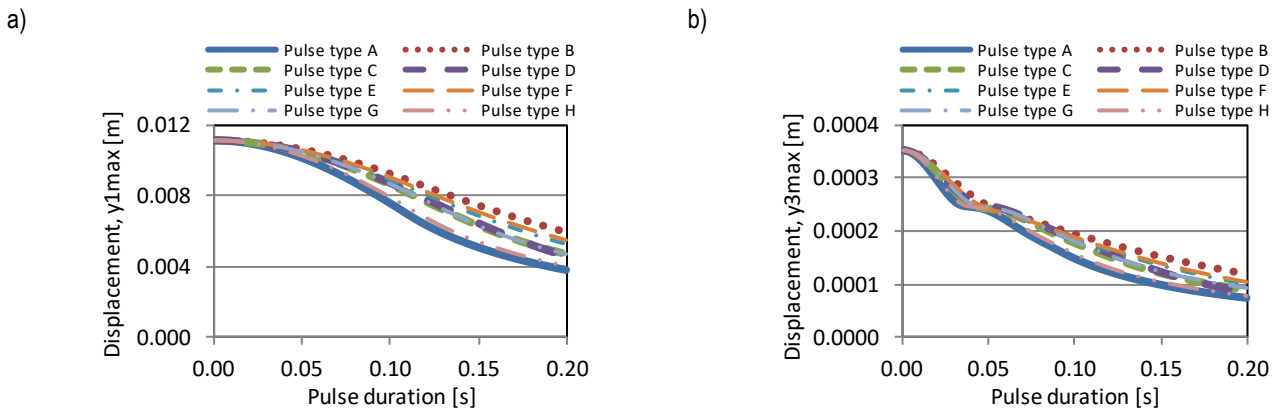


Fig. 8. Effect of shape and duration of pulses on the maximum displacement: a) of the hammer, b) of the foundation trough

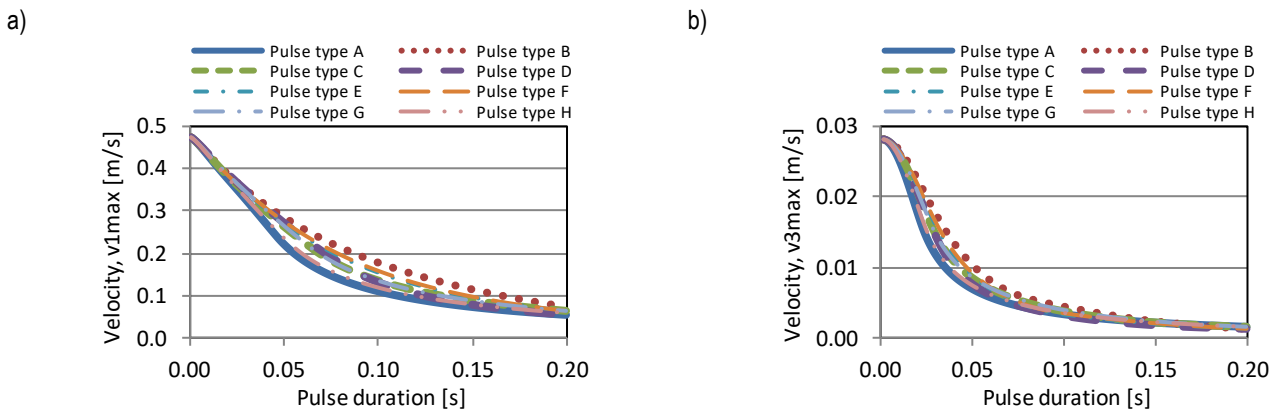


Fig. 9. Effect of shape and duration of pulses on the maximum velocity: a) of the hammer, b) of the foundation trough

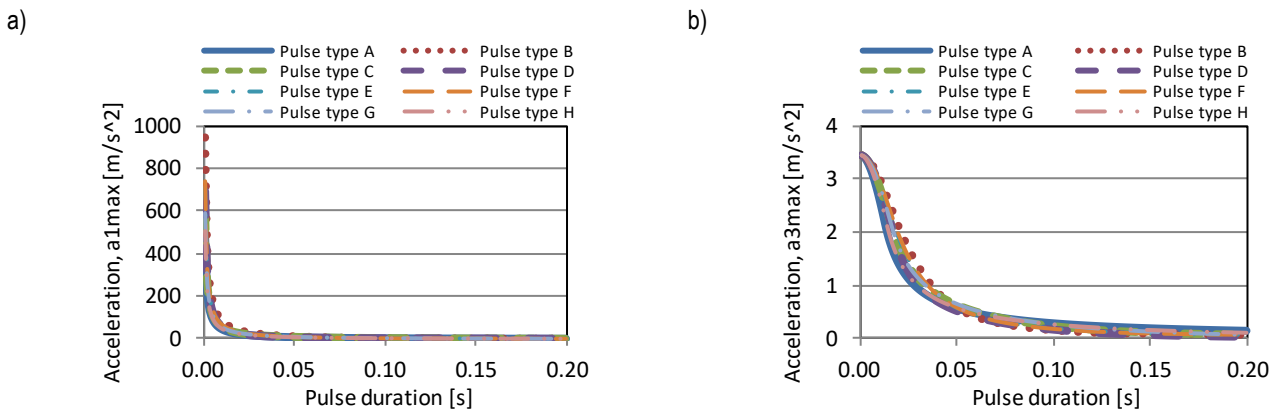


Fig. 10. Effect of shape and duration of pulses on the maximum acceleration: a) of the hammer, b) of the foundation trough

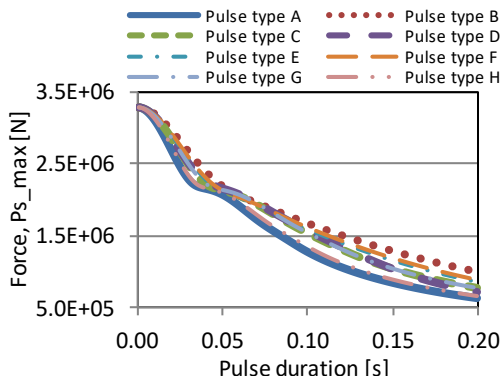


Fig. 11. The maximum forces transmitted to the soil as a function of shape and duration of pulses

Similar observations can be made regarding the maximum forces transmitted to the soil from Fig. 11.

6. SUMMARY AND CONCLUSIONS

In the paper, the effect of the duration and shape of a pulse load on the dynamic response of a hammer-foundation forging system was assessed. The forging system with three degrees of freedom was analysed. The analyses for eight forms of the pulse loads with the same pulse sizes but different durations were performed. The parameters of the analysis for unfavourable forging conditions, that is, cold forging of steel at maximum velocity were determined.

To investigate the effect of the pulse shape and duration on the dynamic response of the hammer-foundation forging system, the maximum displacements, velocities and accelerations of the hammer and foundation as well as the maximum forces transmitted to the soil were determined.

The results of the numerical analyses as a set of graphs were presented. Based on the results of the analyses, it was found that:

- A greater impact on the dynamic response of a forging system has the duration of a pulse than its shape;
- The displacements, velocities and accelerations of the forging system components as well as the forces transmitted to the soil reach the highest values for the pulses with the shortest duration;
- If the pulse duration is less than 0.01 s, the system response is insensitive to the shape of the pulse;
- As the pulse duration increases, the response of the forging system decreases.

Since, as the results of the analyses show, the shape of a pulse has a little effect on the dynamic response of the forging system, during the design work or checking the influence of the structure with known parameters on the soil and surroundings, theoretically, pulse loads of any shape can be used in calculation models. However, since with prolonging the pulse duration, the dynamic responses reach the highest values for the triangular pulse, it seems expedient to use this shape in the calculations.

Due to the large impact of the pulse duration on the maximum displacements and velocities of the forging system components as well as the forces transmitted to the soil, it is important that the pulse duration corresponds to the real forging conditions. Therefore, the analyses should be performed for the experimentally confirmed durations of the contact between the interacting materials.

If the results of the analyses show that for the adopted model parameters of the forging system, the permissible values of the foundation displacements (according to Lipiński (1985) and Major (1980)) or the permissible soil stress (according to Lipiński (1985)) have been exceeded and it is not possible to change these parameters, the only way to limit the negative impact of the forging hammer on the soil and surroundings will be such a modification of the parameters of the forming process, that will prolong the duration of contact between the interacting materials. The same actions should be taken to ensure the proper working conditions

for hammerman when the permissible levels of the hammer vibration amplitudes are exceeded (according to Lipiński (1985) and Major (1980)).

REFERENCES

1. **Altan T., Henning H.J., Sabroff A.M.** (1969), *Sixth interim topical report on a study of the mechanics of closed-die forging*, Battelle Memorial Institute, Columbus Laboratories, Ohio.
2. **Bieliajew J., Popow A.** (1967), Experimental study of the loads of colliding parts of hammers during impact, *Forging and Stamping Production* (in Russian), 2, 26-30.
3. **Chehab A.G., El Naggar M.H.** (2003), Design of efficient base isolation for hammers and presses, *Soil Dynamics and Earthquake Engineering*, 23 (2), 127-141.
4. **Chehab A.G., El Naggar M.H.** (2004), Response of block foundations to impact loads, *Journal of Sound and Vibration*, 276(1-2), 293-310.
5. **Dresig H., Holzweißig F.** (2010), *Dynamics of machinery*, Springer-Verlag, Berlin.
6. **Gryboś R.** (1969), *Theory of impact in discrete mechanical systems* (in Polish), PWN.
7. **Harris C.M. ed., Piersol A.G. ed.** (2002), *Harris' Shock and Vibration Handbook*, McGraw-Hill, New York.
8. **Leopa A.** (2011), Parametric method for dynamic analysis of mechanical impulsive systems actions, *Proc. of The Romanian Academy, Series A*, 12 (1), 63-70.
9. **Lipiński J.** (1985), *Machine foundations* (in Polish). Wyd. Arkady, Warszawa.
10. **Majewski L., Trąbka A.** (2006), Assessment of dynamical properties of steam-air die hammer MPM 10000 B, *TRANSFER 2006: The utilization of the new knowledge in the engineering practice, VIII International Scientific Conference*, Trencin, 28-29 september, 2 dil.
11. **Major A.** (1980), *Dynamics in civil engineering – analysis and design – volume II*, Budapest, Akademiai Kiado.
12. **Prolović V., Bonić Z., Živković S.** (2004), Dependence of the basic dynamic parameters on the disturbing force of the impact impulse type with different forms, *Facta Universitatis, Series: Architecture and Civil Engineering*, 3 (1), 23-31.
13. **Zheng E., Zhou X., Zhu S.** (2014), Dynamic response analysis of block foundations with nonlinear dry friction mounting system to impact loads, *Journal of Mechanical Science and Technology*, 28 (7), 2535-2548.

THE IMPACT OF TROPOSPHERE CORRECTION FOR DESIGNATION OF THE ELLIPSOIDAL HEIGHT OF AIRCRAFT AT APPROACH TO LANDING PROCEDURE

Kamil KRASUSKI,* Stepan SAVCHUK*

*Institute of Navigation, Military University of Aviation, ul. Dywizjonu 303 nr 35, 08-521 Dęblin, Poland

k.krasuski@law.mil.pl, s.savchuk@law.mil.pl

received 3 October 2019, revised 11 December 2019, accepted 12 December 2019

Abstract: The paper reports on research into the effect of the troposphere correction on the accuracy of the vertical component determination of an aircraft's flight as it approaches landing at Deblin Airport. The article presents ellipsoidal height value of the aircraft when the troposphere correction is considered in navigational calculations and when it is not taken into account. Accuracy of the aircraft positioning in the vertical plane using the SPP method is determined. The study shows that application of the troposphere correction in navigational calculations increases the accuracy of the vertical component determination by 25%–32%. The article and the study may serve as a valuable source of information for pilots, flight instructors and aircraft crews during training in operation and implementation of GNSS in aviation.

Key words: GPS, Aircraft, Ellipsoidal Height, Troposphere Correction

1. INTRODUCTION

Studies of the tropospheric state are increasingly used in aviation. Atmospheric weather effect is a dangerous condition during air operations, especially whilst landing. Atmospheric hazards are an unfavourable process during aircraft operation. Study and monitoring of the troposphere seems to be a key technical parameter in modern aviation. Use of GNSS satellite equipment is one of the ways to determine the state of the troposphere during air operations (Krasuski et al., 2017). The parameter of the tropospheric effect is included in the observation equations using both code and carrier phase GNSS measurements (Schaer, 1999). Code measurements on L1 frequency are generally used to determine the position of the aircraft via satellite navigation technology (ICAO, 2006). In this case, the tropospheric effect parameter (troposphere correction) is estimated using deterministic tropospheric models. The Hopfield model, the Saastamoinen model and the Simple model are the most common deterministic tropospheric models.

There is a vast amount of research worldwide aimed to determine the status of the troposphere and how it is applied in aviation, for example:

- determination of the tropospheric status in GBAS aircraft support system (Parameswaran et al., 2008);
- error determination for the troposphere correction in the height function of the aircraft's flight (Kutsenko et al., 2018);
- determination of the tropospheric state using Hopfield and RTCA MOPS models for GPS system (Sultana et al., 2013);
- determination of the tropospheric state using GPS and Galileo satellite navigation systems for air transport (Guilbert, 2016);
- evaluation of the tropospheric effect on the determination of the aircraft's geocentric coordinates (Krasuski et al., 2016);

- evaluation of the tropospheric effect using the MOPS RTCA model within the APV approach procedure in transport aviation (Neri, 2011);
- evaluation of the tropospheric effect on the determination of the aircraft's location (Boon et al., 1997);
- determination of the troposphere correction while in flight (Vyas et al., 2011);
- effect of the troposphere on the determination of the VPL reliability parameter in air transportation (Wang et al., 2017);
- testing of the tropospheric model developed by UNB researchers to determine airplane positioning in air navigation (Collins, 1999).

The paper aims to evaluate the effect of the troposphere on the ellipsoidal height determination of the aircraft's flight. Real navigation data and observations from the onboard GNSS receiver installed on a Cessna 172 aircraft were used in the study. Results of the study directly affect flight safety in the vertical plane VNAV. The developed technique, which studies the effect of the troposphere on the determination of the aircraft's positioning, can be used practically to improve flight safety.

2. THE RESEARCH METHOD

The tropospheric effect on the determination of the aircraft's ellipsoidal height was investigated using the code-based method (SPP) in the GPS navigation system. The basic observation equation using the SPP code positioning method in the GPS system is (Hofmann-Wellenhof et al., 2008):

$$C1 = d + c \cdot (dtr - dts) + Ion + Trop + TGD + Rel + Mp \quad (1)$$

where: C1 – the code observations at L1 frequency in GPS sys-

tem (expressed in meters), c – light speed (expressed in m/s), d – geometric distance between satellite and receiver on L1 frequency in GPS system (expressed in meters), $d = \sqrt{(X - X_{sat})^2 + (Y - Y_{sat})^2 + (Z - Z_{sat})^2}$, (X, Y, Z) – XYZ geocentric coordinates of the aircraft, $(X_{sat}, Y_{sat}, Z_{sat})$ – satellite coordinates in GPS system, dtr – receiver clock bias in GPS system (expressed in seconds), dts – satellite clock bias in GPS system (expressed in seconds), Ion – ionosphere delay in GPS system (expressed in meters), $Trop$ – troposphere correction in GPS system (expressed in meters), TGD – Time Group Delay in GPS system (expressed in meters), Rel – relativistic effect in GPS system (expressed in meters), Mp – multipath effect and measurement noise in GPS system (expressed in meters).

In equation (1), the parameter $Trop$ denotes an oblique troposphere correction expressed as dependence (Savchuk et al., 2018):

$$Trop = SHD + SWD = m_H \cdot ZHD + m_W \cdot ZWD \quad (2)$$

where: SHD – slant hydrostatic delay (expressed in meters), SWD – slant wet delay (expressed in meters), ZHD – zenith hydrostatic delay (expressed in meters), ZWD – zenith wet delay (expressed in meters), m_H – mapping function for zenith hydrostatic delay (without a unit), m_W – mapping function for zenith wet delay (without a unit).

Whereas, the ellipsoidal height value is calculated using the recursive process based on the previously determined plane coordinates in the XYZ geocentric system, as shown below (Sanz Subirana et al., 2013):

$$h = \frac{\rho}{\cos B_i} - R \quad (3)$$

where: $\rho = \sqrt{X^2 + Y^2}$ – geocentric distance on the ellipsoid (expressed in meters), R – radius of curvature of the first ellipsoid vertical, $R = \frac{a}{\sqrt{1 - e^2 \cdot \sin^2 B_i}}$ (expressed in meters), a – semi-major axes (expressed in meters), e – eccentricity (without a unit), B – Latitude (expressed in degrees), i – iteration step (without a unit).

3. THE RESEARCH TEST

The effect of the troposphere on the determination of the ellipsoidal height during aircraft's approach to landing was estimated during the research test. The Cessna 172 aircraft made a test flight around the EPDE military airport in Deblin (Ćwiklak et al., 2010). The study focused strictly on the final stage of the flight, namely on the approach to landing and landing itself. Figure 1 shows vertical flight trajectory using the ellipsoidal height values during the approach to landing.

Analysis of the tropospheric effect on the determination of the aircraft's ellipsoidal height was conducted. The analysis intended to detect a change in the ellipsoidal height of the aircraft's flight with troposphere correction and without it. The effect of the troposphere was considered in two deterministic models: the Saastamoinen model and the SBAS model. Consequently, three results were obtained: in the first two results models that took into account tropospheric effect were used, whereas in the third troposphere correction was eliminated and omitted.

The $Trop$ parameter was estimated in Saastamoinen model

as below (Abdefatah et al., 2018):

$$Trop = \frac{1}{\cos z} \cdot (ZHD_{Saas} + ZWD_{Saas}) \quad (4)$$

where:

$$ZHD_{Saas} = 0.002277 \cdot \frac{P}{1 - 0.00266 \cdot \cos(2\phi) - 0.0000028 \cdot h'}$$

$$ZWD_{Saas} = 0.002277 \cdot \left(\frac{1255}{T} + 0.05 \right) \cdot e, \quad (P, T, e) - \text{pressure, temperature and water vapor pressure, } (\phi, h) - \text{Latitude and ellipsoidal height paramaters, } z - \text{zenith angle.}$$

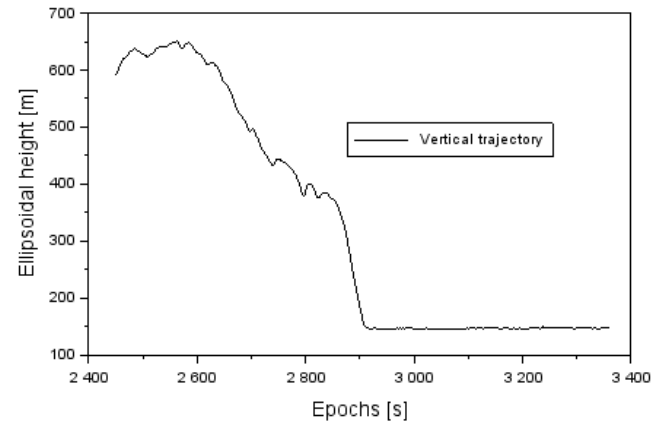


Fig. 1. The vertical trajectory at approach to landing procedure

The $Trop$ parameter was estimated in SBAS model as below (Uemo et al., 2001):

$$Trop = \frac{1.001}{\sqrt{0.002001 + \sin^2 El}} \cdot (ZHD_{SBAS} + ZWD_{SBAS}) \quad (5)$$

where: $ZHD_{SBAS} = ZHD_0 \cdot \left(1 - \frac{\beta \cdot h}{T_K} \right)^{\frac{g}{R_d \beta}}$, $ZWD_{SBAS} = ZWD_0 \cdot \left(1 - \frac{\beta \cdot h}{T_K} \right)^{\frac{(\lambda+1) \cdot g}{R_d \beta} - 1}$, (ZHD_0, ZWD_0) – ZHD and ZWD term at sea level, (λ, β) – water vapor lapse rate and temperature lapse rate, (g, R_d) – constant coefficients, h – ellipsoidal height paramaters, T_K – temperature, El – elevation angle.

Calculations of the aircraft's positioning were made in RTKLIB v.2.4.3 software using RTKPOST module. Calculation strategy using the RTKPOST library involved (Takasu, 2013):

- positioning method: SPP;
- elevation angle: 5o, based on ICAO recommendation (ICAO, 2006);
- source of the ionospheric correction: message in the navigation file;
- source of the tropospheric correction: Saastamoinen model for the first result, SBAS for the second result, OFF for the third case;
- source of the ephemeris data and satellite clock corrections: navigation file;
- coordinate system: ellipsoidal BLh;
- a priori average deviation of the pseudorange: $mI = 1m$;
- type of observation: code at L1 frequency;
- weight: in the elevation angle function, $p = \left(\frac{mI}{\sin El} \right)^2$;
- maximum DOP value: 30;

- observation interval: 1 s,
- multipath and measurement noise: applied.

4. THE RESULTS

Ellipsoidal height value with and without troposphere correction was determined during the first stage of the study. Figure 2 shows changes in ellipsoidal height calculated using the SPP code method. Results, where troposphere correction obtained from the Saastamoinen model was used, varied from 143.5 m to 650.6 m. Whereas, ellipsoidal height in the SBAS troposphere model varied from 143.6 m to 651.6 m. Ellipsoidal height value in the third result, where troposphere correction was not considered (OFF), ranged between 152.9 m and 666.6 m.

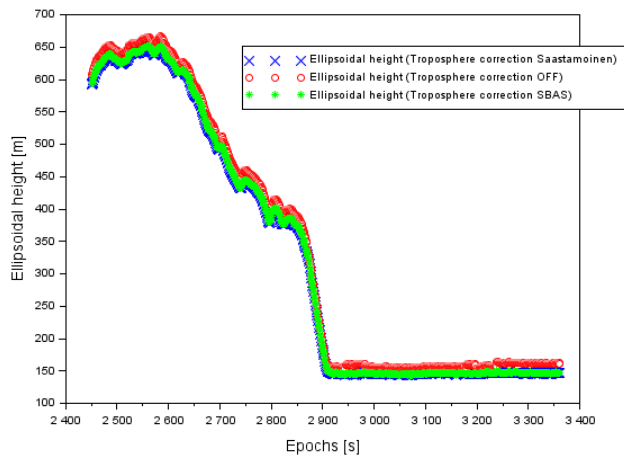


Fig. 2. The results of ellipsoidal height at approach to landing procedure

Values h shown in Figure 2 were compared to analyze the results of the aircraft's ellipsoidal height (h). For this purpose, differences in the aircraft's ellipsoidal height h were determined (Auh et al., 2018):

$$\begin{cases} dh1 = h_{OFF}^{SPP} - h_{Saastamoinen}^{SPP} \\ dh2 = h_{OFF}^{SPP} - h_{SBAS}^{SPP} \\ dh3 = h_{SBAS}^{SPP} - h_{Saastamoinen}^{SPP} \end{cases} \quad (6)$$

where: h_{OFF}^{SPP} – ellipsoidal height of aircraft without troposphere correction, see equation (3) (expressed in meters), $h_{Saastamoinen}^{SPP}$ – ellipsoidal height of aircraft with troposphere correction of Saastamoinen model, see equation (3) (expressed in meters), h_{SBAS}^{SPP} – ellipsoidal height of aircraft with troposphere correction of SBAS model, see equation (3) (expressed in meters).

Value of the aircraft's ellipsoidal height difference is defined as a function of time (Figure 3). The corresponding differences of the ellipsoidal height $dh1$ are in the range of 6.7 m and 17.3 m, the average ellipsoidal height difference is 13.1 m and its RMS error equals 13.4 m. Meanwhile, aircraft's ellipsoidal height difference $dh2$ ranges from 6.8 m to 16.0 m, the average height difference equals 12.6 m, and the RMS error is 12.7 m. Whereas, aircraft's ellipsoidal height difference $dh3$ varies from -0.1 m to 1.3 m, the average ellipsoidal height difference equals 0.5 m, and the RMS error is 0.7 m. This, therefore, shows that troposphere correction effect is essential to determining the ellipsoidal height of the air-

craft during landing approach. Ignoring the tropospheric effect on the positioning of the aircraft causes significant errors in determination of its height.

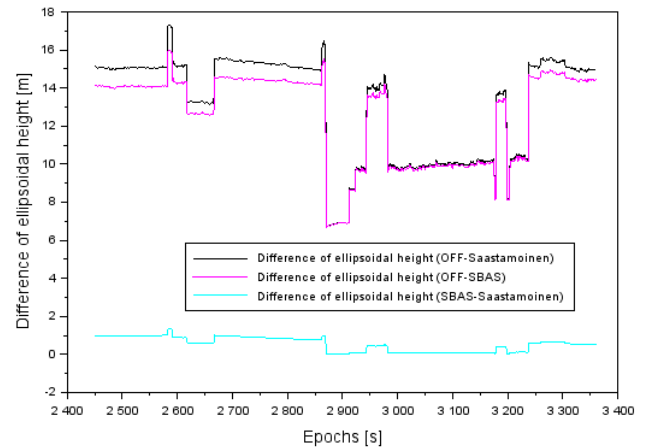


Fig. 3. The difference of ellipsoidal height at approach to landing procedure

The obtained results of the height differences ($dh1$, $dh2$, $dh3$) were also presented in a function of the ellipsoidal height change during the Cessna 172 aircraft's flight (see Fig. 4). Figure 4 shows that ($dh1$, $dh2$) parameters have the highest value in the range of 350 and 700 m. Moreover, significant differences in the ($dh1$, $dh2$) parameters occur directly during landing at Deblin Airport. In air navigation, information about the significant tropospheric effect on the determination of the aircraft's ellipsoidal height during its approach to landing is negative for the safety of the flight. Thus, studying the tropospheric effect on the determination of the aircraft's ellipsoidal height in this flight stage is of a grave importance in aviation. The change in the ellipsoidal height of the aircraft is not that significant for $dh3$ parameter – the difference of ellipsoidal height is relatively small, less than 1.3 m. Therefore, the use of the troposphere model in equation (1) is important for the SPP code method in air navigation.

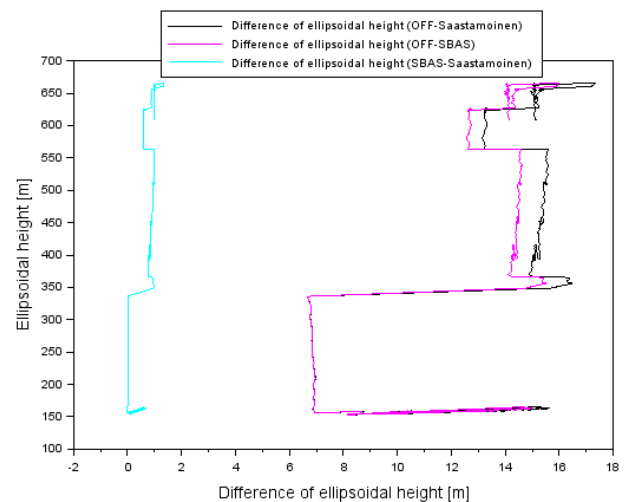


Fig. 4. The difference of ellipsoidal height at approach to landing procedure

The next stage of the study focused on determining the accuracy of the vertical component h in aircraft positioning using the

SPP code method. Therefore, ellipsoidal height determined using the SPP method was compared with its more accurate value obtained using the dual-frequency L1/L2 PPP method. Using this method, the h-component of an aircraft can be determined with an average error of about 0.1 m. Thus, PPP technology is also used in air navigation to recreate the exact flight trajectory of an aircraft. Accuracy of the vertical component h in aircraft positioning is determined below using the SPP code method (Uemo et al., 2001):

$$\begin{cases} rh1 = h_{OFF}^{SPP} - h_{PPP} \\ rh2 = h_{Saastamoinen}^{SPP} - h_{PPP} \\ rh3 = h_{SBAS}^{SPP} - h_{PPP} \end{cases} \quad (7)$$

where: h_{PPP} – ellipsoidal height of aircraft based on PPP solution (expressed in meters).

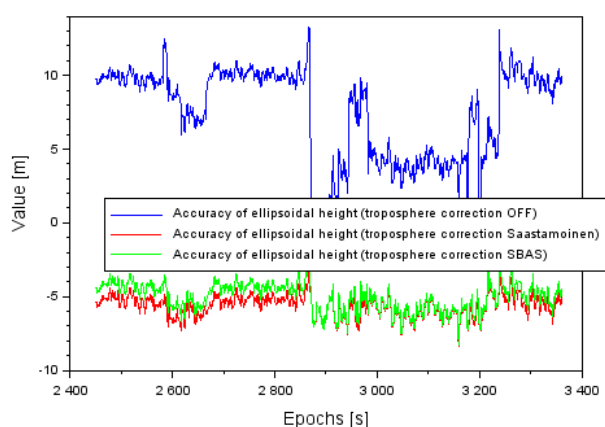


Fig. 5. The accuracy of ellipsoidal height at approach to landing procedure

Figure 5 shows the accuracy of the aircraft's h component obtained after using the SPP code method. When the troposphere correction is not applied (OFF), the accuracy of the h component varies from -0.3 m to +13.4 m with an average accuracy value of 7.5 m and RMS error being 8.1 m. When troposphere correction is determined using the Saastamoinen model with SPP method, the accuracy of the ellipsoidal height of the aircraft ranges from -8.4 m to -2.9 m, while an average accuracy equals 5.6 m and RMS error is 5.6 m. When the SBAS model is used, the accuracy of the aircraft's ellipsoidal height varies from -8.3 m to -1.6 m, the average accuracy is -5.1 m and the RMS error is 5.2 m.

The results of the study show that the use of the SBAS model increases the accuracy of the h-component positioning by 32% compared to when troposphere correction is not taken into account (OFF) in the positioning of the aircraft. Furthermore, the use of the tropospheric SBAS model increases the accuracy of the h positioning component by approximately 10% in comparison to Saastamoinen model. However, the use of the Saastamoinen model increases the accuracy of the h positioning component by approximately 25% when troposphere correction is not considered in the navigational calculations (OFF).

5. CONCLUSIONS

The paper presents the results of the navigational calculations measuring the tropospheric effect on the determination of the

ellipsoidal height of an aircraft as it approaches landing. The accuracy of the aircraft's navigational positioning with and without troposphere correction was analysed. Navigational calculations for the SPP code method were done in RTKLIB v.2.4.3 software. Calculations were based on real GPS navigation data and observations from an onboard GNSS receiver installed on a Cessna 172 aircraft. As part of the study, the position of the aircraft was determined using three methods: 1) the Saastamoinen troposphere model, 2) the SBAS troposphere model, 3) without troposphere correction (OFF). Values of the aircraft's ellipsoidal height obtained using the SPP code method were compared with more accurate data obtained using the PPP measurement technique. The study shows that:

- Omission of the troposphere correction in the navigational calculations causes low accuracy (over 13 m) in determination of the vertical component h.
- Consideration of the troposphere correction in navigational calculations increases the accuracy of the vertical component h determination by 25%–32%.
- Troposphere correction effect plays a crucial role in determining the ellipsoidal height accuracy of the aircraft's flight in navigation calculations.

In the future, the authors will estimate the troposphere delay, especially Zenith Troposphere Delay (ZTD) in kinematic test in aviation. In addition, the ZTD will be calculated using the PPP method for dual-frequency onboard GNSS receiver. This solution will be tested in absolute and differential GNSS positioning in aviation.

REFERENCES

1. **Abdelfatah M. A., Mousa A.E., El-Fiky G. S.** (2018), Assessment of tropospheric delay mapping function models in Egypt: Using PTD database model, *NRIAG Journal of Astronomy and Geophysics*, 7(1), 47–51.
2. **Auh S.-C., Lee S.-B.** (2018), Analysis of the Effect of Tropospheric Delay on Orthometric Height Determination at High Mountain, *KSCE Journal of Civil Engineering*, 22, 4573.
3. **Boon F.J.G., de Jonge P.J., Tiberius C.C.J.M.** (1997), Precise aircraft positioning by fast ambiguity resolution using improved troposphere modeling, *Proceedings of the 10th International Technical Meeting of the Satellite Division of The Institute of Navigation (ION GPS 1997)*, Kansas City, MO, 1877–1884.
4. **Collins J.P.** (1999), *Assessment and Development of a Tropospheric Delay Model for Aircraft Users of the Global Positioning System*, University of New Brunswick, Department of Geodesy and Geomatics Engineering, Technical Report no. 203.
5. **Ćwiklak J., Jafarnik H.** (2010), The monitoring system for aircraft and vehicles of public order services based on GNSS, *Annual of Navigation*, 16, 15–24.
6. **Guilbert A.** (2016), *Optimal GPS/GALILEO GBAS methodologies with an application to troposphere*, PhD thesis, Institut National Polytechnique de Toulouse (INP Toulouse).
7. **Hofmann-Wellenhof B., Lichtenegger H., Wasle E.** (2008), *GNSS – Global Navigation Satellite Systems: GPS, GLONASS, Galileo and more*, SpringerWienNewYork, Wien, Austria.
8. **International Civil Aviation Organization** (2006), *ICAO Standards and Recommended Practices (SARPS). Annex 10, Volume 1 (Radionavigation aids)*, Polish version available at website: <http://www.ulc.gov.pl/prawo/prawomi%20C4%99dzynarodowe/206-konwencje>, current on: 15.10.2018.

9. **Krasuski K., Jafernik H.** (2017), Determination troposphere delay using GPS sensor in air transport, *Autobusy: technika, eksploatacja, systemy transportowe*, 18(6), 826–829 (in Polish).
10. **Krasuski K., Wierzbicki D.** (2016), The impact of atmosphere delays in processing of aircraft's coordinates determination, *Journal of KONES*, 23(2), 209–214.
Kutsenko O., Ilnytska S., Konin V. (2018), Investigation of the the residual tropospheric error influence on the coordinate determination accuracy in a satellite landing system, *Aviation*, 22(4), 156–165.
12. **Lkan R. M., Ozulu İ. M., Ilci V.** (2016), Precise Point Positioning (PPP) Technique versus Network-RTK GNSS, *FIG Working Week 2016*, Christchurch, New Zealand, 1–10.
13. **Neri P.** (2011), *Use of GNSS signals and their augmentations for Civil Aviation navigation during Approaches with Vertical Guidance and Precision Approaches*, PhD thesis, Institut National Polytechnique de Toulouse (INP Toulouse).
14. **Parameswaran K., Saha K., Raju C.S.** (2008), Development of a regional tropospheric delay model for GPS-based navigation with emphasis to the Indian Region, *Radio Science*, 43, RS4007
15. **Sanz Subirana J., Juan Zornoza J. M., Hernandez-Pajares M.** (2013), *GNSS Data Processing, Volume I: Fundamentals and Algorithms*, Publisher: ESA Communications, ESTEC, Noordwijk, Netherlands.
16. **Savchuk S., Khoptar A.** (2018), Estimation of Slant Tropospheric Delays from GNSS Observations with Using Precise Point Positioning Method, *Annual of Navigation*, 25, 253–266.
17. **Schaer S.** (1999), *Mapping and predicting the Earth's ionosphere using Global Positioning System*, PhD thesis, Neunundfunzigster Band volume 59, Zurich.
18. **Sultana Q., Sarma A.D., Javeed M.Q.** (2013), Estimation of tropospheric time delay for Indian LAAS, *2013 International Conference on Emerging Trends in VLSI, Embedded System, Nano Electronics and Telecommunication System (ICEVENT)*, Tiruvannamalai, 1–5.
19. **Takasu T.** (2013), *RTKLIB ver. 2.4.3 Manual, RTKLIB: An Open Source Program Package for GNSS Positioning*, Paper available at website: http://www.rtklib.com/prog/manual_2.4.2.pdf, current on 2019.
20. **Uemo M., Hoshinoo K., Matsunaga K., Kawai M., Nakao H., Langley R., Bisnath S.** (2001), Assessment of atmospheric delay correction models for the Japanese MSAS; *Proceedings of the ION GPS 2001*; Salt Lake, UT, USA.
21. **Vyas M. R., Lim S., Rizos C.** (2011), Analysis of Zenith Path Delay in dynamically changing environment, *International Global Navigation Satellite Systems Society IGNSS Symposium 2011*, University of New South Wales, Sydney, NSW, Australia, 1–8.
22. **Wang Z., Xin P., Li R., Wang S.** (2017), A Method to Reduce Non-Nominal Troposphere Error, *Sensors*, 17, 1751.

Acknowledgements : This paper was supported by Military University of Aviation for 2019 year.

MIXED BOUNDARY VALUE PROBLEM FOR AN ANISOTROPIC THERMOELASTIC HALF-SPACE CONTAINING THIN INHOMOGENEITIES

Heorhiy SULYM^{*}, Iaroslav PASTERNAK^{}, Mariia SMAL^{**}, Andrii VASYLYSHYN^{***}**

^{*}Bialystok University of Technology, ul. Wiejska 45C, 15-351 Bialystok, Poland

^{**}Lutsk National Technical University, Lvivska Str. 75, 43018 Lutsk, Ukraine

^{***}Ivan Franko National University of Lviv, Universytetska Str. 1, 79000 Lviv, Ukraine

h.sulym@pb.edu.pl, yaroslav.pasternak@gmail.com, m.smal@lntu.edu.ua, vasylyshyn.c.h@gmail.com

received 16 May 2019, revised 6 December 2019, accepted 13 December 2019

Abstract: The paper presents a rigorous and straightforward approach for obtaining the 2D boundary integral equations for a thermoelastic half-space containing holes, cracks and thin foreign inclusions. It starts from the Cauchy integral formula and the extended Stroh formalism which allows writing the general solution of thermoelastic problems in terms of certain analytic functions. In addition, with the help of it, it is possible to convert the volume integrals included in the equation into contour integrals, which, in turn, will allow the use of the method of boundary elements. For modelling of solids with thin inhomogeneities, a coupling principle for continua of different dimensions is used. Applying the theory of complex variable functions, in particular, Cauchy integral formula and Sokhotski–Plemelj formula, the Somigliana type boundary integral equations are constructed for thermoelastic anisotropic half-space. The obtained integral equations are introduced into the modified boundary element method. A numerical analysis of the influence of boundary conditions on the half-space boundary and relative rigidity of the thin inhomogeneity on the intensity of stresses at the inclusions is carried out.

Keywords: thermoelasticity, anisotropic half-space, boundary element method, thin inclusion, crack, stress intensity factors, Stroh formalism

1. INTRODUCTION

Modern composite materials are widely used in engineering structures due to their useful properties (Woo, 2011). To a large extent, most of them are anisotropic. It is also clear that the internal structure of most of them is not perfect. Since material fracture generally initiates at various defects, there is a need for the development of analytical and numerical approaches for the analysis of internal physical and mechanical fields and the strength and reliability of the structural elements made of composite materials.

In most cases, modelling of bulky structural elements can be reduced to the analysis of semi-infinite solids, for example, half-space, since it is essential to estimate the influence of interaction of internal inhomogeneities with the boundary of a solid. A three-dimensional model for solving steady-state heat conduction in a semi-infinite domain containing an elementary cuboidal inhomogeneity was established by Yang et al. (2019). Three-dimensional exact fundamental solutions of the thermoelastic field in a transversely isotropic elastic medium weakened by a half infinite plane crack subjected to a pair of point thermal loadings symmetrically acting on the crack surface were presented by Li (2012). Sherief et al. (2014) applied the fractional order theory of thermoelasticity to a two-dimensional problem for a half-space. Şeremet (2011) derived the exact Green's function and a Poisson-type integral formula for a boundary-value problem (BVP) for a thermoelastic wedge, half-space and quarter-space. For solving two-dimensional thermoelastic crack problems, Chen et al. (2016) used singular edge-based smoothed finite element method (ES-FEM).

The jump function method is convenient and effective in simulation of thin inhomogeneities (Sulym, 2007). The idea of this

method is that the inclusion as a geometric object is excluded from consideration, and its effect is reduced to introduction of certain functions of the jump of physical and mechanical fields in the medium while passing the median surface of the thin-walled inhomogeneity.

The boundary element method (BEM) perfectly suits for solving the stress concentration and fracture mechanics problems due to its high precision and efficiency (Bozhydarnyk et al., 2011; Hou, 2011; Qin, 1999; Shiah, 2000). Tokovy and Ma (2009) obtained the Volterra integral equations of thermoelasticity for the orthotropic plane, half-plane and a strip. However, in the presence of thermal effects, there are additional volume integral terms in integral equations that fully reduce the advantages of BEM. In the case of isotropic solids, these volume integrals can be easily converted to boundary ones (Mukherjee, 1999). However, in the case of anisotropy, transformation of the volume integral into the contour one is a difficult task. For the first time, in the case of a plane thermoelasticity problem, the temperature volume integral was reduced to the contour one in the real domain in Pasternak (2012).

The abovementioned works consider mainly half-space with traction-free thermally insulated surface. However, in most of the engineering problems, especially those of contact mechanics, mixed thermomechanical boundary conditions should be considered, that is, at the half-space boundary given are some components of traction vector and some components of displacement vector. For example, if the half-space boundary $x_2 = 0$ rests on the smooth rigid basement, the component u_2 of displacement vector and the component t_1 of traction vector are zero. Such problems for thermoelastic anisotropic half-space are not found in scientific literature.

In this paper, the methods based on the complex variable calculus, the Stroh formalism, the jump function method and the BEM (Pasternak, 2012; Pasternak et al., 2013) are used to obtain new integral formulas and equations for anisotropic thermoelastic half-space with holes, cracks and thin deformable inclusions, taking into account all possible mixed mechanical and thermal boundary conditions on its boundary.

2. GOVERNING EQUATIONS OF THERMOELASTICITY

Consider a solid resting in a fixed rectangular coordinate system $Ox_1x_2x_3$. According to Hwu (2010), the equilibrium equation, the equation of thermal balance, as well as the constitutive equations of plain strain of a linearly thermoelastic body and of plane stationary heat conductivity are written as:

$$\sigma_{ij,j} = 0, h_{i,i} = 0, (i, j = 1, 2, 3); \quad (1)$$

$$\sigma_{ij} = C_{ijkl}\varepsilon_{kl} - \beta_{ij}\theta, h_i = -k_{ij}\theta_{,j}, \quad (2)$$

where $\varepsilon_{ij} = (u_{i,j} + u_{j,i})/2$ is a strain tensor, σ_{ij} is a stress tensor, h_i is a heat flux vector, u_i is a displacement vector, θ is the change in temperature compared with the reference one, C_{ijkl} are the elastic moduli, k_{ij} are the heat conduction coefficients, $\beta_{ij} = C_{ijkl}\alpha_{km}$ ($i, j, k, m = 1, \dots, 3$) are the thermal moduli and α_{ij} are the thermal expansion coefficients. The tensors C_{ijkl} , k_{ij} , α_{ij} and β_{ij} are fully symmetric. Here and further, the Einstein summation convention is used. Using the generalised Stroh formalism, it is possible to derive the following dependences:

$$\theta = 2\text{Re}\{g'(z_t)\}, \vartheta = 2k_t\text{Im}\{g'(z_t)\}, h_1 = -\vartheta_{,2}, h_2 = \vartheta_{,1}, k_t = \sqrt{k_{11}k_{22} - k_{12}^2}, \mathbf{u} = 2\text{Re}[\mathbf{A}\mathbf{f}(z_*) + \mathbf{c}g(z_t)], \boldsymbol{\varphi} = 2\text{Re}[\mathbf{B}\mathbf{f}(z_*) + \mathbf{d}g(z_t)], \sigma_{i1} = -\varphi_{i,2}, \sigma_{i2} = \varphi_{i,1}; z_t = x_1 + p_t x_2, z_\alpha = x_1 + p_\alpha x_2, \mathbf{f}(z_*) = [F_1(z_1), F_2(z_2), F_3(z_3)]^T, \quad (3)$$

where ϑ is a heat flux function, $F_\alpha(z_\alpha)$ and $g(z_t)$ are the complex analytic functions with respect to their arguments and the complex constant p_t is a root (with a positive imaginary part) of the characteristic equation for heat conduction

$$k_{22}p_t^2 + 2k_{12}p_t + k_{11} = 0.$$

Constant complex matrices \mathbf{A} , \mathbf{B} , vectors \mathbf{c} , \mathbf{d} and scalars p_α ($\alpha = 1, 2, 3$) are determined from the extended Stroh eigenvalue problem.

The relationship between the Stroh's complex potentials and vector functions of displacements and stresses is given by the following relations:

$$\mathbf{f}(z_*) = \mathbf{B}^T \mathbf{u} + \mathbf{A}^T \boldsymbol{\varphi} - \mathbf{B}^T \mathbf{u}^t - \mathbf{A}^T \boldsymbol{\varphi}^t, \quad \mathbf{u}^t = 2\text{Re}\{\mathbf{c}g(z_t)\}, \boldsymbol{\varphi}^t = 2\text{Re}\{\mathbf{d}g(z_t)\}. \quad (4)$$

Based on Eq. (3), one can derive the following relation between the function $g'(z_t)$, temperature and heat flux function

$$g'(z_t) = \frac{1}{2} \left(\theta + i \frac{\vartheta}{k_t} \right). \quad (5)$$

3. DERIVATION OF INTEGRAL FORMULAE FOR THE STROH COMPLEX FUNCTIONS

For thermoelastic half-space $x_2 > 0$ containing a system of holes bounded with smooth closed contours $\Gamma = \cup_i \Gamma_i$, the following dependencies are derived:

$$\mathbf{f}(z_*) = \frac{1}{2\pi i} \int_\Gamma \left\langle \frac{d\tau_*}{\tau_* - z_*} \right\rangle \mathbf{f}(\tau_*) + \frac{1}{2\pi i} \int_{-\infty}^{\infty} \left\langle \frac{dx_1}{x_1 - z_*} \right\rangle \mathbf{f}(x_1), (\text{Im } z_* > 0), \quad (6)$$

where $(F(z_*)) = \text{diag}[F_1(z_1), F_2(z_2), F_3(z_3)]$.

It is obvious that outside the half-space, Cauchy integrals (6) are equal to zero. Therefore, for external points z_* ($\text{Im } z_* > 0$), Eq. (6) is writes as:

$$\frac{1}{2\pi i} \int_\Gamma \left\langle \frac{d\tau_*}{\tau_* - z_*} \right\rangle \mathbf{f}(\tau_*) + \frac{1}{2\pi i} \int_{-\infty}^{\infty} \left\langle \frac{dx_1}{x_1 - z_*} \right\rangle \mathbf{f}(x_1) = 0, (\text{Im } z_* > 0). \quad (7)$$

Integral representations in Eqs (6) and (7) include linear integrals along the infinite half-space boundary that are inconvenient for further calculations. To exclude them from consideration, we will use four different types of boundary conditions on the half-space boundary:

$$\vartheta(x_1) = 0 \quad (x_2 = 0); \quad (8a)$$

$$\theta(x_1) = 0 \quad (x_2 = 0); \quad (8b)$$

$$u_1(x_1) = 0, \varphi_2(x_1) = 0 \quad (x_2 = 0); \quad (8c)$$

$$u_2(x_1) = 0, \varphi_1(x_1) = 0 \quad (x_2 = 0). \quad (8d)$$

3.1. Heat conduction

According to the boundary conditions in Eq. (8a) and Eq. (5), the integral formula for the function $g'(z_t)$ can be rewritten as follows:

$$g'(z_t) = \frac{1}{2\pi i} \int_\Gamma \frac{g'(\tau_t) d\tau_t}{\tau_t - z_t} + \frac{1}{4\pi k_t} \int_{-\infty}^{\infty} \frac{\vartheta(x_1) dx_1}{x_1 - z_t}. \quad (9)$$

Having calculated the complex conjugate expression for the Cauchy integral and using Eqs (6) and (5), we obtain the integral value along the half-space boundary:

$$\frac{1}{4\pi i} \int_{-\infty}^{\infty} \frac{\theta(x_1) dx_1}{x_1 - z_t} = -\frac{1}{2\pi i} \int_\Gamma \frac{g'(\bar{\tau}_t) d\bar{\tau}_t}{\bar{\tau}_t - z_t}. \quad (10)$$

Substituting Eq. (10) into (9), one obtains the integral formula for a complex function $g'(z_t)$.

$$g'(z_t) = \frac{1}{2\pi i} \left[\int_\Gamma \frac{g'(\tau_t) d\tau_t}{\tau_t - z_t} - \int_\Gamma \frac{g'(\bar{\tau}_t) d\bar{\tau}_t}{\bar{\tau}_t - z_t} \right]. \quad (11)$$

Using Eq. (5), we can construct an integral representation of a function $g'(z_t)$ using the boundary values of physical parameters ϑ and θ :

$$g'(z_t) = \frac{1}{4\pi i} \left[\int_\Gamma \frac{(\theta + i \frac{\vartheta}{k_t}) d\tau_t}{\tau_t - z_t} - \int_\Gamma \frac{(\theta - i \frac{\vartheta}{k_t}) d\bar{\tau}_t}{\bar{\tau}_t - z_t} \right]. \quad (12)$$

Eq. (12) can be reduced to the first-order curvilinear integrals:

$$g'(z_t) = -\frac{1}{4\pi i} \int_\Gamma \left[\frac{n_2(s) - p_t n_1(s)}{\tau_t(s) - z_t} - \frac{n_2(s) - \bar{p}_t n_1(s)}{\bar{\tau}_t(s) - z_t} \right] \theta(s) ds + \frac{1}{4\pi k_t} \int_\Gamma [\ln(\tau_t(s) - z_t) + \ln(\bar{\tau}_t(s) - z_t)] h_n(s) ds. \quad (13)$$

Based on Eqs (8) and (13), we obtain integral representations for temperature and heat flux at an arbitrary point ξ in the half-space $x_2 > 0$:

$$\theta(\xi) = 2\text{Re}\{g'(Z_t(\xi))\} = \int_\Gamma [\theta^{hs*}(\mathbf{x}, \xi) h_n(\mathbf{x}) - H^{hs*}(\mathbf{x}, \xi) \theta(\mathbf{x})] ds(\mathbf{x}), \quad (14)$$

$$h_i(\xi) = 2k_t \text{Im}\{(\delta_{2i} - \delta_{1i} p_t) g''(Z_t(\xi))\} = \int_\Gamma \theta_i^{hs**}(\mathbf{x}, \xi) h_n(\mathbf{x}) d\Gamma(\mathbf{x}) - \int_\Gamma H_i^{hs**}(\mathbf{x}, \xi) \theta(\mathbf{x}) ds(\mathbf{x}), \quad (15)$$

where the kernels are defined as:

$$\theta^{hs*}(\mathbf{x}, \xi) = \frac{1}{2\pi k_t} [\ln|Z_t(\mathbf{x} - \xi)| + \ln|\bar{Z}_t(\mathbf{x}) - Z_t(\xi)|], \quad (16)$$

$$H^{hs*}(\mathbf{x}, \xi) = \frac{1}{2\pi} \operatorname{Im} \left\{ \frac{n_2(\mathbf{x}) - p_t n_1(\mathbf{x})}{Z_t(\mathbf{x} - \xi)} - \frac{n_2(\mathbf{x}) - \bar{p}_t n_1(\mathbf{x})}{\bar{Z}_t(\mathbf{x}) - Z_t(\xi)} \right\}, \quad (17)$$

$$\Theta_i^{hs**} = -\frac{1}{2\pi} \operatorname{Im} \left\{ \frac{\delta_{i2} - p_t \delta_{i1}}{Z_t(\mathbf{x} - \xi)} + \frac{\delta_{i2} - \bar{p}_t \delta_{i1}}{\bar{Z}_t(\mathbf{x}) - Z_t(\xi)} \right\}, \quad (18)$$

$$H_i^{hs**} = -\frac{k_t}{2\pi} \operatorname{Re} \{ (\delta_{i2} - p_t \delta_{i1}) \times \left[\frac{n_2(\mathbf{x}) - p_t n_1(\mathbf{x})}{|Z_t(\mathbf{x} - \xi)|^2} - \frac{n_2(\mathbf{x}) - \bar{p}_t n_1(\mathbf{x})}{|\bar{Z}_t(\mathbf{x}) - Z_t(\xi)|^2} \right] \}. \quad (19)$$

Here, $Z_*(\mathbf{x}) = x_1 + p_* x_2$.

3.2. Thermoelasticity

Using the boundary conditions (8c) and (8d) and representation of complex potentials in Eq. (4), we can rewrite the integral along the boundary of the half-space in Eq. (6) as follows:

$$\int_{-\infty}^{\infty} \left\langle \frac{dx_1}{x_1 - z_*} \right\rangle \mathbf{f}(x_1) = \int_{-\infty}^{\infty} \left\langle \frac{dx_1}{x_1 - z_*} \right\rangle [\mathbf{B}^T \mathbf{u} + \mathbf{A}^T \boldsymbol{\varphi} - \mathbf{B}^T \mathbf{u}^t(x_1) - \mathbf{A}^T \boldsymbol{\varphi}^t(x_1)]. \quad (20)$$

As a result of integration by parts of Eq. (20) and the limitation of functions $\mathbf{u}^t(x_1)$ and $\boldsymbol{\varphi}^t(x_1)$, we obtain the following equation.

$$\int_{-\infty}^{\infty} \left\langle \frac{dx_1}{x_1 - z_*} \right\rangle \mathbf{f}(x_1) = \int_{-\infty}^{\infty} \left\langle \frac{dx_1}{x_1 - z_*} \right\rangle \mathbf{A}^T \boldsymbol{\varphi} + \int_{-\infty}^{\infty} \left\langle \frac{dx_1}{x_1 - z_*} \right\rangle \mathbf{B}^T \mathbf{u} + \int_{-\infty}^{\infty} \langle \ln(x_1 - z_*) \rangle \left[\mathbf{B}^T \frac{\partial \mathbf{u}^t(x_1)}{\partial x_1} + \mathbf{A}^T \frac{\partial \boldsymbol{\varphi}^t(x_1)}{\partial x_1} \right] dx_1. \quad (21)$$

Now consider that, according to Eqs (5) and (6) and the boundary conditions in Eqs (8a) and (8c):

$$\mathbf{B}^T \frac{\partial \mathbf{u}^t(x_1)}{\partial x_1} + \mathbf{A}^T \frac{\partial \boldsymbol{\varphi}^t(x_1)}{\partial x_1} = \mathbf{m} \theta, \quad (22)$$

where

$$\mathbf{m} = \mathbf{B}^T \operatorname{Re}[\mathbf{c}] + \mathbf{A}^T \operatorname{Re}[\mathbf{d}]. \quad (23)$$

Therefore, the Cauchy integral in Eq. (21) is written as

$$\int_{-\infty}^{\infty} \left\langle \frac{dx_1}{x_1 - z_*} \right\rangle \mathbf{f}(x_1) = \int_{-\infty}^{\infty} \left\langle \frac{dx_1}{x_1 - z_*} \right\rangle \mathbf{A}^T \boldsymbol{\varphi} + \int_{-\infty}^{\infty} \left\langle \frac{dx_1}{x_1 - z_*} \right\rangle \mathbf{B}^T \mathbf{u} + \int_{-\infty}^{\infty} \langle \ln(x_1 - z_*) \rangle \mathbf{m} \theta(x_1) dx_1. \quad (24)$$

Substituting Eq. (24) in Eq. (7), we can write:

$$\int_{-\infty}^{\infty} \left\langle \frac{dx_1}{x_1 - \bar{z}_*} \right\rangle [\mathbf{A}^T \boldsymbol{\varphi} + \mathbf{B}^T \mathbf{u}] = - \int_{\Gamma} \left\langle \frac{d\tau_*}{\tau_* - \bar{z}_*} \right\rangle \mathbf{f}(\tau_*) - \int_{-\infty}^{\infty} \langle \ln(x_1 - \bar{z}_*) \rangle \mathbf{m} \theta(x_1) dx_1. \quad (25)$$

Let us introduce the notation $\mathbf{A}^T \boldsymbol{\varphi} + \mathbf{B}^T \mathbf{u} = \mathbf{C} \mathbf{X}$, where $\mathbf{X} = \begin{pmatrix} \mathbf{u} \\ \boldsymbol{\varphi} \end{pmatrix}$, \mathbf{C} is a square matrix that will be formed on the basis of the matrix $(\mathbf{B}^T \mathbf{A}^T)$.

Now we can rewrite Eq. (25) in a slightly different manner:

$$\int_{-\infty}^{\infty} \left\langle \frac{dx_1}{x_1 - \bar{z}_*} \right\rangle [\mathbf{A}^T \boldsymbol{\varphi} + \mathbf{B}^T \mathbf{u}] = \int_{-\infty}^{\infty} \left\langle \frac{dx_1}{x_1 - \bar{z}_*} \right\rangle \mathbf{C} \mathbf{X} = - \int_{\Gamma} \left\langle \frac{d\tau_*}{\tau_* - \bar{z}_*} \right\rangle \mathbf{f}(\tau_*) - \int_{-\infty}^{\infty} \langle \ln(x_1 - \bar{z}_*) \rangle \mathbf{m} \theta(x_1) dx_1$$

or in complex conjugate form

$$\int_{-\infty}^{\infty} \left\langle \frac{dx_1}{x_1 - \bar{z}_*} \right\rangle \bar{\mathbf{C}} \mathbf{X} = \int_{-\infty}^{\infty} \left\langle \frac{dx_1}{x_1 - \bar{z}_*} \right\rangle [\bar{\mathbf{A}}^T \boldsymbol{\varphi} + \bar{\mathbf{B}}^T \mathbf{u}]$$

$$= - \int_{\Gamma} \left\langle \frac{d\bar{\tau}_*}{\bar{\tau}_* - z_*} \right\rangle \overline{\mathbf{f}(\tau_*)} - \int_{-\infty}^{\infty} \langle \ln(x_1 - z_*) \rangle \bar{\mathbf{m}} \theta(x_1) dx_1. \quad (26)$$

Accounting for the Stroh orthogonality relations, the first integral on the right side of Eq. (24) can be represented as

$$\int_{-\infty}^{\infty} \left\langle \frac{dx_1}{x_1 - z_*} \right\rangle [\mathbf{A}^T \boldsymbol{\varphi} + \mathbf{B}^T \mathbf{u}] = \int_{-\infty}^{\infty} \left\langle \frac{dx_1}{x_1 - z_*} \right\rangle \mathbf{C} \mathbf{X} = - \sum_{\beta=1}^3 \mathbf{I}_{\beta} \mathbf{C} \bar{\mathbf{C}}^{-1} \int_{-\infty}^{\infty} \left\langle \frac{dx_1}{x_1 - z_{\beta}} \right\rangle \bar{\mathbf{C}} \mathbf{X}. \quad (27)$$

Here, $\mathbf{I}_1 = \operatorname{diag}[1,0,0]$, $\mathbf{I}_2 = \operatorname{diag}[0,1,0]$ and $\mathbf{I}_3 = \operatorname{diag}[0,0,1]$.

Substituting Eq. (26) into Eq. (27) and taking into account the value received, Eq. (24) takes the form

$$\int_{-\infty}^{\infty} \left\langle \frac{dx_1}{x_1 - z_*} \right\rangle \mathbf{f}(x_1) = \sum_{\beta=1}^3 \int_{\Gamma} \left\langle \frac{d\bar{\tau}_{\beta}}{\bar{\tau}_{\beta} - z_*} \right\rangle \mathbf{C}^{-1} \bar{\mathbf{C}} \mathbf{I}_{\beta} \overline{\mathbf{f}(\tau_*)} + \int_{-\infty}^{\infty} \langle \ln(x_1 - z_*) \rangle [\mathbf{m} + \mathbf{C}^{-1} \bar{\mathbf{C}} \bar{\mathbf{m}}] \theta(x_1) dx_1, \quad (28)$$

and integrating Eq. (10) gives

$$\int_{-\infty}^{\infty} \langle \ln(x_1 - z_*) \rangle \theta(x_1) dx_1 = -2 \int_{\Gamma} \langle \ln(\bar{\tau}_t - z_*) \rangle \overline{g'(\tau_t)} d\bar{\tau}_t. \quad (29)$$

Therefore, the integral formula in Eq. (7) can be written in the form which does not contains integrals along the boundary of the half-space

$$\mathbf{f}(z_*) = \frac{1}{2\pi i} \left[\int_{\Gamma} \left\langle \frac{d\tau_*}{\tau_* - z_*} \right\rangle \mathbf{f}(\tau_*) + \sum_{\beta=1}^3 \int_{\Gamma} \left\langle \frac{d\bar{\tau}_{\beta}}{\bar{\tau}_{\beta} - z_*} \right\rangle \mathbf{C}^{-1} \bar{\mathbf{C}} \mathbf{I}_{\beta} \overline{\mathbf{f}(\tau_*)} - 2 \int_{\Gamma} \langle \ln(\bar{\tau}_t - z_*) \rangle [\mathbf{m} + \mathbf{C}^{-1} \bar{\mathbf{C}} \bar{\mathbf{m}}] d\bar{\tau}_t \right]. \quad (30)$$

Using Eqs (4) and (5), the integral formula in Eq. (30) takes the form:

$$\begin{aligned} \mathbf{f}(z_*) &= \frac{1}{2\pi i} \left[- \int_{\Gamma} \left\langle \frac{n_2(s) - p_* n_1(s)}{\tau_*(s) - z_*} \right\rangle \mathbf{B}^T \right. \\ &+ \sum_{\beta=1}^3 \left\langle \frac{n_2(s) - \bar{p}_{\beta} n_1(s)}{\bar{\tau}_{\beta}(s) - z_*} \right\rangle \mathbf{C}^{-1} \bar{\mathbf{C}} \mathbf{I}_{\beta} \mathbf{B}^T \left. \right] \mathbf{u}(s) ds \\ &+ \int_{\Gamma} \langle \ln(\tau_*(s) - z_*) \rangle \mathbf{A}^T \\ &+ \sum_{\beta=1}^3 \langle \ln(\bar{\tau}_{\beta}(s) - z_*) \rangle \mathbf{C}^{-1} \bar{\mathbf{C}} \mathbf{I}_{\beta} \mathbf{A}^T \left. \right] \mathbf{t}(s) ds \\ &- \int_{\Gamma} \langle \ln(\tau_*(s) - z_*) \rangle (\mathbf{A}^T \operatorname{Re}[\mathbf{d}(n_2 - n_1 p_t)]) \\ &+ \mathbf{B}^T \operatorname{Re}[\mathbf{c}(n_2 - n_1 p_t)] \theta(s) ds \\ &- \int_{\Gamma} \sum_{\beta=1}^3 \langle \ln(\bar{\tau}_{\beta}(s) - z_*) \rangle \mathbf{C}^{-1} \bar{\mathbf{C}} \mathbf{I}_{\beta} (\bar{\mathbf{A}}^T \operatorname{Re}[\mathbf{d}(n_2 - n_1 p_t)]) \\ &+ \bar{\mathbf{B}}^T \operatorname{Re}[\mathbf{c}(n_2 - n_1 p_t)] \theta(s) ds \\ &- \int_{\Gamma} \langle \ln(\bar{\tau}_t(s) - z_*) \rangle [n_2(s) - \bar{p}_t n_1(s)] [\mathbf{m} + \mathbf{C}^{-1} \bar{\mathbf{C}} \bar{\mathbf{m}}] \theta(s) ds \\ &- \frac{1}{k_t} \int_{\Gamma} \langle f^*(\tau_*(s) - z_*) \rangle (\mathbf{A}^T \operatorname{Im}[\mathbf{d}] + \mathbf{B}^T \operatorname{Im}[\mathbf{c}]) h_n(s) ds \\ &+ \frac{1}{k_t} \int_{\Gamma} \langle f^*(\bar{\tau}_t - z_*) \rangle [\mathbf{m} + \mathbf{C}^{-1} \bar{\mathbf{C}} \bar{\mathbf{m}}] h_n(s) ds \\ &- \frac{1}{k_t} \int_{\Gamma} \sum_{\beta=1}^3 \langle f^*(\bar{\tau}_{\beta}(s) - z_*) \rangle \mathbf{C}^{-1} \bar{\mathbf{C}} \mathbf{I}_{\beta} \\ &\times (\bar{\mathbf{A}}^T \operatorname{Im}[\mathbf{d}] + \bar{\mathbf{B}}^T \operatorname{Im}[\mathbf{c}]) h_n(s) ds. \end{aligned} \quad (31)$$

Based on Eqs (3), (9) and (31), one can derive the following Somigliana type integral identity for extended displacement at the arbitrary point ξ of thermoelastic half-space:

$$\mathbf{u}(\xi) = 2\text{Re}\{\mathbf{A}\mathbf{f}(Z_*(\xi)) + \mathbf{c}g(Z_t(\xi))\} = \int_{\Gamma} [\mathbf{U}^{hs}(\mathbf{x}, \xi)\mathbf{t}(\mathbf{x}) - \mathbf{T}^{hs}(\mathbf{x}, \xi)\mathbf{u}(\mathbf{x}) + \mathbf{r}^{hs}(\mathbf{x}, \xi)\theta(\mathbf{x}) + \mathbf{v}^{hs}(\mathbf{x}, \xi)h_n(\mathbf{x})]ds(\mathbf{x}). \quad (32)$$

Here, the kernels are defined as:

$$\mathbf{U}^{hs}(\mathbf{x}, \xi) = \frac{1}{\pi} \text{Im}[\mathbf{A}\langle \ln Z_*(\mathbf{x} - \xi) \rangle] \mathbf{A}^T + \mathbf{A} \sum_{\beta=1}^3 \left\langle \ln \left(\bar{Z}_{\beta}(\mathbf{x}) - Z_*(\xi) \right) \right\rangle \mathbf{C}^{-1} \bar{\mathbf{C}}\mathbf{I}_{\beta} \bar{\mathbf{A}}^T; \quad (33)$$

$$\mathbf{v}^{hs}(\mathbf{x}, \xi) = -\frac{1}{\pi k_t} \text{Im}[\mathbf{A}\langle f^*(Z_*(\mathbf{x} - \xi)) \rangle] (\mathbf{A}^T \text{Im}[\mathbf{d}] - \mathbf{B}^T \text{Im}[\mathbf{c}]) - \frac{1}{\pi k_t} \text{Im} \left[\sum_{\beta=1}^3 \mathbf{A} \langle f^*(\bar{Z}_{\beta}(\mathbf{x}) - Z_*(\xi)) \rangle \mathbf{C}^{-1} \bar{\mathbf{C}}\mathbf{I}_{\beta} \times (\bar{\mathbf{A}}^T \text{Im}[\mathbf{d}] + \bar{\mathbf{B}}^T \text{Im}[\mathbf{c}]) - \frac{1}{2\pi k_t} \text{Re}[\mathbf{c}\langle f^*(Z_t(\mathbf{x} - \xi)) + f^*(\bar{Z}_t(\mathbf{x}) - Z_t(\xi)) \rangle] + \frac{1}{\pi k_t} \text{Re}[\mathbf{A}\langle f^*(\bar{Z}_t(\mathbf{x}) - Z_*(\xi)) \rangle] \times (\mathbf{m} + \mathbf{C}^{-1} \bar{\mathbf{C}}\bar{\mathbf{m}}) \right]; \quad (34)$$

$$\mathbf{T}^{hs}(\mathbf{x}, \xi) = \frac{1}{\pi} \text{Im} \left[\mathbf{A} \left\langle \frac{n_2(\mathbf{x}) - p_* n_1(\mathbf{x})}{Z_*(\mathbf{x} - \xi)} \right\rangle \mathbf{B}^T + \mathbf{A} \sum_{\beta=1}^3 \left\langle \frac{n_2(\mathbf{x}) - \bar{p}_{\beta} n_1(\mathbf{x})}{\bar{Z}_{\beta}(\mathbf{x}) - Z_*(\xi)} \right\rangle \mathbf{I}_{\beta} \mathbf{C}^{-1} \bar{\mathbf{C}} \bar{\mathbf{B}}^T \right] \text{ and} \quad (35)$$

$$\mathbf{r}_i^{hs}(\mathbf{x}, \xi) = -\frac{1}{\pi} \text{Im}[\mathbf{A}\langle \ln Z_*(\mathbf{x} - \xi) \rangle] (\mathbf{A}^T \text{Re}\{\mathbf{d}(n_2 - p_t n_1)\} + \mathbf{B}^T \text{Re}\{\mathbf{c}(n_2 - p_t n_1)\}) - \frac{1}{\pi} \text{Im} \sum_{\beta=1}^3 \left[\mathbf{A} \left\langle \ln \left(\bar{Z}_{\beta}(\mathbf{x}) - Z_*(\xi) \right) \right\rangle \times \mathbf{C}^{-1} \bar{\mathbf{C}}\mathbf{I}_{\beta} (\bar{\mathbf{A}}^T \text{Re}\{\mathbf{d}(n_2 - p_t n_1)\} + \bar{\mathbf{B}}^T \text{Re}\{\mathbf{c}(n_2 - p_t n_1)\}) - \frac{1}{\pi} \text{Im}[\mathbf{A}\langle \ln(\bar{Z}_t(\mathbf{x}) - Z_*(\xi)) \rangle] \mathbf{A}^{-1} \text{Re}[\mathbf{c}(n_2 - \bar{p}_t n_1)] + \frac{1}{\pi} [\mathbf{c}[n_2 - p_t n_1] \ln Z_t(\mathbf{x} - \xi) - (n_2 - \bar{p}_t n_1) \ln(\bar{Z}_t(\mathbf{x}) - Z_*(\xi))] \right]. \quad (36)$$

Here, $Z_*(\mathbf{x}) = x_1 + p_* x_2$.

Eqs (5), (13) and (31) yield the following integral formula for the components of the extended stress tensor:

$$\sigma_{ij}(\xi) = [\sigma_{ij}(\xi)] = 2\text{Re}\{\mathbf{B}(\delta_{2j} - \delta_{1j}P)\mathbf{f}'(Z_*(\xi)) + \mathbf{d}(\delta_{2j} - \delta_{1j}p_t)g'(Z_t(\xi))\} = \int_{\Gamma} \mathbf{D}_j^{hs}(\mathbf{x}, \xi)\mathbf{t}(\mathbf{x})ds(\mathbf{x}) - \int_{\Gamma} \mathbf{S}_j^{hs}(\mathbf{x}, \xi)\mathbf{u}(\mathbf{x})ds(\mathbf{x}) + \int_{\Gamma} \mathbf{q}_j^{hs}(\mathbf{x}, \xi)\theta(\mathbf{x})ds(\mathbf{x}) + \int_{\Gamma} \mathbf{w}_j^{hs}(\mathbf{x}, \xi)h_n(\mathbf{x})ds(\mathbf{x}). \quad (37)$$

Here

$$\mathbf{q}_{ij}^{hs}(\mathbf{x}, \xi) = -\frac{1}{\pi} \text{Im} \left\{ \mathbf{B} \left\langle \frac{\delta_{2j} - p_* \delta_{1j}}{Z_*(\mathbf{x} - \xi)} \right\rangle \times (\mathbf{A}^T \text{Re}\{\mathbf{d}(n_2 - p_t n_1)\} + \mathbf{B}^T \text{Re}\{\mathbf{c}(n_2 - p_t n_1)\}) \right\} + \frac{1}{\pi} \text{Im} \left\{ \mathbf{B} \sum_{\beta=1}^3 \left\langle \frac{\delta_{2j} - p_* \delta_{1j}}{\bar{Z}_{\beta}(\mathbf{x}) - Z_*(\xi)} \right\rangle \mathbf{C}^{-1} \bar{\mathbf{C}}\mathbf{I}_{\beta} \times (\bar{\mathbf{A}}^T \text{Re}\{\mathbf{d}(n_2 - p_t n_1)\} + \bar{\mathbf{B}}^T \text{Re}\{\mathbf{c}(n_2 - p_t n_1)\}) \right\} - \frac{1}{\pi} \text{Im} \left\{ \mathbf{B} \left\langle \frac{\delta_{2j} - p_* \delta_{1j}}{\bar{Z}_{\beta}(\mathbf{x}) - Z_*(\xi)} \right\rangle \mathbf{A}^{-1} \text{Re}[\mathbf{c}(n_2 - \bar{p}_t n_1)] \right\}$$

$$- \frac{1}{2\pi} \text{Im} \left\{ \mathbf{d}(\delta_{2j} - p_* \delta_{1j}) \left[\frac{\delta_{2j} - p_* \delta_{1j}}{Z_*(\mathbf{x} - \xi)} - \frac{\delta_{2j} - \bar{p}_* \delta_{1j}}{\bar{Z}_t(\mathbf{x}) - Z_t(\xi)} \right] \right\};$$

$$\mathbf{w}_{ij}^{hs}(\mathbf{x}, \xi) = \frac{1}{\pi k_t} \text{Im}[-\mathbf{B}\langle (\delta_{2j} - \delta_{1j}P_*) \ln Z_*(\mathbf{x} - \xi) \rangle] \times (\mathbf{B}^T \text{Im}[\mathbf{c}] + \mathbf{A}^T \text{Im}[\mathbf{d}]) + \frac{1}{\pi k_t} \text{Im} \left[\sum_{\beta=1}^3 \mathbf{B}\langle (\delta_{2j} - \delta_{1j}P_*) \ln \bar{Z}_{\beta}(\mathbf{x}) - Z_*(\xi) \rangle \times \mathbf{C}^{-1} \bar{\mathbf{C}}\mathbf{I}_{\beta} (\bar{\mathbf{B}}^T \text{Im}[\mathbf{c}] + \bar{\mathbf{A}}^T \text{Im}[\mathbf{d}]) \right] - \frac{1}{\pi k_t} \text{Re} \left[\sum_{\beta=1}^3 \mathbf{B}\langle (\delta_{2j} - \delta_{1j}P_*) \ln \bar{Z}_t(\mathbf{x}) - Z_*(\xi) \rangle \mathbf{A}^{-1} \text{Re}[\mathbf{c}] \right] + \frac{1}{2\pi k_t} \text{Re}[\mathbf{d}(\delta_{2j} - \delta_{1j}P_t(\ln Z_t(\mathbf{x} - \xi) + \ln(\bar{Z}_t(\mathbf{x}) - \ln Z_t(\xi)))];$$

$$\mathbf{D}_{ijk}^{hs}(\mathbf{x}, \xi) = -\frac{1}{\pi} \text{Im} \left\{ \mathbf{B} \left[\left\langle \frac{\delta_{2j} - p_* \delta_{2j}}{Z_*(\mathbf{x} - \xi)} \right\rangle \mathbf{A}^T + \sum_{\beta=1}^4 \left\langle \frac{\delta_{2j} - p_* \delta_{1j}}{\bar{Z}_{\beta}(\mathbf{x}) - Z_*(\xi)} \right\rangle \mathbf{C}^{-1} \bar{\mathbf{C}}\mathbf{I}_{\beta} \bar{\mathbf{A}}^T \right] \right\} \text{ and}$$

$$\mathbf{S}_{ijk}^{hs}(\mathbf{x}, \xi) = \frac{1}{\pi} \text{Im} \left\{ \mathbf{B} \left\langle \frac{(\delta_{2j} - p_* \delta_{1j})(n_2 - p_* n_1)}{(Z_*(\mathbf{x} - \xi))^2} \right\rangle \mathbf{B}^T \right\} + \frac{1}{\pi} \text{Im}\{\mathbf{B}(\delta_{2j} - p_* \delta_{1j})\} \times \sum_{\beta=1}^4 \left\langle \frac{(n_2 - \bar{p}_* n_1)}{(\bar{Z}_{\beta}(\mathbf{x}) - Z_*(\xi))^2} \right\rangle \mathbf{C}^{-1} \bar{\mathbf{C}}\mathbf{I}_{\beta} \bar{\mathbf{B}}^T. \quad (38)$$

Thus, for the problem with boundary conditions in Eqs (8a) and (8c), appropriate integral representations can be obtained.

4. NUMERICAL EXAMPLES

Sample problem is considered for an anisotropic (fibreglass) thermoelastic half-plane $x_2 > 0$ under the action of a uniform heat flow directed along its boundary, which contains internal thin, rectilinear thermoelastic isotropic inclusion (Fig. 1). Its length is $l = 2a$ and thickness is $h = 0,01a$, and it is located at a distance $d = a$ to the edge of the half-space. Properties of the half-space are as follows: $E_1 = 55$ GPa, $E_2 = 21$ GPa, $G_{12} = 9.7$ GPa, $\nu_{12} = 0.25$, $\alpha_{11} = 6.3 \times 10^{-6} \text{ K}^{-1}$, $\alpha_{22} = 2.0 \times 10^{-5} \text{ K}^{-1}$, $k_{11} = 3.46 \text{ W/(m}\cdot\text{K)}$ and $k_{22} = 0.35 \text{ W/(m}\cdot\text{K)}$. The values of these constants are given in the direction of the main axes of the anisotropy of the material. Inclusion is assumed to be thermally insulated and possesses no thermal expansion.

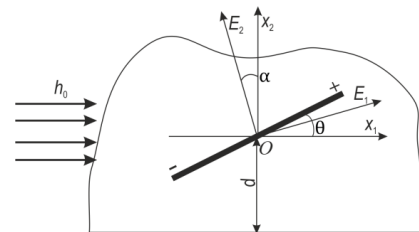


Fig. 1. Thermoelastic anisotropic half-plane with thin inclusion

Figs 2–9 show the relationship between the generalised stress intensity factors (SIF) and the relative rigidity $k = G^i/G_{12}$ (G^i is the shear modulus of inclusion) of the inclusion, under the boundary conditions in Eqs (8a) and (8c) at different values of inclusion inclination angle θ . The normalising SIF $K_0 =$

$\alpha\sqrt{\pi a} \cdot E_1 \times \alpha_{11}/k_{11} \cdot h_0$. Dashed lines show cases when the influence of inclusion bending is excluded from its model. As can be seen from the plot, this effect is significant, and therefore requires careful analysis.

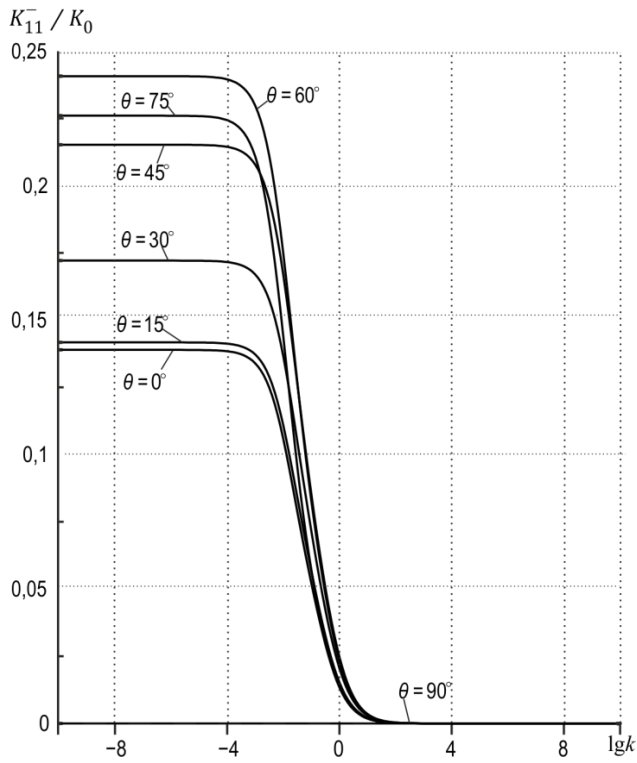


Fig. 2. The relationship between SIF K_{11}^- / K_0 and the generalised stiffness at different values of θ

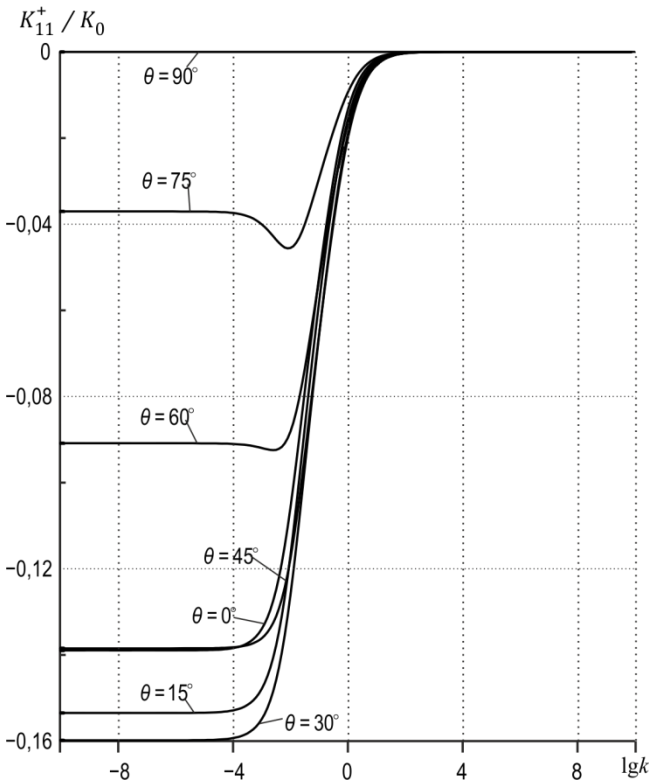


Fig. 3. The relationship between SIF K_{11}^+ / K_0 and the generalised stiffness at different values of θ

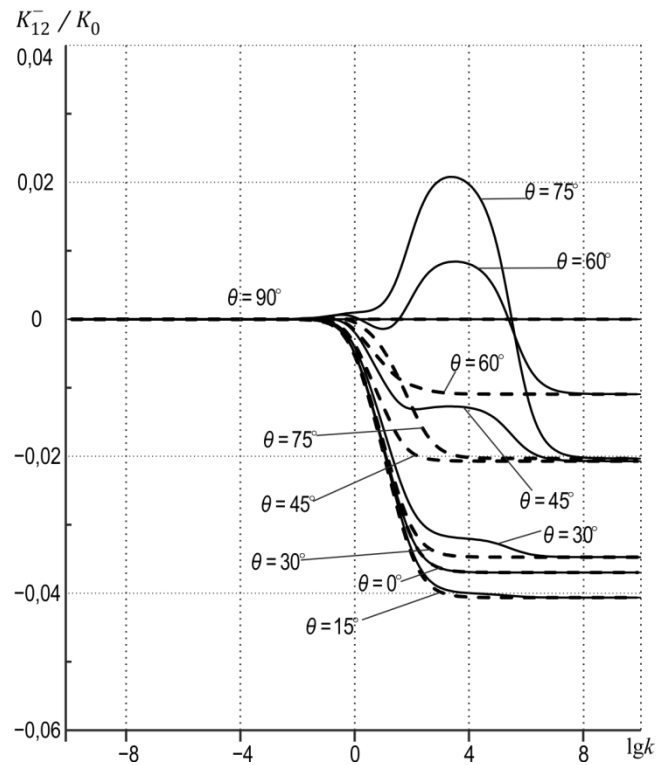


Fig. 4. The relationship between SIF K_{12}^- / K_0 and the generalised stiffness at different values of θ

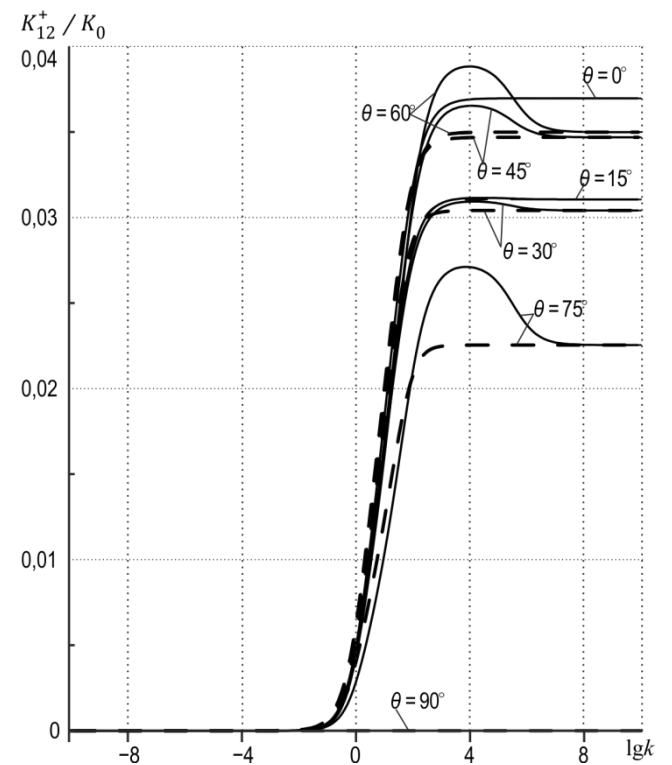


Fig. 5. The relationship between SIF K_{12}^+ / K_0 and the generalised stiffness at different values of θ

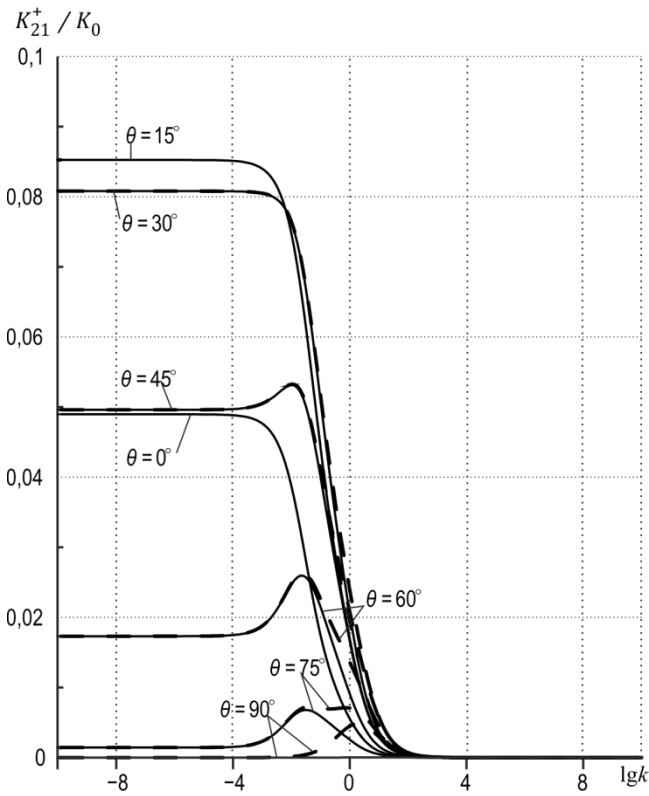


Fig. 6. The relationship between SIF K_{21}^+ / K_0 and the generalised stiffness at different values of θ

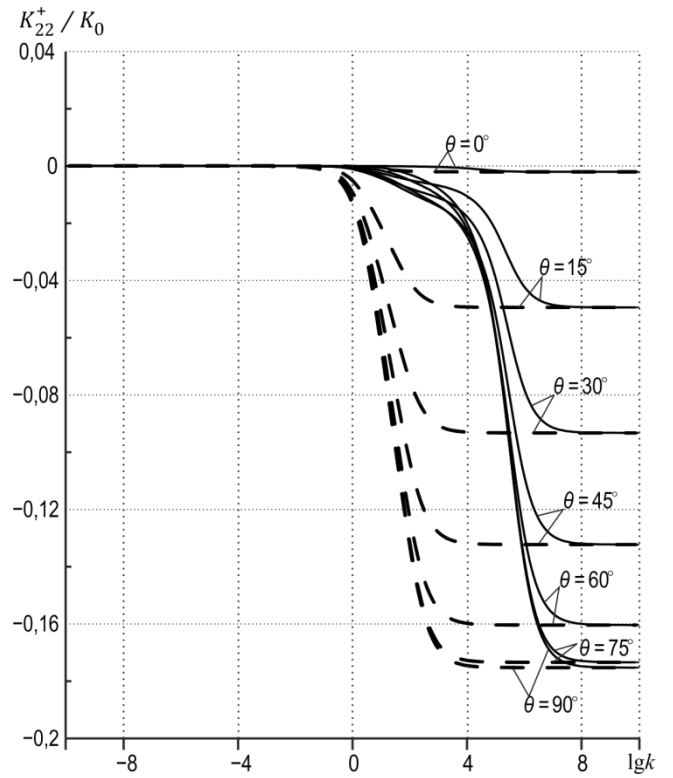


Fig. 8. The relationship between SIF K_{22}^+ / K_0 and the generalised stiffness at different values of θ

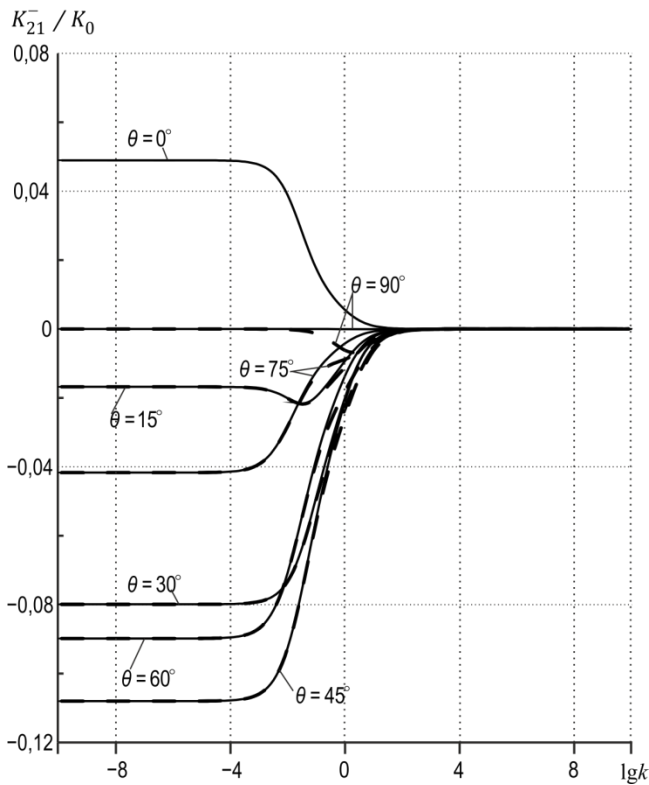


Fig. 7. The relationship between SIF K_{21}^- / K_0 and the generalised stiffness at different values of θ

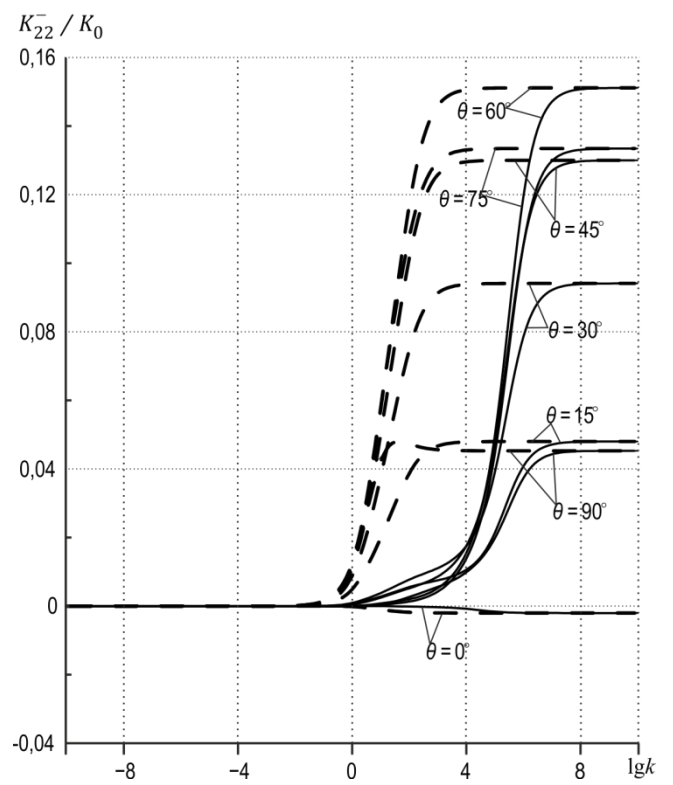


Fig. 9. The relationship between SIF K_{22}^- / K_0 and the generalised stiffness at different values of θ

In Figs 2 and 3, we see that the inclusion bending does not affect the values of the SIFs K_{11}^+/K_0 and K_{11}^-/K_0 . It should also be noted that the maximum value of the SIFs K_{11}^-/K_0 is reached when the inclusion is at the angle $\theta = 60^\circ$ to the boundary of the half-space. At $l g k < -4$, the values of the SIFs do not change, and at $l g k > -4$ (except in case of $\theta = 75^\circ$), they monotonically tend to become zero.

In Figs 4–9, it can be seen that the bending of the inclusion significantly affects the values of the SIFs. This is especially noticeable in Fig. 4, when $\theta = 75^\circ$ and $\theta = 60^\circ$. As mentioned earlier, this effect requires careful analysis.

One can see in Figs 8 and 9 that below $l g k = 4$, the values of the SIFs grow slowly and above $l g k > 4$, their growth is intense. When the influence of inclusion bending is excluded from consideration, we can see that the SIFs K_{22}^+/K_0 and K_{22}^-/K_0 increase monotonously even at $l g k = 0$ and tend their maximum values faster.

5. CONCLUSIONS

The paper presents a simple and straightforward approach for obtaining the Somigliana type integral formulae and corresponding dual boundary integral equations for an anisotropic thermoelastic half-space with mixed boundary conditions on its surface.

Integral equations in conjunction with the scheme of the modified BEM allow solving a number of new problems for the thermoelastic half-plane containing cracks or thin deformable inclusions.

A numerical analysis of the influence of boundary conditions on the half-space boundary and the relative rigidity of the thin inhomogeneity on stress intensity at the inclusions is provided.

REFERENCES

1. **Bozhydarnyk V., Pasternak I., Sulym H., Oliarynyk N.** (2011), BEM approach for the antiplane shear of anisotropic solids containing thin inhomogeneities, *Acta mechanica et automatica*, 5(4), 11–16.
2. **Chen H., Wang Q., Liu G. R., Wang Y., Sun J.** (2016), Simulation of thermoelastic crack problems using singular edge-based smoothed finite element method, *International Journal of Mechanical Sciences*, 115–116, 123–134.
3. **Hou P.F.** (2011), 2D general solution and fundamental solution for orthotropic thermoelastic materials, *Engineering Analysis with Boundary Elements*, 35, 56–60.
4. **Hwu C.** (2010), *Anisotropic elastic plates*, Springer, London.
5. **Li X.Y.** (2012), Exact fundamental thermo-elastic solutions of a transversely isotropic elastic medium with a half infinite plane crack, *International Journal of Mechanical Sciences*, 59(1), 83–94.
6. **Mukherjee Y.X.** (1999), Thermoelastic fracture mechanics with regularized hypersingular boundary integral equations, *Engineering Analysis with Boundary Elements*, 23, 89–96.
7. **Pasternak I., Pasternak R., Sulym H.** (2013), Boundary integral equations for 2D thermoelasticity of a half-space with cracks and thin inclusions, *Engineering Analysis with Boundary Elements*, 37, 1514–1523.
8. **Pasternak I.** (2012), Boundary integral equations and the boundary element method for fracture mechanics analysis in 2D anisotropic thermoelasticity, *Engineering Analysis with Boundary Elements*, 36(12), 1931–1941.
9. **Qin Q.** (1999), Thermoelastic analysis of cracks in piezoelectric half-plane by BEM, *Computational Mechanics*, 23, 353–360.
10. **Şeremet V.** (2011), Deriving exact Green's functions and integral formulas for a thermoelastic wedge, *Engineering Analysis with Boundary Elements*, 35(3), 527–532.
11. **Sherief H.H., Abd El-Latif A.M.** (2014), Application of fractional order theory of thermoelasticity to a 2D problem for a half-space, *Applied Mathematics and Computation*, 248, 584–592.
12. **Shiah Y.C.** (2000), Fracture mechanics analysis in 2-D anisotropic thermoelasticity using BEM, *CMES*, 1(3), 91–99.
13. **Sulym H.T.** (2007), *Bases of mathematical theory of thermo-elastic equilibrium of solids containing thin inclusions*, Research and Publishing center of NTSh, 2007 (in Ukrainian).
14. **Tokovyy Y., Ma C-C.** (2009), An explicit-form solution to the plane elasticity and thermoelasticity problems for anisotropic and inhomogeneous solids, *Int J Solids Struct*, 46(21), 3850–9.
15. **Woo H-G., Li H.** (2011), *Advanced functional materials*, Springer, London.
16. **Wu W-L.** (2009), Dual Boundary Element Method Applied to Antiplane Crack Problems, *Mathematical Problems in Engineering*, doi:10.1155/2009/132980.
17. **Yang W., Zhou Q., Zhai Yu, Lyu D., Huang Y., Wang J., Jin X., Keer M.L., Wang Q.J.** (2019), Semi-analytical solution for steady state heat conduction in a heterogeneous half space with embedded cuboidal inhomogeneity, *International Journal of Thermal Sciences*, 139, 326–338.

The present paper is financially supported by the Ministry of Science and Higher Education of Poland (research project No. S/WMM/4/2017) and realised in Białystok University of Technology.

STRESS CONCENTRATION AT LOAD-CARRYING FILLET WELDED CRUCIFORM JOINTS SUBJECTED TO TENSILE AND BENDING LOADS

Krzysztof L. MOLSKI*

*Bialystok University of Technology, ul. Wiejska 45C, 15-351 Bialystok, Poland

k.molski@pb.edu.pl

received 25 November 2019, revised 13 December 2019, accepted 18 December 2019

Abstract: This article presents numerical finite element method (FEM) analysis of the stress concentration at toes and crack-like faults in load-carrying fillet welded cruciform joints with transversal slits resulting from non-fused root faces. Potential fatigue damage of such joints subjected to cyclic tensile and bending loads appears in the form of fatigue cracks starting from the weld roots or toes. The aim of this article is to find qualitative and quantitative relationships between geometrical parameters of the load-carrying fillet welded cruciform joint subjected to tensile and bending loads and the stress concentration at weld toes and roots. The results of the analysis represented by the stress concentration factors (SCFs) and the stress intensity factors K_I and K_{II} are shown in the form of tables, graphs and mathematical formulas, which may be applied for fatigue assessment of such joints.

Key words: cruciform welded joint, load-carrying fillets, stress concentration factor, stress intensity factor, finite element method

1. INTRODUCTION

Cruciform welded joints are commonly used in engineering practice. There are two general types of such connections known as the 'non-load carrying fillet welded joints' and the 'load-carrying fillet welded joints'. In the first type, the external loads are sustained by the main plate with additional transversal stiffeners, whereas, in the latter, the loads pass through the fillet welds. Besides, both types of joints may have un-fused root faces producing the so-called 'lack of penetration defects'.

It is well known that fatigue fracture produced by fluctuating loads is the most common damage mechanism of welded connections. Therefore, the weakest points determining fatigue life of the structure are related to particular zones of high stress concentration located at a weld toe and at the apex of existing slits. Fatigue life of such connections may be estimated in many ways, taking into account possible damage mechanisms, including crack location and its possible growth. Some details of different approaches used for the assessment of fatigue life can be found in the literature (e.g. in Peterson, 1974; Monahan, 1995; Singh et al., 2002; Chung et al., 2008; Wooryong and Chitoshi, 2008; Radaj et al., 2009; Chattopadhyay et al., 2011; Sonsino et al., 2012; Singh et al., 2003; Livieri and Lazzarin, 2005; Dong, 2001; Lotsberg and Sigurdsson, 2006; Stenberg et al., 2015; Remes, and Varsta, 2010; Kranz and Sonsino, 2010; Schijve, 2012; Zerbst et al., 2016; Niemi et al., 2018; Tchoffo et al., 2017). Numerous design procedures have also been developed and published in the form of standards and recommendations (e.g. Young and Lawrence, 1985; CES, 2005; Hobbacher, 2009; Fricke, 2012; Fricke, 2013; ISO, 2013). Many solutions to stress concentration factors (SCFs) regarding various types of weldments have also been published (e.g. in Ushirokawa and Nakayama, 1983; Tsuji, 1990; Iida and Uemura, 1996; Molski et al., 2019).

The assessment of fatigue life requires high accuracy of SCFs solutions. As shown in Molski et al. (2019), several percentages of errors in estimating maximum stress range may lead in some circumstances up to 200% inaccuracy in estimating fatigue life. Therefore, SCF approximation formulas should be highly accurate and cover wide range of values of all basic geometrical parameters, determining shape of the joint and influencing SCF.

The fatigue strength of the load-carrying fillet welded cruciform joints with the lack of penetration defects is generally lower than that for the non-load carrying joints because of the fact that un-fused root faces are in transverse position to the main plate. Such a location of both slits may produce high stress concentration at the vicinity of each apex and additionally increases the maximum stress at the weld toe.

The present work deals with the determination of SCFs and the stress intensity factors K_I and K_{II} in the weld region of a load-carrying fillet welded cruciform joint subjected to tensile and bending loads.

2. GENERAL ASSUMPTIONS AND MODELLING STRATEGY

The shape and the basic geometrical parameters of the joint under consideration subjected to tensile and bending loads are shown in Figure 1. Two zones located at the weld toe and at the apex of the slit, denoted by A and B, respectively, represent the places where significant increase of stresses is expected.

As the toe radius $\rho > 0$, the maximum stress is finite and can be represented by the stress concentration factor K_t^t for tensile and K_b^t for bending load, respectively. In the case of un-fused crack-like defect, two stress intensity factors have to be determined separately for each loading mode. For convenience, both SCFs for tension and bending may be represented by the following equations:

$$K_t^t = K_{t0}^t F^t \tag{1}$$

$$K_t^b = K_{t0}^b F^b \tag{2}$$

as a product of the known stress concentration factors K_{t0}^t and K_{t0}^b for fully penetrated welds and the unknown correction functions F^t and F^b that have to be determined. An extended review of published formulas dealing with K_{t0}^t and K_{t0}^b for these weldments is presented in Ushirokawa and Nakayama (1983) Tsuji (1990) and Iida and Uemura (1996), and, therefore, they will not be quoted here.

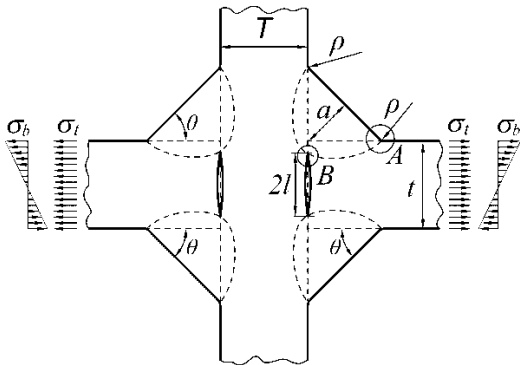


Fig. 1. General shape and loading conditions of the load-carrying fillet welded cruciform joint with two crack-like slits

In the case of stress intensity factors K_I and K_{II} , it is convenient to introduce the following general formula:

$$K_j = \sigma \sqrt{\pi l} F_{K_j} \tag{3}$$

where σ represents the remote nominal stress and F_{K_j} is a correction function that has to be determined. The subscript j indicates the loading mode of the joint.

There are several geometrical parameters characterising the shape of the weldment, as weld toe radius ρ , nominal throat thickness a , weld face angle θ , thickness of the main plate t and so on. It was supposed that the weld face angle $\theta = 45^\circ$ and the ratios of other parameters change in the following ranges: $0.1 \leq \rho/a \leq 0.5$, $0.25 \leq a/t \leq 1$, $0 \leq 2l/t \leq 1$ and $0.5 \leq T/t \leq 2$, which usually apply to weldments in engineering structures. Many particular values of geometrical parameters were chosen in each range depending on the values of calculated correction functions. For example, the ρ/a parameter was changed by a step of 0.1, whereas T/t parameter was changed by a step of 0.5. In cases of two remaining parameters, 5 – 10 different values were chosen from the appropriate range.

Numerical finite element method (FEM) modelling of the joint has been carried out using ANSYS 19 MultiPhysics program and PLANE 182 type of finite elements. The material of the body is linear-elastic, isotropic and homogeneous. Small deformations occur because of external load. Both load-carrying main plates of the same thickness t are co-linear, and the shape of all fillet welds is identical.

Shape of the body as well as loading and displacement boundary conditions of the cruciform joints are shown in Figure 2.

About 200,000 finite elements were used for each model and a special attention has been given to the finite element mesh density at the weld critical zones A and B, which is shown in Figure 3. In the first case, the arc of the toe radius ρ was described by at least 40 elements. In the second case, the use of a very fine mesh was necessary with special triangular elements located at the core around the crack tip. Such a modelling strategy is appropriate for approximating the stress singularity and makes the stress field around the crack tip proportional to $r^{-0.5}$ according to the exact analytical solution based on the theory of elasticity.

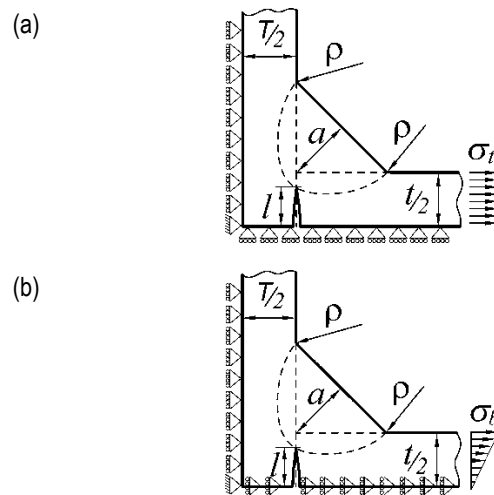


Fig. 2. Geometry and loading conditions – (a) tensile and (b) bending – of the modelled element

3. RESULTS AND DISCUSSION

Several hundred numerical FEM solutions have been obtained for the loaded joints, which are shown in Figure 2. One example of such a solution for tensile load is presented in Figure 3, where critical zones of increased stress concentration are clearly seen.

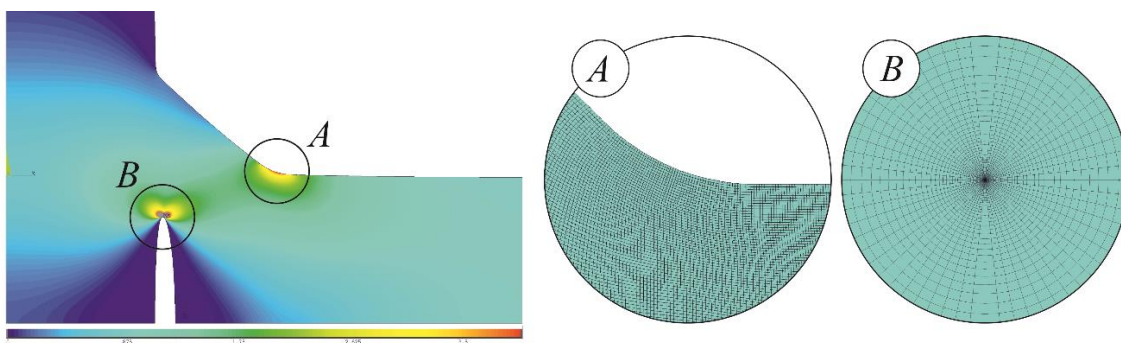


Fig. 3. Distribution of the principal stress component σ_1 in the joint subjected to tension. Details A and B show the finite element mesh in both critical zones

The calculated maximum principal stresses at the weld toe were compared to the nominal ones and divided by the particular reference values of K_{t0}^t and K_{t0}^b obtained in the same way for joints without the lack of penetration defects. Such a procedure made it possible to calculate particular values of correction parameters F^t and F^b using equations (1) and (2). Using equation (3), the values of correction parameters $F_{K_j}^t$ and $F_{K_j}^b$ have been obtained in a similar way.

The detailed analysis of the results led to the conclusion that two shape parameter ratios l/t and a/t are the most important and have significant impact on the values of all correction parameters. Other geometrical ratios of p/a and T/t have minor influence on all F^t , F^b , $F_{K_j}^t$ and $F_{K_j}^b$. The maximum changes in correction parameters for the weld toe because of p/a and T/t are about 5%, whereas for the apex of the transverse, cracks do not exceed 1%. It is also important to note that for tensile loading, the stress intensity factor, K_{II} , is about 8–15 times lower than K_I and, therefore, may be omitted in the procedures of fatigue life assessment.

In the case of bending load, both stress intensity factors K_I and K_{II} are of the same order. In spite of the fact that their values are much lower than K_I for tension under the same nominal stress, both loading modes – tension and bending – are independently applied in the real structures, which means that their proportions are generally not known.

It is important to note that from a theoretical point of view, if pure bending load is applied, one half of the central slit is open, whereas the other tends to be closed. As mutual penetration of both crack faces under compression is not physically possible, some additional comments are necessary. Generally, there are two reasons confirming the solution is reasonable. The first reason is that welding process never introduces a perfect crack. The un-fused faces are usually slightly separated and such a penetration may not occur or may be very limited. The second reason is that bending load usually acts together with the accompanying tensile load, producing additional opening of the slit. This leads to the conclusion that real conditions inside the weldment are in fact unknown and the assumptions made here are rational enough to explain the applicability of the solution to the assessment of fatigue life.

Some examples of particular values of correction parameters, transformed later into correction functions are presented in Tables 1–5 and shown in Figures 4–8. Mathematical formulas (A1)–(A5) derived from numerical solutions and appropriate for the assessment of fatigue life of the load-carrying fillet welded cruciform joint are presented in Appendix. The accuracy of those equations does not exceed 1% compared to the numerical FEM solutions.

Table 1. Numerical values of the correction function F^t

$p/a=0.5$		$2l/t$					
a/t	K_{t0}^t	0.0	0.25	0.50	0.75	0.90	1.0
0.25	2.207	1.0	1.072	1.311	1.773	2.179	2.502
0.333	2.053	1.0	1.061	1.245	1.558	1.809	2.002
0.4	1.960	1.0	1.048	1.190	1.420	1.599	1.734
0.6	1.759	1.0	1.020	1.077	1.167	1.237	1.289
0.8	1.624	1.0	1.007	1.028	1.061	1.087	1.107
1.0	1.526	1.0	1.003	1.009	1.021	1.029	1.035

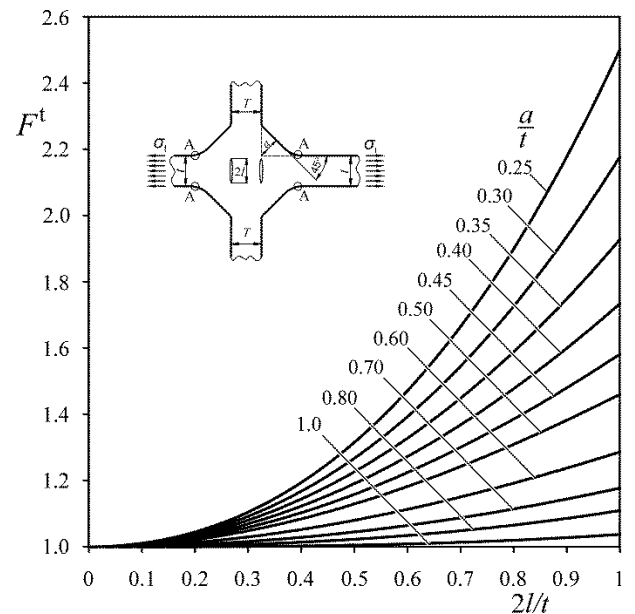


Fig. 4. Correction function F^t for calculating $K_{K_j}^t$ at a weld toe of a load-carrying fillet welded cruciform joint with a lack of penetration defect and subjected to tensile load

Table 2. Numerical values of correction function $F_{K_j}^t$

a/t	$2l/t$					
	0.10	0.25	0.50	0.75	0.90	1.0
0.25	0.826	0.832	0.868	0.960	1.051	1.131
0.333	0.786	0.788	0.807	0.859	0.910	0.954
0.4	0.752	0.751	0.759	0.791	0.824	0.823
0.6	0.648	0.643	0.635	0.638	0.646	0.655
0.8	0.562	0.554	0.541	0.534	0.534	0.537
1.0	0.492	0.485	0.471	0.459	0.456	0.456

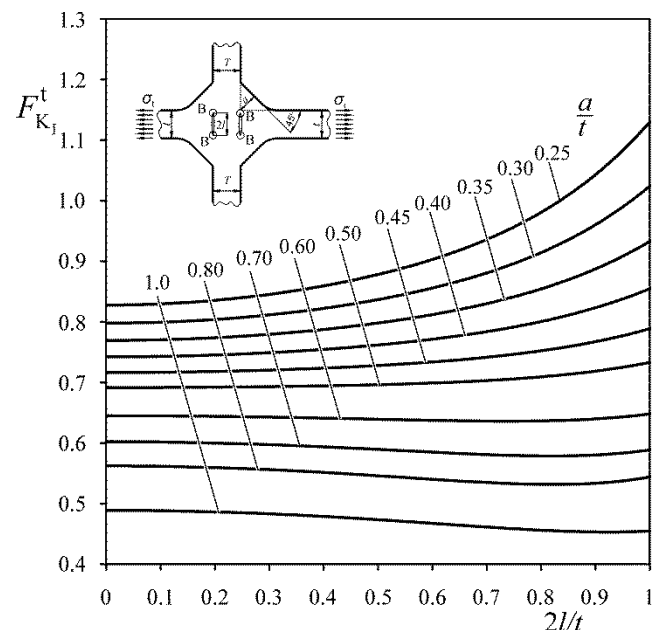


Fig. 5. Correction function $F_{K_j}^t$ for calculating $K_{K_j}^t$ at the apex of a lack of penetration defect in the load-carrying fillet welded cruciform joint subjected to tensile load

Table 3. Numerical values of the correction function F^b

$\rho a=0.5$		$2l/t$					
alt	K_{t0}^b	0.0	0.25	0.50	0.75	0.90	1.0
0.25	1.784	1.0	1.011	1.052	1.143	1.223	1.282
0.333	1.647	1.0	1.006	1.027	1.065	1.095	1.115
0.4	1.568	1.0	1.003	1.014	1.033	1.046	1.056
0.6	1.416	1.0	1.0	1.001	1.003	1.005	1.006
0.8	1.328	1.0	1.0	1.0	1.0	1.0	1.0
1.0	1.271	1.0	1.0	1.0	1.0	1.0	1.0

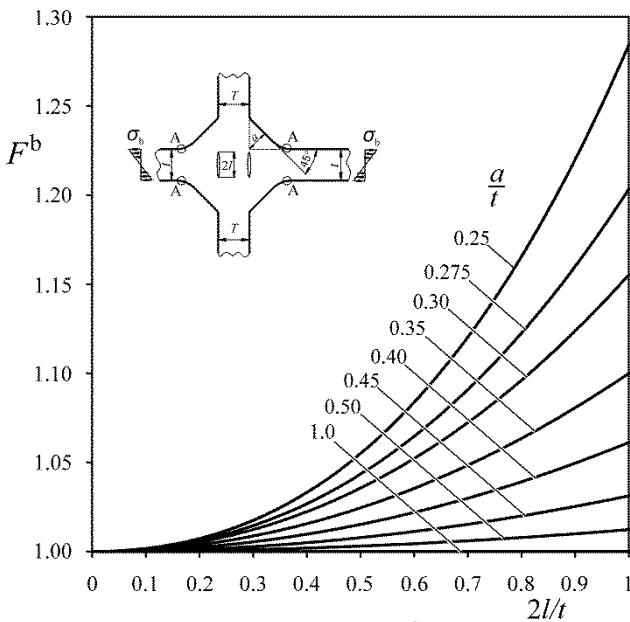


Fig. 6. Correction function F^b for calculating K_t^b at a weld toe of a load-carrying fillet welded cruciform joint with a lack of penetration defect and subjected to bending load

Table 4. Numerical values of the correction function $F_{K_I}^b$

	$2l/t$					
alt	0.10	0.25	0.50	0.75	0.90	1.0
0.25	0.026	0.066	0.133	0.198	0.238	0.264
0.333	0.022	0.054	0.106	0.153	0.177	0.193
0.4	0.018	0.045	0.088	0.125	0.144	0.155
0.6	0.011	0.026	0.051	0.072	0.083	0.089
0.8	0.006	0.016	0.031	0.045	0.052	0.056
1.0	0.004	0.010	0.021	0.030	0.034	0.037

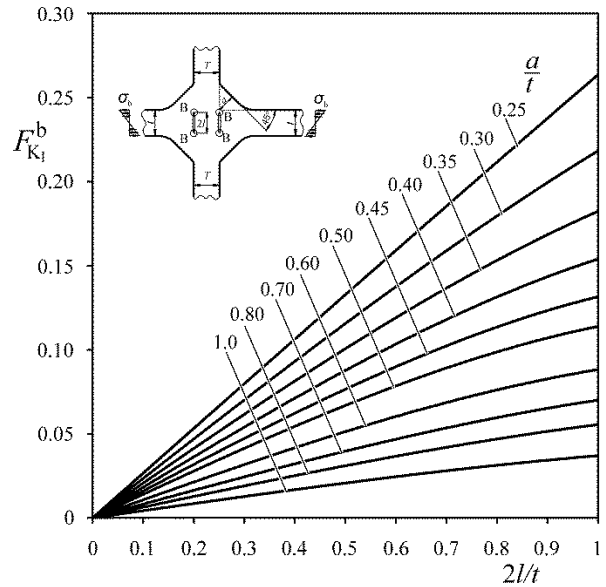


Fig. 7. Correction function $F_{K_I}^b$ for calculating $K_{K_I}^b$ at the apex of a lack of penetration defect in the load-carrying fillet welded cruciform joint subjected to bending load

Table 5. Numerical values of the correction function $F_{K_{II}}^b$

	$2l/t$					
alt	0.10	0.25	0.50	0.75	0.90	1.0
0.25	0.127	0.126	0.117	0.102	0.090	0.080
0.333	0.114	0.111	0.101	0.086	0.075	0.068
0.4	0.100	0.098	0.088	0.075	0.066	0.060
0.6	0.066	0.064	0.059	0.051	0.046	0.042
0.8	0.043	0.043	0.040	0.035	0.033	0.031
1.0	0.029	0.029	0.028	0.025	0.024	0.023

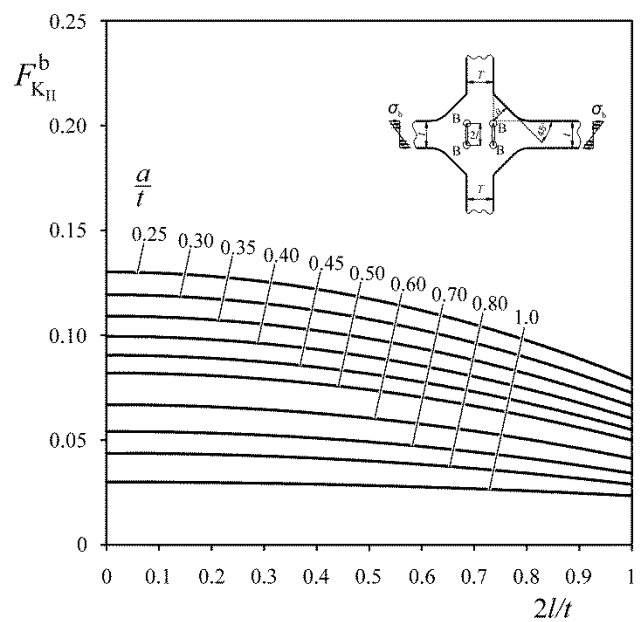


Fig. 8. Correction function $F_{K_{II}}^b$ for calculating $K_{K_{II}}^b$ at the apex of a lack of penetration defect in the load-carrying fillet welded cruciform joint subjected to bending load

The correction formula (4) proposed by Ushirokawa and Nakayama (1983), reported also in Iida and Uemura (1996), and represented in parameters regarded in the present work, also deals with the increase in SCF at the weld toe of a load-carrying fillet joint subjected to tensile load and should correspond to the present solution given by equation (A1).

$$F_{UN}^t = 1 + 0.64 \frac{(2l/t)^2}{2\sqrt{2}a/t} - 0.12 \frac{(2l/t)^4}{(2\sqrt{2}a/t)^2} \quad (4)$$

Comparison of both equations have shown significant differences in calculating correction values up to 33% in the range of $0.25 \leq a/t \leq 0.5$ and about $\pm 5\%$ in the range of $0.5 \leq a/t \leq 1$.

4. CONCLUSIONS

An extended analysis of numerical FEM solutions carried out using the ANSYS 19 MultiPhysics program for the load-carrying fillet welded cruciform joint with the lack of penetration defects has shown the significant influence of the geometrical parameters a , l and t of the weldment on the stress concentrations at two critical zones: at the weld toe and at the weld root. The first effect is represented by the correction functions of the stress concentration factor, whereas the second may be quantitatively described by the stress intensity factors K_I and K_{II} commonly used in fracture mechanics. The influence of the other parameters ρ and T has a minor effect.

Five correction functions have been derived, making it possible to calculate the corrected values of the stress concentration factors at the weld toe and particular values of K_I and K_{II} at the weld root for tensile and bending loads. For tensile load, K_{II} is 8–15 times smaller than K_I and may be omitted in the assessment of fatigue life. The accuracy of the formulas compared to the FEM results does not exceed 1.5%. The formulas presented in Appendix facilitate the computer-aided assessment of fatigue life of the structural element with such welded connections.

The correction formula of Ushirokawa and Nakayama (4) differs from the present solution given by equations (A1) of about $\pm 5\%$ in the range of $0.5 \leq a/t \leq 1$ and provides underestimated values up to -33% for the lower a/t ratios in the range of $0.25 \leq a/t \leq 0.5$.

Appendix: Formulas for calculating SCFs and stress intensity factors at the critical zones of a load-carrying fillet welded cruciform joint containing lack of penetration defects

Range of application: $0 < \rho/a \leq 0.5$; $0.25 \leq a/t \leq 1$; $0 \leq 2l/t \leq 1$ and $0.5 \leq T/t \leq 2$.

Tensile load, SCF at a weld toe:

$$K_t^t = K_{t0}^t F^t \quad (A1)$$

where

$$F^t = 1 + A_1(2l/t)^2 + A_2(2l/t)^3$$

$$A_1 = \text{Exp}(-5.25(a/t)^3 + 0.103)$$

$$A_2 = 4.028 - 24.433(a/t) + 51.482(a/t)^2 - 45.700(a/t)^3 + 14.655(a/t)^4$$

Tensile load, mode I stress intensity factor:

$$K_I^t = \sigma_t \sqrt{\pi l} F_{K_I}^t \quad (A2)$$

where

$$F_{K_I}^t = 1 + B_1 + B_2(2l/t)^2 + B_3(2l/t)^6$$

$$B_1 = -0.774(a/t) + 0.366(a/t)^2 - 0.103(a/t)^3$$

$$B_2 = 0.489 - 1.434(a/t) + 1.086(a/t)^2 - 0.204(a/t)^3$$

$$B_3 = 0.439 - 2.013(a/t) + 3.126(a/t)^2 - 1.523(a/t)^3$$

Bending load, SCF at a weld toe:

$$K_t^b = K_{t0}^b F^b \quad (A3)$$

where

$$F^b = 1 + C_1(2l/t)^2 + C_2(2l/t)^3$$

$$C_1 = \text{Exp}(-43.228(a/t)^4 - 1.693)$$

$$C_2 = \text{Exp}(-58.566(a/t)^2 + 1.613)$$

Bending load, mode I stress intensity factor:

$$K_I^b = \sigma_b \sqrt{\pi l} F_{K_I}^b \quad (A4)$$

where

$$F_{K_I}^b = D_1(2l/t) + D_2(2l/t)^3$$

$$D_1 = 0.470 - 0.999(a/t) + 0.786(a/t)^2 - 0.214(a/t)^3$$

$$D_2 = 0.233 - 1.713(a/t) + 3.939(a/t)^2 - 3.737(a/t)^3 + 1.272(a/t)^4$$

Bending load, mode II stress intensity factor:

$$K_{II}^b = \sigma_b \sqrt{\pi l} F_{K_{II}}^b \quad (A5)$$

where

$$F_{K_{II}}^b = E_1 + E_2(2l/t)^2$$

$$E_1 = 0.193 - 0.281(a/t) + 0.118(a/t)^2$$

$$E_2 = -0.074 + 0.100(a/t) - 0.033(a/t)^2$$

List of symbols:

a , nominal weld throat thickness; F^t , correction function of K_{t0}^t for partial penetration welds; F^b , correction function of K_{t0}^b for partial penetration welds; $F_{K_I}^t$, correction function of K_I for tensile load; $F_{K_I}^b$, correction function of K_I for bending load; $F_{K_{II}}^b$, correction function of K_{II} for bending load; FEM, finite element method; $2l$, total length of a crack or slit appearing as a consequence of unfused root faces; K_I^t , mode I stress intensity factor for cracks or unfused slits, tensile load; K_{II}^t , mode II stress intensity factor for cracks or unfused slits, tensile load; K_I^b , mode I stress intensity factor for cracks or unfused slits, bending load; K_{II}^b , mode II stress intensity factor for cracks or unfused slits, bending load; $K_t^t = \sigma_{t\max}/\sigma_t$, weld toe stress concentration factor for partial pene-

tration welds (tension); $K_t^b = \sigma_{1\max}/\sigma_b$, weld toe stress concentration factor for partial penetration welds (bending); $K_{t0}^t = \sigma_{1\max}/\sigma_t$, weld toe stress concentration factor for full penetration welds (tension); $K_{t0}^b = \sigma_{1\max}/\sigma_b$, weld toe stress concentration factor for full penetration welds (bending); r , radial distance measured from the crack tip; SCF, stress concentration factor; t , thickness of the main plate; T , thickness of the transversal plate; ρ , weld toe radius; σ_t , nominal tensile stress; σ_b , nominal bending stress; $\sigma_{1\max}$, maximum principal stress at a weld toe.

REFERENCES

1. **Chattopadhyay A, Glinka G, El-Zein M, Qian J, Formas R.** (2011), Stress analysis and fatigue of welded structures, *Weld World*, 55(7–8), 2–21.
2. **Chung HY., Liu SH., Lin RS., Ju SH.** (2008), Assessment of stress intensity factors for load-carrying fillet welded cruciform joints using a digital camera, *Int. Journal of Fatigue*, 30(10–11), 1861–1872.
3. **Dong P.** (2001), A structural stress definition and numerical implementation for fatigue analysis of welded joints, *Int. Journal of Fatigue*, 23(10), 865–876.
4. **European Committee for Standardization (CES)** (2005), *Eurocode 3: Design of steel structures - Part 1–9, Fatigue*, Brussels: CES; EN 1993-1-9:2005.
5. **Fayard JL., Bignonnet A. and Dang Van K.** (1996), Fatigue design criteria for welded structures, *Fatigue Fracture Eng. Materials & Structures*, 19(6), 723–729.
6. **Fricke W.** (2012), IIW Recommendations for the Fatigue Assessment of Welded Structures by Notch Stress Analysis: IIW-2006-09, *Woodhead Publishing Series in Welding and Other Joining Technologies*, 2–41.
7. **Fricke W.** (2013), IIW guideline for the assessment of weld root fatigue, *Weld World*, 57, 753.
8. **Hobbacher A.F.** (2009), The new IIW recommendations for fatigue assessment of welded joints and components – A comprehensive code recently updated, *International Journal of Fatigue*, 31, 50–58.
9. **Iida K., Uemura T.,** (1996), Stress concentration factor formulas widely used in Japan, *Fatigue Fract Eng Mater Struct.*, 19(6), 779–786.
10. **ISO 9692-1** (2013) *Welding and allied processes — Types of joint preparation — Part 1: Manual metal arc welding, gas-shielded metal arc welding, gas welding, TIG welding and beam welding of steels.*
11. **Kranz B., Sonsino C.M.** (2010), Verification of FAT Values for the Application of the Notch Stress Concept with the Reference Radii $R_{ref} = 1.00$ and 0.05 mm, *Weld World*, 54(7–8), 218–224.
12. **Livieri P., Lazzarin, P.** (2005), Fatigue strength of steel and aluminium welded joints based on generalised stress intensity factors and local strain energy values, *Int. Journal of Fracture*, 133(3), 247–276.
13. **Lotsberg I., Sigurdsson G.** (2006), Hot Spot Stress S-N Curve for Fatigue Analysis of Plated Structures, *J. Offshore Mech. Arct. Eng.*, 128(4), 330–336.
14. **Molski K.L., Tarasiuk P., Glinka G.** (2019), *Description of stress concentration at tee welded joints subjected to tensile and bending loads*, Opole University of Technology, Oficyna Wydawnicza, Studia i Monografie, 516, 61–80 (in Polish).
15. **Monahan C.C.** (1995), *Early fatigue cracks growth at welds*, Computational Mechanics Publications, Southampton.
16. **Niemi E., Fricke W. Maddox S. J.** (2018), *Structural Hot-Spot Stress Approach to Fatigue Analysis of Welded Components*, <https://doi.org/10.1007/978-981-10-5568-3>.
17. **Peterson R.E.** (1974), *Stress concentration design factors*, 2nd ed., Wiley, New York.
18. **Radaj D., Sonsino CM., Fricke W.** (2009), Recent developments in local concepts of fatigue assessment of welded joints, *International Journal of Fatigue*, 31(1), 2–11.
19. **Remes, H., Varsta, P.** (2010), Statistics of Weld Geometry for Laser-Hybrid Welded Joints and its Application within Notch Stress Approach, *Weld World*, 54(7–8), 189–207.
20. **Schijve J.** (2012), Fatigue predictions of welded joints and the effective notch stress concept, *International Journal of Fatigue*, 45, 31–38.
21. **Singh P.J., Achar D.R.G., Guha B., Nordberg H.** (2002), Influence of weld geometry and process on fatigue crack growth characteristics of AISI 304L cruciform joints containing lack of penetration defects, *Sci. Technol. Weld Join.*, 7(5), 306–312.
22. **Singh P.J., Guha B., Achar D.R.G.** (2003), Fatigue life prediction using two stage model for AISI 304L cruciform joints, with different fillet geometry, failing at toe, *Sci. Technol. Weld. Join.*, 8(1), 69–75.
23. **Sonsino C.M., Fricke W, de Bruyne F., Hoppe A., Ahmadi A., Zhang G.** (2012), Notch stress concepts for the fatigue assessment of welded joints – Background and applications, *Int. Journal of Fatigue*, 34(1), 2–16.
24. **Stenberg T., Barsoum Z., Balawi S.O.M.** (2015), Comparison of local stress based concepts — Effects of low-and high cycle fatigue and weld quality, *Engineering Failure Analysis*, 57, 323–333.
25. **Tchoffo Ngoula D., Beier H. Th., Vormwald M.** (2017), Fatigue crack growth in cruciform welded joints: Influence of residual stresses and of the weld toe geometry, *International Journal of Fatigue*, 101(2), 253–262.
26. **Tsuji I.** (1990), Estimation of stress concentration factor at weld toe of non-load carrying fillet welded joints, *Trans West Jpn Soc Naval Architects*, 80, 241–251.
27. **Ushirokawa O., Nakayama E.** (1983), Stress concentration factor at welded joints, *Ishikawajima–Harima Eng. Rev.*, 23(4), 351–355.
28. **Wooryong P., Chitoshi M.** (2008), Fatigue assessment of large-size welded joints based on the effective notch stress approach, *International Journal of Fatigue*, 30(9), 1556–1568.
29. **Young J.Y., Lawrence F.V.** (1985), Analytical and graphical aids for the fatigue design of weldments, *Fatigue Fracture Eng Mater Struct.*, 8(3), 223–241.
30. **Zerbst U., Madia M., Schork B.** (2016), Fracture mechanics based determination of the fatigue strength of weldments, *Procedia Structural Integrity*, 1, 10–17.

HEAT CONDUCTION IN ANISOTROPIC MEDIUM WITH PERFECTLY CONDUCTIVE THREAD-LIKE INCLUSIONS

Heorhiy SULYM*, Nataliia ILCHUK**, Iaroslav PASTERNAK**

*Bialystok University of Technology, Wiejska Str. 45C, 15-351 Bialystok, Poland

**Lutsk National Technical University, Lvivska Str. 75, 43018 Lutsk, Ukraine

h.sulym@pb.edu.pl, n.ilchuk@lntu.edu.ua, iaroslav.m.pasternak@gmail.com

received 21 May 2019, revised 8 January 2020, accepted 10 January 2020

Abstract: The paper presents a novel approach for the analysis of steady-state heat conduction of solids containing perfectly conductive thread-like inhomogeneities. Modelling of a thread-like heat conductive inhomogeneity is reduced to determination of density of heat distributed along a spatial curve, which replaces the inclusion. Corresponding boundary integral equations are obtained for anisotropic solids with thread-like inclusions. Non-integral terms are computed in a closed form. It is shown that, nevertheless the singularity of the equation is $1/r$, it is hypersingular, since the kernel is symmetric. Boundary element approach is adopted for solution of the obtained equations. Numerical example is presented for a rectilinear conductive thread, which verifies derived boundary integral equations.

Key words: thread-like inclusion, steady-state heat conduction, anisotropy, boundary integral equation, hypersingular

1. INTRODUCTION

Thermomechanical problems for inhomogeneities in structural materials have been widely studied in modern scientific literature, since they are closely related to the analysis of effective properties, strength and fracture of composite materials. Berger et al. (2005) presented an analytic fundamental solution for steady-state heat conduction in functionally graded anisotropic medium. Wang et al. (2005) developed a meshless method for the analysis of steady-state heat conduction in anisotropic and inhomogeneous solids. Vales et al. (2016) presented a homogenisation technique for the estimation of effective thermal properties of composite materials and used it for the analysis of experimental data from thermographic measurements. Khan et al. (2016) presented an analytic approach for determination of effective thermal properties of composites with highly conductive inclusions. Kushch et al. (2017) derived an analytic approach for determination of effective heat conduction properties of composite materials with ellipsoidal inclusions.

In general, thermomechanical problems for inhomogeneities can be divided into three main classes with respect to their geometric shape, which determine the approaches used in their analysis. These are: a) bulky inhomogeneities, in which the dimensions in different directions are comparable; b) thin inhomogeneities (ribbons, shells), in which one dimension is much less than two others and c) thread-like inhomogeneities (wires), in which one dimension is much greater than two others.

The class of bulky inhomogeneities includes globular defects of structural elements or globular filament of composite materials, which is rarely used at present. Such inclusions are mainly studied within the general approaches of thermomechanics. Analytic solutions for anisotropic solids with ellipsoidal inclusions are presented by Kushch et al. (2017). Chao et al. (2009) derived an exact solution for heat conduction in three-phase composite materials with elliptical inhomogeneities. Cepite and Jakovics (2008)

presented a finite element analysis of heat conduction in inhomogeneous medium with elliptical pores. Lee et al. (2018) obtained an analytic solution for effective thermal properties for a medium containing spherical inclusions with imperfect interface.

Thin ribbon-like, plate-like and wire-like filaments are widely used in modern composite materials, including nano-composites. It should be mentioned that modern carbon nano-filament, for example, graphene, possesses very high thermal conductivity (Balandin et al., 2010), which should be definitely accounted for in the numerical thermomechanical analysis of carbon nano-composites. However, the study of thin-walled and thread-like inclusions is complicated due to the low accuracy of general numerical approaches (e.g. finite element and boundary element methods) in modelling of thin shapes. Therefore, thin and thread-like inclusions are studied with special approaches (e.g. see Sulim and Piskozub, 2008), which can reduce the number of degrees of freedom accounting for the 2D or 1D geometries of such inhomogeneities.

Thin ribbon-like and shell-like inclusions can be studied with the help of discontinuity (jump) function method, which replaces the inhomogeneity with a surface of field discontinuity (see Pasternak et al., 2019). However, this approach cannot be directly applied to the study of thread-like inclusions. To the best of authors' knowledge, there are no publications which provide some special approaches for thermomechanical analysis of thread-like inhomogeneities. There are only some publications which provide analytic and experimental study of nano-wires based on the approaches of theoretical physics (Anufriev and Nomura, 2019; Im et al., 2013).

Therefore, this study provides a straightforward boundary integral equation approach and the boundary element numerical solution strategy for the analysis of steady-state heat conduction in anisotropic medium containing a perfectly conductive thread-like inclusion. It is the first step in the thermomechanical analysis of materials containing thread-like inhomogeneities.

2. BOUNDARY INTEGRAL EQUATIONS OF HEAT CONDUCTION OF ANISOTROPIC MEDIUM CONTAINING A THREAD-LIKE INCLUSION

Consider an anisotropic medium containing a perfectly conductive thread-like inclusion of constant radius ρ , in which the median line L is a smooth curve (see Fig. 1).

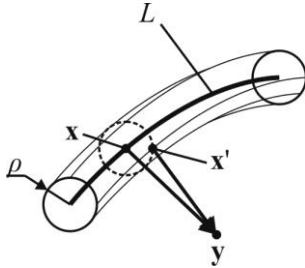


Fig. 1. Thread-like inclusion

Green's third identity for anisotropic heat conduction in a solid with such inclusion is written as (Pasternak et al., 2017)

$$\theta(\mathbf{y}) = \iint_S (\Theta(\mathbf{x}', \mathbf{y})h_n(\mathbf{x}') - H(\mathbf{x}', \mathbf{y})\theta(\mathbf{x}'))dS(\mathbf{x}') + \theta^\infty(\mathbf{y}), \tag{1}$$

where θ is temperature, h_n is a heat flux normal to the surface S of the inclusion and $\theta^\infty(\mathbf{y})$ is a temperature field due to thermal loading at infinity. Kernels of integral Eq. (1) are defined as (Pasternak et al., 2017)

$$\Theta(\mathbf{x}, \mathbf{y}) = -\frac{1}{8\pi^2|\mathbf{x}-\mathbf{y}|} \oint_{|\lambda|=1} (k_{ij}\lambda_i\lambda_j)^{-1} d\lambda, \tag{2}$$

$$H(\mathbf{x}, \mathbf{y}) = -k_{ij}n_i(\mathbf{x})\Theta_{,j}(\mathbf{x}, \mathbf{y}), \tag{3}$$

where k_{ij} are heat conduction coefficients, $n_i(\mathbf{x})$ is a unit normal to the inclusion surface at the point \mathbf{x} and λ is a unit vector normal to the position vector $\mathbf{x} - \mathbf{y}$.

When ρ is small compared to a characteristic length L of the thread, one can assume that according to Eq. (2)

$$\Theta(\mathbf{x}', \mathbf{y}) \approx \Theta(\mathbf{x}, \mathbf{y}) \tag{4}$$

and according to Eq. (3)

$$\int_0^{2\pi} H(\mathbf{x}', \mathbf{y})d\vartheta(\mathbf{x}') = 0, \tag{5}$$

where ϑ is the polar angle in the normal cross-section of the inclusion at the point \mathbf{x} .

Since the inclusion is assumed perfectly heat conducting, its temperature $\theta(\mathbf{x})$ is a constant, and thus, for small ρ accounting for Eqs (4) and (5), one can rewrite Eq. (1) as

$$\theta(\mathbf{y}) = \int_L \Theta(\mathbf{x}, \mathbf{y})\gamma(\mathbf{x})dL(\mathbf{x}) + \theta^\infty(\mathbf{y}), \tag{6}$$

where

$$\gamma(\mathbf{x}) = \rho \int_0^{2\pi} h_n(\mathbf{x}')d\vartheta(\mathbf{x}') \tag{7}$$

is the sought heat distributed along the inclusion line.

The unknown function $\gamma(\mathbf{x})$ can be determined by solving the integral equation obtained from Eq. (6) by approaching an internal

point \mathbf{y} of a medium to some point \mathbf{x}_0 of the thread-like inclusion:

$$\theta^0 = \lim_{\mathbf{y} \rightarrow \mathbf{x}_0} \int_L \Theta(\mathbf{x}, \mathbf{y})\gamma(\mathbf{x})dL(\mathbf{x}) + \theta^\infty(\mathbf{x}_0), \tag{8}$$

where θ^0 is the constant temperature of the inclusion, since it is assumed perfectly conductive.

Eq. (8) should be accompanied with the inclusion balance equation

$$\int_L \gamma(\mathbf{x})dL(\mathbf{x}) + H_0 = 0, \tag{9}$$

where H_0 is the external heat applied to the inclusion.

It should be noted that, nevertheless the kernel $\Theta(\mathbf{x}, \mathbf{y})$ has singularity $1/r$, the integral Eq. (8) is hypersingular and cannot be considered as a Cauchy type, since the kernel is symmetric, that is, $\Theta(\mathbf{x}, \mathbf{y}) = \Theta(\mathbf{y}, \mathbf{x})$. Therefore, consider this equation in detail.

Assume that the line L , which models a thread, is a smooth spatial curve. Introducing an opened contour L_ϵ of small radius $\epsilon \rightarrow +0$ surrounding the collocation point \mathbf{x}_0 (see Fig. 2), Eq. (8) is rewritten as

$$\int_{L \setminus L_\epsilon} \Theta(\mathbf{x}, \mathbf{x}_0)\gamma(\mathbf{x})dL(\mathbf{x}) + B(\mathbf{x}_0)\gamma(\mathbf{x}_0) = \theta^0 - \theta^\infty(\mathbf{x}_0), \tag{10}$$

where

$$B(\mathbf{x}_0) = \int_{L_\epsilon} \Theta(\mathbf{x}, \mathbf{x}_0)dL(\mathbf{x}). \tag{11}$$

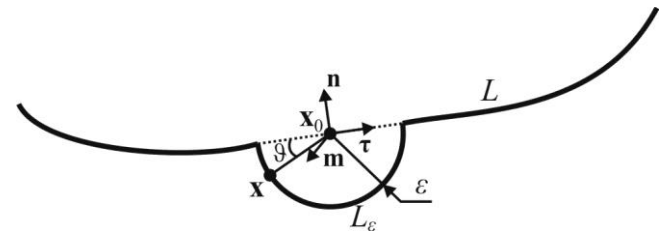


Fig. 2. Determination of the non-integral terms

Substituting Eq. (2) into Eq. (11), one obtains

$$B(\mathbf{x}_0) = -\frac{1}{8\pi^2} \int_0^\pi \oint_{|\lambda|=1} (k_{ij}\lambda_i\lambda_j)^{-1} d\lambda d\vartheta, \tag{12}$$

where $\lambda(\psi) \perp -(\cos\vartheta\tau + \sin\vartheta\mathbf{n})$. Since according to Eq. (2) the integrand of Eq. (12) is a π -periodic function of ϑ and ψ , the non-integral term $B(\mathbf{x}_0)$ depends only on the tangent vector τ to the line L at the point \mathbf{x}_0 .

For isotropic materials, Eq. (12) reduces to

$$B(\mathbf{x}_0) = -\frac{1}{4k} \tag{13}$$

and is independent of the spatial orientation of the inclusion line. Here, k is a heat conduction coefficient of an isotropic material.

It should be emphasised that, nevertheless the strength of singularity in Eq. (10) according to Eq. (2) is $1/r$, the integral in Eq. (10) cannot be computed as the Cauchy principal value. Cauchy principal value can be computed for an integral of a type

$$\text{CPV} \int_a^b \frac{f(x)}{x-x_0} dx = \int_a^{x_0-\epsilon} \frac{f(x)}{x-x_0} dx + \int_{x_0+\epsilon}^b \frac{f(x)}{x-x_0} dx \quad (a < x_0 < b), \tag{14}$$

but Eq. (10) contains integral of the type

$$\int_a^{x_0-\varepsilon} \frac{f(x)}{|x-x_0|} dx + \int_{x_0+\varepsilon}^b \frac{f(x)}{|x-x_0|} dx \quad (a < x_0 < b), \quad (15)$$

which diverges when ε tends to zero. Therefore, boundary integral equation (11) is *hypersingular*, and for its solution, the integral in it should be computed as the Hadamard Finite Part.

3. COMPARISON WITH THE 2D SOLUTION FOR A HEAT CONDUCTIVE LINE INCLUSION

The studies on 2D heat conductive line inclusions are widely covered in scientific literature (e.g. see Sulim and Piskozub, 2008). However, in 2D heat conduction, line inhomogeneity is not exactly a line in 3D representation. Since a cylindrical (plane heat conduction and plane strain) or a plate-like (generalised heat conduction in a plate with thermally insulated surfaces, plane stress) solid is considered in 2D heat conduction and thermoelasticity, for which the geometry and loading do not change along the generatrix (generally Ox_3 axis), a 2D rigid line is, in general, a cylindrical surface, for which intersection (a 2D line) with a front plane is considered.

Boundary integral equations for a 2D heat conducting line are obtained as (e.g. see Sulim and Piskozub, 2008)

$$\int_L \Theta^{2D}(\mathbf{x}, \mathbf{x}_0) \Sigma h_n(\mathbf{x}) dL(\mathbf{x}) = \theta^0 - \theta^\infty(\mathbf{x}_0), \quad (16)$$

accompanied with the heat balance equation

$$\int_L \Sigma h_n(\mathbf{x}) dL(\mathbf{x}) + H_0 = 0, \quad (17)$$

where $\Sigma h_n(\mathbf{x})$ is the heat flux discontinuity at transition through the 2D inclusion line.

The 2D kernel $\Theta^{2D}(\mathbf{x}, \mathbf{x}_0)$ of the integral Eq. (16) possesses logarithmic singularity.

Comparing the boundary integral equations (9) and (10) for a heat conducting thread-like inclusion and Eqs (16) and (17) for a 2D heat conductive line, one can observe the following.

- **Order of singularity.** According to Eq. (16), boundary integral equations for 2D heat conductive line inclusions are weakly singular (with logarithmic singularity). After differentiation of Eq. (16) with respect to \mathbf{x}_0 , one can obtain a singular integral equation with Cauchy principal value integral, which is well studied. In contrast, boundary integral equation (10) for a 3D heat conductive thread is hypersingular with symmetric kernel of the order $1/r$. The authors have found only one source (Eq. (54) on p. 316 of Polyanin and Manzhirov (2008)), referring the integral equation with a similar kernel.
- **Type of equation.** It is readily seen that the integral Eq. (10) of a heat conductive thread-like inclusion is a Fredholm equation of the second kind and the integral Eq. (16) of the 2D heat conducting line inclusion is a Fredholm equation of the first kind. Both equations are inhomogeneous.
- **Heat flux singularity at inclusion tip.** It is well known that the heat flux exhibits the square root singularity at the two tips of the 2D heat conducting line inclusion (Sulim and Piskozub, 2008). The same concerns the sought solution $\Sigma h_n(\mathbf{x})$ of Eq. (16). Heat flux discontinuity $\Sigma h_n(\mathbf{x})$ at 2D inclusion line possesses square root singularity at its endpoints. The same concerns the stress field at the 2D inclusion in thermoelastic problems. Nevertheless, the studies by Mirenkova and Sosnina

(1982) revealed that the stress field near the tips of a rigid needle inclusion possesses another type of singularity. The stresses at the tip of an ellipsoidal needle are of order $O(1/(\alpha^2 |\ln \alpha|))$, where $\alpha \ll 1$ defines the curvature of the inclusion at its tips. According to the theory of asymptotic expansions, the same singularity is observed in the stress field in the vicinity of inclusion tips. Also, the same field behaviour is observed in the analysis of flows near thin axisymmetric cavities (see Petrov, 1986).

This comparison reveals that thread-like inclusions should be attributed to a separate class of inhomogeneities, which stands alone from bulky inclusions and shell-like (or 2D line) inclusions. Special mathematical attention should be paid to the development of analytic and numerical approaches of the solution of boundary integral equation (10), which discover and account for the singularity of the sought function at the endpoints of inclusion line.

4. RECTILINEAR THREAD-LIKE INCLUSION IN ISOTROPIC MEDIUM

Consider a rectilinear thread-like, heat conductive inclusion of length $2a$ in an isotropic medium, which is placed at the section $-a < x_1 < a$ of Ox_1 axis. The heat h^0 is flowing uniformly along Ox_1 axis. In this case, Eqs (9), (10) and (13) reduce to

$$\frac{1}{\pi} \text{HFP} \int_{-a}^a \frac{\gamma(x_1)}{|x_1 - x_1^{(0)}|} dx_1 + \gamma(x_1^{(0)}) = -4h^0 x_1^{(0)}. \quad (18)$$

Here, HFP stands for the Hadamard Finite Part of the integral.

Boundary integral equation (18) can be solved numerically with the following boundary element approach. The interval $(-a, a)$ is divided into N equal parts (boundary elements). It is assumed that the function $\gamma(x_1)$ is constant on each element ($\gamma^{(j)}$). Collocation points $x_1^{(i)} = a(-1 + (2j - 1)/N)$ are placed at the centre of each boundary element. Thus, the integral equation (18) is reduced to the following system of linear algebraic equations:

$$\frac{1}{\pi} \sum_{j=1}^N a_{ij} \gamma^{(j)} = -4h^0 x_1^{(i)}, \quad (19)$$

where

$$a_{ij} = \begin{cases} \pi, & i = j \\ \log \left| \frac{t_{ij}+1}{t_{ij}-1} \right|, & i \neq j, \end{cases} \quad (20)$$

and $t_{ij} = (x_1^{(i)} - x_1^{(j)})/(N/a)$. Here, $i = 1, \dots, N$ and $j = 1, \dots, N$.

One thousand constant boundary elements of equal length are used to mesh the line of the thread-like inclusion. Numerical results for the sought function $\gamma(x_1)$ are presented in Fig. 3.

Normalised temperature field $\theta k/(h^0 a)$ near the thread-like inclusion is presented in Fig. 4 (here, k is the heat conduction coefficient). The field is calculated based on Eq. (2).

One can see in Fig. 4 that the temperature is zero on the inclusion line. Isothermal lines “envelop” the inclusion. Field distribution is very close to the thread. Large field gradient is observed at inclusion tips.

Obtained temperature field was compared with the results of finite element analysis. Perfect agreement was observed, which verifies the proposed approach.

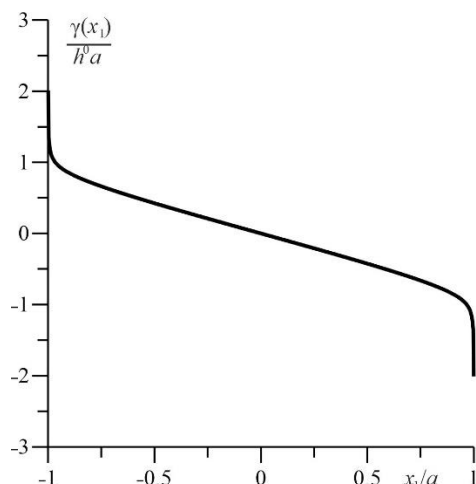


Fig. 3. Distribution of sought heat along the inclusion line

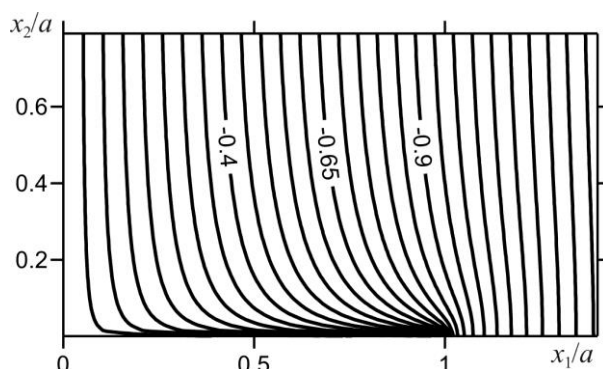


Fig. 4. Dimensionless temperature field near the thread-like inclusion

5. CONCLUSION

The study presents a novel approach to the analysis of thread-like inclusions. Boundary integral equations of the problem are obtained and it is shown that, nevertheless the kernel possesses $1/r$ singularity, this equation is hypersingular.

Numerical solution is presented for a rectilinear thread-like conductive inclusion. Big field gradients are observed near the inclusion line, especially at its tips. Therefore, special studies should be provided on the analysis of singularity of the solution of the obtained hypersingular boundary integral equations.

REFERENCES

1. Anufriev R., Nomura M. (2019), Coherent thermal conduction in silicon nanowires with periodic wings, *Nanomaterials*, 9, 142; doi:10.3390/nano9020142.
2. Balandin A.A., Ghosh S., Nika D.L., Pokatilov E.P. (2010), Extraordinary thermal conductivity of graphene: possible applications in thermal management, *ECS Trans.*, 28(5), 63–71.

3. Berger J.R., Martin P.A., Mantić V., Gray L.J. (2005), Fundamental solutions for steady-state heat transfer in an exponentially graded anisotropic material, *Z. angew. Math. Phys.*, 56, 293–303.
4. Cepite D., Jakovics A. (2008), Modelling of a heat transfer through the material with regular distributed elliptic cavities, *HEAT & POWER AND THERMAL PHYSICS*, 1, 56–66.
5. Chao C.K., Chen C.K., Chen F.M. (2009), Analytical exact solutions of heat conduction problems for a three-phase elliptical composite, *CMES*, 47(3), 283–297.
6. Im H., Hwang Y., Moon J.H., Lee S.H., Kim J. (2013), The thermal conductivity of Al(OH)₃ covered MWCNT/epoxy terminated dimethyl polysiloxane composite based on analytical Al(OH)₃ covered MWCNT, *Composites Part A: Applied Science and Manufacturing*, 54, 159–165.
7. Khan K.A., Khan S.Z., Khan M.A. (2016), Effective thermal conductivity of two-phase composites containing highly conductive inclusions, *Journal of Reinforced Plastics and Composites*, 35, 1586–1599.
8. Kushch V.I., Sevostianov I., Giraud A. (2017), Local fields and effective conductivity tensor of ellipsoidal particle composite with anisotropic constituents, *Proceedings of the Royal Society A: Mathematical, Physical and Engineering Sciences*, 473(20170472), 1–19 (<http://dx.doi.org/10.1098/rspa.2017.0472>).
9. Lee S., Lee J., Ryu B., Ryu S. (2018), A micromechanics-based analytical solution for the effective thermal conductivity of composites with orthotropic matrices and interfacial thermal resistance, *SCIENTIFIC REPORTS*, 8, Article Number: 7266, DOI: 10.1038/s41598-018-25379-8.
10. Mirenkova G.N., Sosnina E.G. (1982), Rigid ellipsoidal disc and needle in an anisotropic elastic medium, *PMM U.S.S.R.*, 45, 122–126.
11. Pasternak Ia., Pasternak R., Pasternak V., Sulym H. (2017), Boundary element analysis of 3D cracks in anisotropic thermomagnetoelastoelectric solids, *Engineering Analysis with Boundary Elements*, 74, 70–78.
12. Pasternak Ia., Sulym H., Ilchuk N. (2019), Boundary element analysis of 3D shell-like rigid electrically conducting inclusions in anisotropic thermomagnetoelastoelectric solids, *Z Angew Math Mech.* e201800319 (<https://doi.org/10.1002/zamm.201800319>)
13. Petrov A.G. (1986), Asymptotic expansions of thin axisymmetric cavities, *Journal of Applied Mechanics and Technical Physics*, 27(5), 667–672.
14. Polyanin A.D., Manzhirov A.V. (2008) *Handbook of integral equations*, 2nd ed., Chapman & Hall/CRC.
15. Sulim G.T., Piskozub J.Z. (2008), Thermoelastic equilibrium of piecewise homogeneous solids with thin inclusions, *J Eng Math*, 61, 315–337.
16. Vales B., Cuartas V.M., Welemene H., Pastor M.-L., Trajin B. (2016), Heat source estimation in anisotropic materials, *Composite Structures*, 136, 287–296.
17. Wang H., Qin Q.-H., Kang Y.L. (2005), A new meshless method for steady-state heat conduction problems in anisotropic and inhomogeneous media, *Archive of Applied Mechanics*, 74, 563–579.

The present paper is financially supported by the Ministry of Science and Higher Education of Poland (research project No S/WMM/4/2017) and realised in Białystok University of Technology.

SHAPING THE PARAMETERS OF CYLINDRICAL BELT SURFACE IN THE JOINT AREA

Krzysztof WAŁĘSA,* Ireneusz MALUJDA,* Dominik WILCZYŃSKI*

*Institute of Machine Design, Poznań University of Technology, ul. Piotrowo 3, 61-138 Poznań, Poland

krzysztof.walesa@put.poznan.pl, ireneusz.malujda@put.poznan.pl, dominik.wilczynski@put.poznan.pl

received 24 October 2019, revised 13 January 2020, accepted 15 January 2020

Abstract: Most of the industrial machines use round-shaped drive belts for power transfer. They are often a few millimetres in diameter, and made of thermoplastic elastomer, especially polyurethane. Their production process requires the bonding step, which is often performed by butt welding, using the hot plate method. The authors have undertaken to design an automatic welding machine for this purpose. Consequently, it is required to carry out a process analysis of hot plate welding, which entails describing the dependency between technological parameters (temperature, pressure force, time) and the quality of the joint, especially the outer surface of the belt around the weld. To analyse this process in a proper way, it is necessary to describe the physical phenomena that occur in the material, during particular operations of the hot plate welding process. One of the most troublesome phenomena occurring during the welding process is removing of the flash. These round rings, placed around the weld, which remains after the joining process, are unacceptable in the finished component. The authors took an effort to design the necessary equipment for removing of the flash after welding, using some simple parts that cut off excessive material. The paper shows the three possible solutions for flash removal. They were verified experimentally, and afterwards, the best solution was chosen. Additionally, a number of analytical calculations were carried out in order to determine the maximum force value required for this operation. Results of the analytical calculations were compared with experimental results.

Key words: Hot plate welding, flash, flash removing, surface processing, cutting, round drive belts

1. INTRODUCTION

Industrial grade belts, both used in drives and conveyors, are commonly utilized in machine building for transferring torque between the connected workstations or for transporting products on manufacturing lines. Both full cross-section and perforated conveyor belts are utilized in transportation; the latter are utilized in vacuum transportation of light objects (Wojtkowiak et al., 2018; Wojtkowiak and Talaśka, 2019). On the other hand, the most commonly used types of drive belts are flat, toothed and shaped belts. Toothed belts are used both in simple transmissions as well as non-classical solutions, for example, with variable ratios (Domek and Dudziak, 2011; Domek et al., 2016; Krawiec et al., 2018; Krawiec et al., 2019). Shaped belts, in particular V-shaped and round belts are commonly employed in drives, that is, special robotic arm joint mechanism, with two twisted small diameter belts (Inoue et al., 2016), they can be made of rubber (Kukla et al., 2015 and 2019) or polyester or polyurethane based elastomers (Behabelt, 2015). Their common application in industrial machines calls for an efficient manufacturing process, which usually takes place in two stages (Sikora, 1993). First of all, a long belt is manufactured and cut down to the required size. Finally, the ends are joined permanently to form a continuous loop (Wałęsa, 2018).

Due to the peculiar characteristics of the thermoplastic elastomers used in the manufacturing of such belts, it is possible to join them by hot welding. A specific approach to this process is butt-welding utilizing the hot plate method; it is popular due to its simplicity and efficiency (Grewell and Benatar, 2007; Yousepour et al., 2004). This method is commonly employed in the automotive industry and civil engineering, for example, in the process of

joining: tanks for utility fluids, lamp enclosures, engine instrumentation (Pietrzak et al., 2019; Grewell and Benatar, 2007) and pipes (Rzasinski, 2017; Troughton, 1997; Cocard et al., 2009). Furthermore, studies were carried out on the hot welding of inflexible polymer materials, for example, acrylonitrile butadiene styrene copolymer (ABS) (Mokhtarzadeh and Benatar, 2012), polycarbon (PC) (Krishnan and Benatar, 2004), as well as polypropylene (PP) (Nieh and Lee, 1992). However, it needs to be pointed out that all of them apply primarily to plastics.

The authors started design works on a device for automated butt welding of drive belts utilizing the hot plate technique (Wałęsa et al., 2018), which is to improve the efficiency of the manufacturing process of continuous belts. For the purpose of verification of the design assumptions, the process was to be analysed together with further study of the influence of heating parameters on weld quality (Wałęsa et al., 2019a and 2019b). It was assumed that the drive belt made of TPU C85A polyurethane, commonly marketed by drive belt manufacturers (BASF, 2010) will be hot welded. A review of the available subject literature has concluded that information on this method of connecting thermoplastic elastomers is difficult to obtain.

The butt welding process utilizing the hot plate method can be divided into 5 stages (Wałęsa et al., 2019; Klimpel, 1999 and 2000; Potente et al.; 2002, Jasiulek, 2006). One of the most important activities is the plasticization of the belt end, which enables the chemical reaction and physical interaction between the macromolecules in the joining process (Amanat et al., 2010; Amancio-Filho and dos Santos, 2009; Madej and Ozimina, 2010; Puszcza, 2006; Żuchowska, 2000). The welding temperature choice is a very important issue. Exceeding some values causes

destruction of the material volume in a few stages (Wanqing et al., 2017). On the other hand, in case of some polymers, joint strength increases with welding temperature (Evers et al., 2017). When the heating and cooling process is considered, also it should be noted some division in the three zones with different impact of temperature. This phenomenon can be observed in all of the semi-crystalline thermoplastic polymers, so in butt welding of round belts, it has some impact to the process (Casalino and Ghorbel, 2008). The plasticization of the belt material due to temperature and compression forces activities, results in a flash forming in the final stage of the process (Fig. 1).

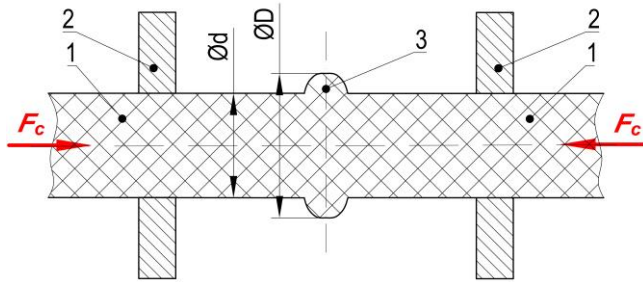


Fig. 1. Forming of the flash in the final stage of the drive belt hot welding: 1 – belt end, 2 – grips, 3 – flash; F_c – pressure force during the final stage of the hot welding, d – belt diameter, D – external flash diameter

The flash constitutes excessive material in the form of a ring with diameter D around the weld, caused by the pressing of the plasticized belt end towards the hot plate with force F_c .

The removal of flash is a significant problem in the aspect of automating the manufacturing process of these belts, as the belt forms a continuous circuit as a result of this welding. Therefore, this operation is often performed manually, using simple tools such as shears. Striving to optimize the entire manufacturing process of the belts, a method to remove the post-weld flash was devised, which entails automatic shearing with use of profiled cutting sleeves; furthermore, the necessary instrumentation was also designed. In order to select the correct components of the drive system, it is necessary to estimate the process forces during this technical operation.

Subject literature provides formulas for calculating the necessary force for cutting various materials using dies for, for example, sheet metal, leather and plastics (Groover, 2017; Marciniak, 1959) as well as composite belts (Wilczyński et al., 2019; Wojtkowiak et al., 2018). However, these approaches fail to account for the peculiar construction features of dies used when the belt is continuous. For this reason, the developed construction solution must be analysed and subject to empirical examination in order to verify its correct operation.

Study of the technological process of hot welding and drive belt processing after the weld was made are problematic as the joined material exhibits non-classical thermomechanical characteristics (Broniewicz et al., 1970). This is shared by other materials, for example, crystallized carbon dioxide (Górecki et al. 2019), fragmented natural materials (Talaśka, 2018), organic fibres (Talaśka and Ferreira, 2017) or glues (Fierek et al., 2019), and predicting their behaviour under mechanical and thermal load conditions is problematic. One needs to consider that the influence of temperature on the characteristics of such polymers is significant (Ciszewski and Radomski, 1989; Sikora, 1993). With

this fact in mind, experimental study to determine the behaviour of belt material during the removal of the flash is called for.

In order to determine the force value necessary to carry out this operation, analytic calculations and experimental studies were performed on the process of cutting off the flash. As a consequence, the characteristics of the process of flash removal utilizing this method were determined, with particular emphasis on the maximum force value utilized in the shearing process. Cutting tests were carried out for three cases of designed instrumentation assemblies, together with analytical calculations, which lead to obtaining maximum cutting force, for one of them.

2. STUDY METHODOLOGY

The study utilized conical blades of the author's own design with different apex angle values: 10°, 20°, 30° and 40°, manufactured with steel hardened to 58 HRC (Fig. 2).

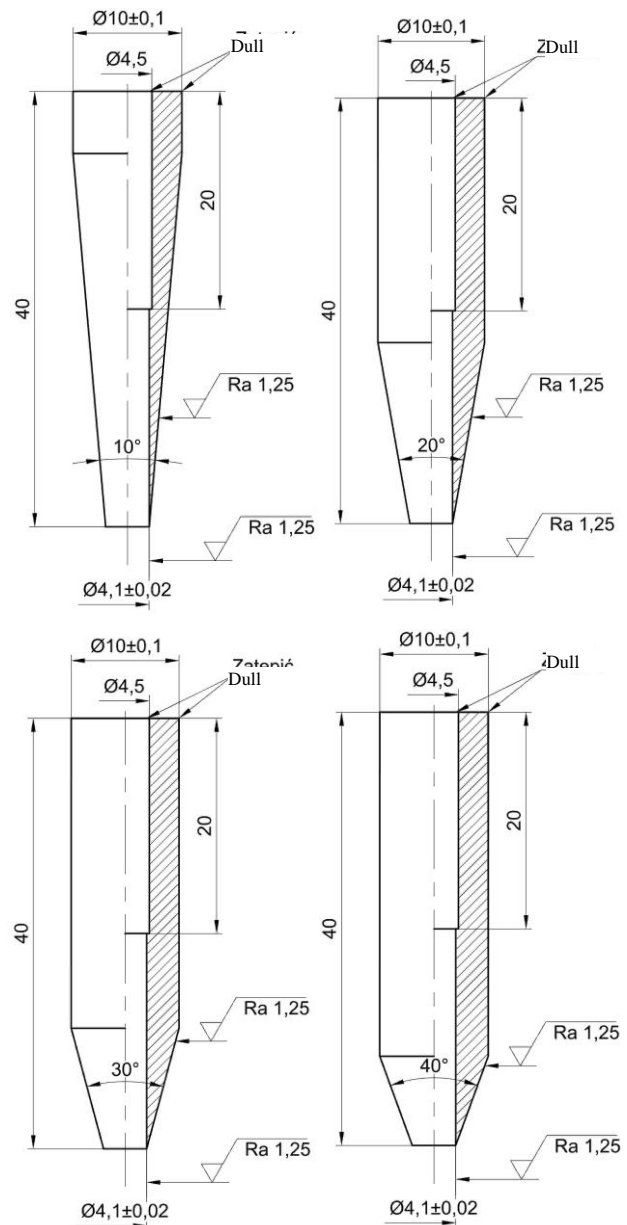


Fig. 2. Executive drawings for the blades used in the study with apex angle values: 10°, 20°, 30° and 40°

For the assumed fixed blade geometry, three methods of flash removal were assumed, which are possible in the proposed construction solution:

- two-sided cutting of the flash with cutting force F_T vectors in opposite directions, distributed evenly at the belt circumference, acting in contact with the round external surface of the belt. This method is achieved by compressing the flash between two identical blades (Fig. 3), whereas both blades are movable in relation to one another,

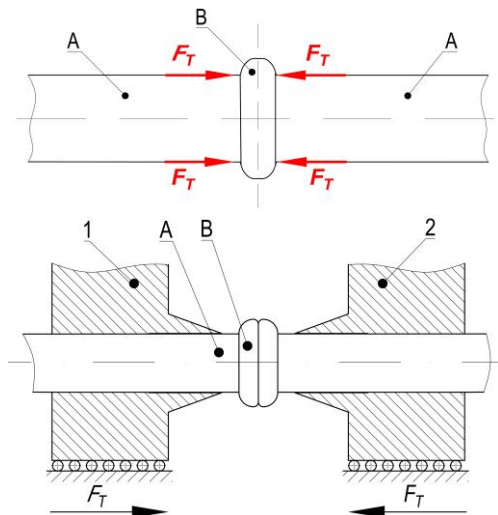


Fig. 3. Two-sided cutting of the flash with cutting forces in opposite directions, together with an implementation example: A – belt ends, B – flash, 1 and 2 – cutting sleeves; F_T – forces cutting off the flash

- one-sided cutting of the flash using F_T cutting forces distributed evenly along the circumference of the belt, acting in contact to the round external surface of the belt, with additional force F_c acting along the belt axis with opposite sense (Fig. 4). This method is carried out by drawing the belt with flash towards the blade,

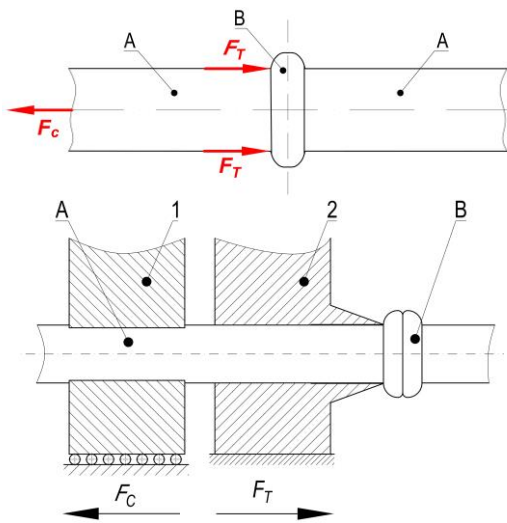


Fig. 4. One-sided cutting of the flash with force drawing the belt in the opposite direction: A – belt end, B – flash; F_T – forces cutting off the flash, F_c – force drawing the belt through the sleeve, 1 – drawing sleeve, 2 – cutting sleeve

- one-sided flash cutting using forces F_T , distributed evenly at the belts circumference, acting in contact to the round external surface of the belt, with additional plate supporting the flash (Fig. 5). Its use causes a reaction force F_p , which prevents the movement of the flash and increases the effectiveness of the removal process. The implementation entails pressing the flash by the blade towards the support plate made of PA6 aluminium, with bore diameter allowing to freely move out the belt.

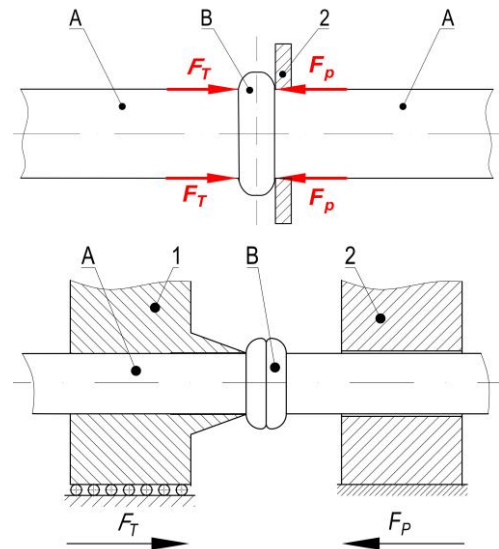


Fig. 5. One-sided cutting of the flash with support: A – belt end, B – flash, 1 – cutting sleeve, 2 – support plate; F_T – forces cutting off the flash, F_p – reaction force of the support plate

The tests were carried out for 4 different rake angles, for welded belt sections with average diameter $d_c = 4,11$ mm. Cutting tests were performed on sixteen samples for each blade angle. The testing utilized the MTS Insight 50 kN durometer with standard grips, flat supporting board with openings together with a supporting plate (Fig. 6). The samples were hot welded belt sections of random length (Fig. 7).

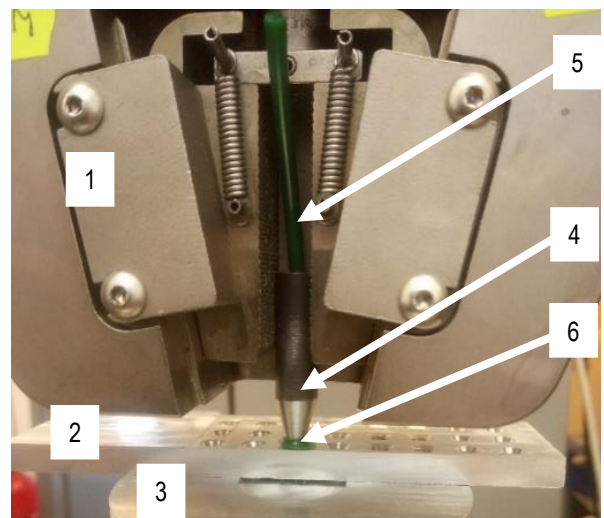


Fig. 6. The testing station during the examination of the flash removal process utilizing the third method: 1 – durometer grip, 2 – supporting plate with holes, 3 – supporting plate, 4 – cutting sleeve, 5 – belt, 6 – flash



Fig. 7. Belt samples with flashes, prepared for the study

Additionally, for the third method of removal, analytical calculations were carried out to determine the force value necessary to remove the flash, utilizing the balance of forces between the belt and the blade. Based on the dimensions of the blade and the belt (Fig. 8) as well as the distribution of forces between them (Fig. 9), it is possible to derive a general formula to calculate the force value required to remove the flash using this technique.

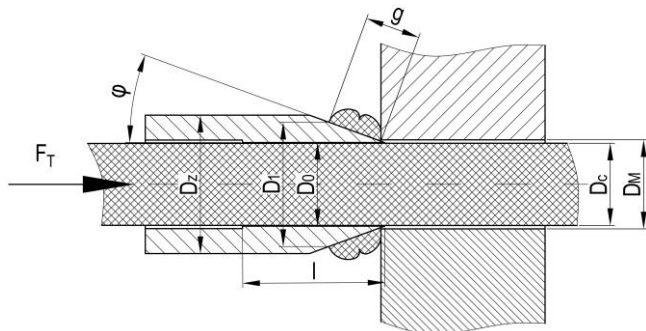


Fig. 8. Dimensions assumed for the analytical calculations: φ – blade inclination angle, D_z – internal diameter of the cutting sleeve, D_0 – bore diameter of the cutting sleeve, D_c – external belt diameter, D_M – support bore diameter, g – flash thickness, F_T – force necessary to remove the flash, l – length of contact area between the belt and the blade

The process force required to remove the flash F_T can be expressed with the formula below:

$$F_T = F_{Tr} + F_{T1} + F_{T2}, \quad (1)$$

where: F_T – flash removal process force, F_{Tr} – component of cutting force from flash stretching on the conical surface of the blade, F_{T1} – cutting force component from flash friction on the conical surface of the blade, F_{T2} – force component from belt friction inside the blade bore.

Considering F_{Tr} , according to the force distribution (Fig. 9), may be expressed as follows:

$$F_{Tr} = F_r \cdot \sin\varphi = p_1 \cdot A_s, \quad (2)$$

where: F_r – singular force stretching the flash, φ – blade side

inclination angle, p_1 – flash bearing pressure on the blade surface, A_s – conical surface constituting the blade side on which the deformed flash is present. It should be therefore noticed that the flash surface in contact with the conical blade side can be calculated from the following formula:

$$A_s = \pi \cdot g \cdot (D_0 + g \cdot \sin\varphi). \quad (3)$$

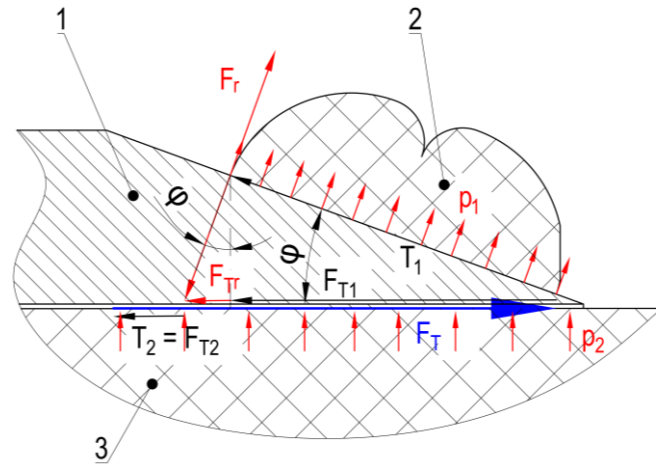


Fig. 9. The dependence between force vectors during flash removal: 1 – blade, 2 – flash, 3 – belt; F_T – flash removal process force, F_{Tr} – cutting force component from the stretching of the flash on the conical surface of the blade, F_{T1} – force component from flash friction on the blade conical surface, F_{T2} – force component from belt friction inside the blade bore, F_r – singular force stretching the flash, φ – blade side angle of inclination, p_1 – flash bearing pressure on the blade surface, T_1 – total frictional force on the blade surface, between the flash and the conical blade surface, T_2 – total frictional force between the belt surface and blade bore

Contact stress p_1 , can be calculated from Hooke's law, assuming average deformation on the conical surface for calculation (Osiński, 2007):

$$p_1 = \varepsilon_{AVG} \cdot E_p, \quad (4)$$

where: ε_{AVG} – mean flash deformation of the conical surface which is identified in the radial direction, E_p – longitudinal flexural modulus of the belt material. Mean deformation can be determined from the following formula:

$$\varepsilon_{AVG} = \frac{D_{AVG} - D_0}{D_0}, \quad (5)$$

where D_{AVG} mean diameter of the flash on the blade, and it is determined from the formula:

$$D_{AVG} = \frac{D_1 + D_0}{2}. \quad (6)$$

The external diameter of the flash on the blade can be calculated as below:

$$D_1 = D_0 + 2 \cdot g \cdot \sin\varphi. \quad (7)$$

Considering the formulas 2-7, the component of cutting force from flash stretching on the conical surface of the blade F_{Tr} , can be determined from the formula as below:

$$F_{Tr} = \frac{g^2 \cdot \sin^2\varphi \cdot E_p \cdot \pi}{D_0} \cdot (D_0 + g \cdot \sin\varphi). \quad (8)$$

Tab. 1. Major parameters assumed for calculating the process force for removal of flash after butt welding of drive belts

1	Designation:	Value:				Source:
Blade side angle of inclination	φ [°]	5	10	15	20	Assumed – manufactured blades
Blade bore diameter	D_0 [mm]	4.1	4.1	4.08	4.09	Measured
Average belt diameter during examination	D_c [mm]	4.11	4.11	4.11	4.11	Measured
Length of the cylindrical section of the blade	l [mm]	20	20	20	20	Assumed
Poisson's coefficient of the belt	ϑ_p	0.5	0.5	0.5	0.5	Assumed
Young's modulus of the belt	E_p [MPa]	50	50	50	50	(Waleśa et al., 2019)
Poisson's coefficient of the sleeve	ϑ_t	0.33	0.33	0.33	0.33	Assumed
Young's modulus of the sleeve	E_t [MPa]	210000	210000	210000	210000	Assumed
Flash thickness	g [mm]	1.60	1.73	1.81	1.96	Measured

The component F_{T1} of the F_T is the process force from friction of the flash on the conical surface of the blade can be derived from the general dependence:

$$F_{T1} = T_1 \cdot \cos\varphi, \tag{9}$$

where T_1 – is the total frictional force on the blade surface, between the blade surface, between the flash and the conical surface of the blade. The value can be calculated from the below formula:

$$T_1 = \frac{F_r}{tg\varphi}, \tag{10}$$

Force stretching the flash F_r , considering the formulas 2–7 is expressed as follows:

$$F_r = \frac{F_{Tr}}{\sin\varphi} = \frac{g^2 \cdot \sin\varphi \cdot E_p \cdot \pi}{D_0} \cdot (D_0 + g \cdot \sin\varphi). \tag{11}$$

Considering the formulas 9, 10 and 11, the force value F_{T1} is ultimately derived from the formula:

$$F_{T1} = \frac{g^2 \cdot \cos^2\varphi \cdot E_p \cdot \pi}{D_0} \cdot (D_0 + g \cdot \sin\varphi). \tag{12}$$

The component F_{T2} of the cutting force F_T , from the friction of the belt on the cylindrical surface of the blade bore can be derived from the formula:

$$F_{T2} = p_2 \cdot \pi \cdot D_0 \cdot l \cdot \mu, \tag{13}$$

whereas: μ – coefficient of friction between the belt and the cutting sleeve, p_2 – belt bearing pressure in the blade bore, which can be determined from the formula (Osiński, 2007):

$$p_2 = c \cdot w, \tag{14}$$

where, w – effective relative interference of belt and sleeve composition, which can be calculated with the formula as below:

$$w = \frac{D_c - D_0}{D_0}, \tag{15}$$

as well as the strain coefficient of the coupled pair belt-sleeve c , is calculated from the formula:

$$c = \frac{1}{\frac{\delta_t + \vartheta_t}{E_t} + \frac{\delta_p + \vartheta_p}{E_p}}, \tag{16}$$

where, δ_t – is the characteristic coefficient of the coupling for the sleeve, whereas δ_p – is the characteristic coefficient for the belt. These coefficient are calculated using the formulas:

$$\delta_t = \frac{1 + \frac{D_0^2}{D_c^2}}{1 - \frac{D_0^2}{D_c^2}}, \tag{17}$$

$$\delta_p = \frac{1 + \frac{D_c^2}{D_0^2}}{1 - \frac{D_c^2}{D_0^2}}. \tag{18}$$

The calculations following the presented methodology were carried out for all rake angles. Major variable values used in the calculations are provided in Table 1.

3. RESULT ANALYSIS

The study with the first proposed method of removing the flash, that is, using two blades and compressing the flash between them has failed. During the first test, the blades were damaged by the sharp, brittle edges of the blades colliding in the final stage of the operation. It was therefore decided to discontinue further examination using this method as under industrial conditions, it is unacceptable to damage the working components after each processed belt.

The study of the second proposed method, that is, drawing the belt with the flash between the blades were also unsatisfactory. The flash was not removed completely. This is caused by the peculiar characteristics of the belt material, it is very flexible and subject to significant flexible deformation. The belt would become significantly elongated before the blade, reducing its diameter. The flash was similarly deformed, which caused it to squeeze through the bore in the cutting sleeve without being removed. Consequently, further examination using this method was discontinued.

The study of the third method, that is, pressing the flash with the blade to a flat support with an opening proved to be successful. The flash was removed in its entirety in every attempt. The results of empirical study as well as analytical calculations are juxtaposed in Table 2 and Fig. 10. For the considered processing method, a relatively good approximation of actual examination results were obtained with the analytical model. The difference in the results, no more than approx. 8% was caused by the likely occurrence of flexing reactions during the removal process. Furthermore, a good repeatability of empirical study results was achieved.

Tab. 2. Results of analytical calculations and empirical data of one-sided cutting of flash with support plate

Analytical calculations				
Blade inclination 2φ [°]	10	20	30	40
Force constituent from stretching of the flash F_{T_r} [N]	3.80	18.23	46.01	98.19
Force constituent from friction between the flash and blade F_{T_1} [N]	496.19	586.40	640.87	741.20
Force constituent from friction between the belt and sleeve bore F_{T_2} [N]	12.56	12.56	37.69	25.12
Total calculated flash cutting force F_T [N]	512.55	617.19	724.57	864.50
Empirical data				
Average flash cutting force F_T [N]	554.85	643.10	740.45	897.74
Standard deviation of population σ [N]	70.81	51.43	67.65	128.84
Percentage difference between empirical and analytical data [%]	8.25	4.20	2.19	3.84

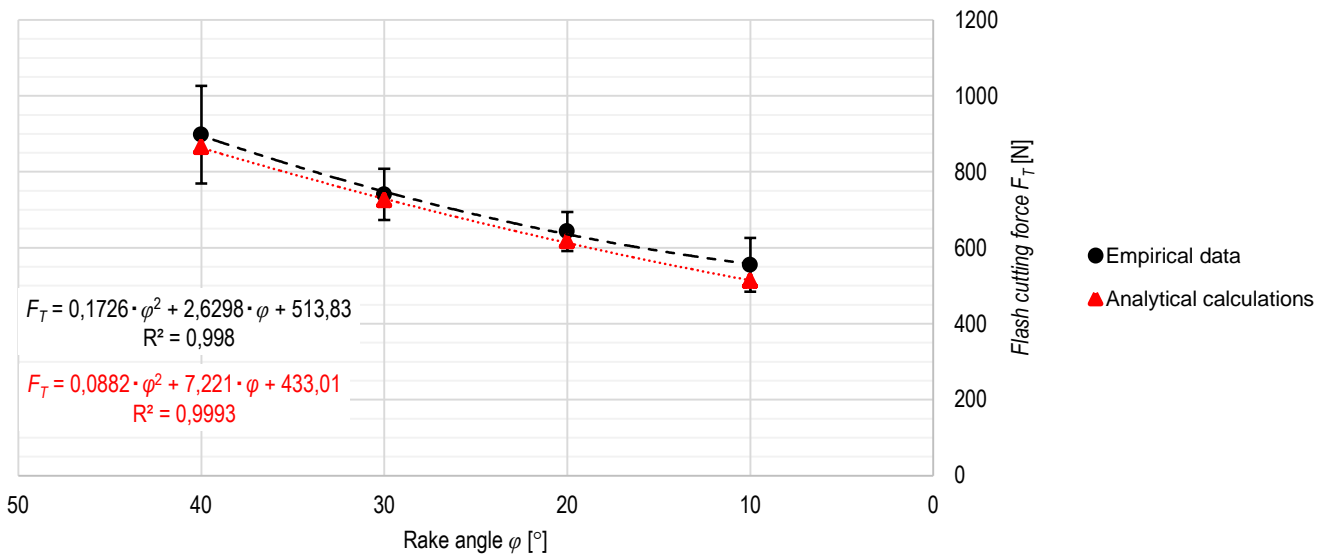


Fig. 10. Results of empirical examination and analytical calculations of force required for removal of the flash depending on rake angle

4. CONCLUSIONS

The removal of flash after hot plate butt welding is a deceptively simple technical operation with easy to implement kinematics in an automated device. However, the peculiar characteristics of the processed material (primarily, the high flexibility of the belt) mean that not every processing method can be successfully employed in this case. As indicated by the performed examinations, the removal of the flash utilizing the double blade method is possible, but not suitable for application under industrial conditions. The method of one-sided cutting of the flash by drawing the belt through the conical blade was also unsuccessful due to high flexibility of the belt.

Therefore, the best approach to carry out this process is one-sided cutting action utilizing a supporting plate. Analysing both the calculated and empirical data, one can observe a significant increase of the cutting force on the flash with the increase of the blade rake angle. As indicated in the analysis of force distribution during flash removal, it is caused by a material increase of the stretching force of the flash on the surface of the conical blade, which subsequently causes a material increase in the frictional force on the conical section of the blade together with the increase in rake angle.

REFERENCES

1. **Amanat N., James N. L., McKenzie D.R.** (2010), Welding methods for joining thermoplastic polymers for the hermetic enclosure of medical devices, *Medical engineering & Physics*, 32, 690–699.
2. **Amancio-Filho S.T., dos Santos J.F.** (2009), Joining of Polymers and Polymer-Metal Hybrid Structures: Recent Developments and Trends, *Polymer Engineering and Science*, 49(8), 1461–1476.
3. **BASF** (2010), *Thermoplastic Polyurethane Elastomers, Elastollan® - Material Properties*, BASF.
4. **Behabelt** (2015), *Product Catalogue 2015/2016*, Behabelt, Glottental.
5. **Broniewicz T., Iwasiewicz A., Kapko J., Placzek W.** (1970) *Methods of researches and examination of plastics properties (in Polish)*, WNT, Warszawa.
6. **Casalino G., Ghorbel E.** (2008), Numerical model of CO₂ laser welding of thermoplastic polymers, *Journal of Materials Processing Technology*, 207, 63–71.
7. **Ciszewski A., Radomski T.** (1989), *Construction materials in machine design (in Polish)*, PWN, Warszawa.
8. **Cocard M., Grozav I., Iacob M., Caneparu A.** (2009), Establishing the Optimum Welding Procedure for PE 100 Polyethylene Pipelines Using the Response Surface Design, *Materiale Plastice*, 46(4), 452–457.
9. **Domek G., Dudziak M.** (2011), Energy Dissipation in Timing Belts Made From Composite Materials, *Advanced Material Research*, 189-193, 4414–4418.

10. Domek G., Kołodziej A., Dudziak M., Woźniak T. (2016), Identification of the quality of timing belt pulleys, *Procedia Engineering*, 177, 275–280.
11. Evers F., Schöppner V., Lakemeyer P. (2017), The influence on welding processes on the weld strength of flame-retardant materials, *Weld World*, 61, 161–170.
12. Fierek A., Malujda I., Talaśka K. (2019), Design of a mechatronic unit for applications of coats of adhesive, *MATEC Web of Conferences*, 254, 01019.
13. Górecki J., Malujda I., Wilczyński D. (2019), The influence of geometrical parameters of the forming channel on the boundary value of the axial force in the agglomeration process of dry ice, *MATEC Web of Conferences*, 254, 05001.
14. Grewell D., Benatar A. (2007), Welding of plastics: fundamentals and new developments, *International Polymer Processing*, 22(1), 43–60.
15. Groover M. P. (2015), *Fundamentals of modern manufacturing*, Wiley, 503-510.
16. Inoue T., Miyata R., Hirai S. (2016), Antagonistically Twisted Round Belt Actuator System for Robotic Joints, *Journal of Robotics and Mechatronics*, 28(6), 842–853.
17. Jasiulek P. (2006), *Joining of plastics by welding, glueing and laminating (in Polish)*, Wydawnictwo "KaBe", Krosno.
18. Klimpel A. (1999), *Metals and thermoplastic polymers welding technology (in Polish)*, Wydawnictwo Politechniki Śląskiej, Gliwice.
19. Klimpel A. (2000), *Welding of thermoplastics materials (in Polish)*, Wydawnictwo Politechniki Śląskiej, Gliwice.
20. Krawiec P., Grzelka M., Krocak J., Domek G., Kołodziej A. (2019), A proposal of measurement methodology and assessment of manufacturing methods of nontypical cog belt pulleys, *Measurement*, 132, 182–190.
21. Krawiec P., Waluś K., Warguła Ł., Adamiec J. (2018), Wear evaluation of elements of V-belt transmission with the application of the optical microscope, *MATEC Web of Conferences*, 157, 01009.
22. Krishnan C., Benatar A. (2004), Analysis of Residual Stress in Hot Plate Welded Polycarbonate, *ANTEC 2004 Proceedings: Plastics*, 1149–1153.
23. Kukla M., Tarkowski P., Górecki J., Malujda I., Talaśka K. (2015), The Effect of Magnetic Field on Magnetorheological Composites. Artificial Neural Network Based Modelling and Experiments, *Applied Mechanics And Materials*, 816, 327–336.
24. Madej M., Ozimina D. (2010), *Plastics and composite materials (in Polish)*, Wydawnictwo Politechniki Świętokrzyskiej, Kielce.
25. Marciniak Z. (1959), *Punching dies construction (in Polish)*, WNT, Warszawa, 299–302.
26. Mokhtarzadeh A., Benatar A. (2012), Experiments with conventional and high temperature hot plate welding of thermoplastics using temperature and pressure control, *ANTEC 2012 Proceedings: Plastics*, 1684–1690.
27. Nieh J., Lee J. (1992), Hot Plate Welding of Polypropylene Part I: Crystallization Kinetics, *Polymer Engineering and Science*, Vol. 38, 1121–1132.
28. Osiński Z. (2007), *Basics of machine design (in Polish)*, PWN, Warszawa, 157–163.
29. Pietrzak M., Wałęsa K., Górecki J., Berdychowski M. (2019) Analysis of the friction (spin) welding – preliminary study, *MATEC Web of Conferences*, 254, 02036.
30. Potente H., Schneiders J., Bornemann M. (2002), Theoretical model for the one-dimensional temperature and stress calculation of simple hot plate welded geometries, *Macromolecular Materials and Engineering*, 287, 843–853.
31. Puszka A. (2006), *Polyurethanes – sources, properties and modifications (in Polish)*, Zakład Chemii Polimerów, Wydział Chemii Uniwersytetu Marii Curie Skłodowskiej w Lublinie, Lublin.
32. Rzasinski R. (2017), The algorithm of verification of welding process for plastic pipes, *IOP Conference Series: Materials Science and Engineering*, 227, 012113.
33. Sikora R. (1993), *Polymers processing (in Polish)*, Wydawnictwo ŻAK, Warszawa.
34. Talaśka K., Ferreira A. (2017), An Approach to Identifying Phenomena Accompanying Micro and Nanoparticles in Contact With Irregular Vessel Walls, *Transactions on NanoBioscience*, 16(6), 463–475.
35. Talaśka K. (2018), *Study of research and modelling of the loose and shredded materials compaction process (in Polish)*, Wydawnictwo Politechniki Poznańskiej, Poznań.
36. Troughton M. (1997), *Handbook of Plastics Joining: A practical guide*, Plastics Design Library, New York.
37. Wałęsa K., Malujda I., Talaśka K. (2018), Butt welding of round drive belts, *Acta Mechanica et Automatica*, 12(2), 115–126.
38. Wałęsa K., Malujda M., Górecki J., Wilczyński D. (2019), The temperature distribution during heating in hot plate welding process, *MATEC Web of Conferences*, 254, 02033.
39. Wałęsa K., Mysiukiewicz O., Pietrzak M., Górecki J., Wilczyński D. (2019), Preliminary research of the thermomechanical properties of the round drive belts, *MATEC Web of Conferences*, 254, 06007.
40. Wanqing L., Changqing F., Xing Z., Youliang C., Rong Y., Donghong L. (2017), Morphology and thermal properties of polyurethane elastomer based on representative structural chain extenders, *Thermochimica Acta*, 653, 116–125.
41. Wilczyński D., Malujda M., Górecki J., Domek G. (2019), Experimental research on the proces of cutting transport belts, *MATEC Web of Conferences*, 254, 05014.
42. Wojtkowiak D., Talaśka K. (2019), Determination of the effective geometrical features of the piercing punch for polymer composite belts, *The International Journal of Advanced Manufacturing Technology*, <https://doi.org/10.1007/s00170-019-03746-7>.
43. Wojtkowiak D., Talaśka K., Malujda I., Domek G. (2018), Estimation of the perforation force for polymer composite conveyor belts taking into consideration the shape of the piercing punch, *The International Journal of Advanced Manufacturing Technology*, 98(9-12), 2539–2561.
44. Yousepour A., Hojjari M., Immarigeon J-P. (2004), Fusion Bonding/Welding of Thermoplastic Composites, *Journal of Thermoplastic Composite Materials*, 17, 303–341.
45. Żuchowska D. (2000), *Construction polymers (in Polish)*, WNT, Warszawa.

PREDICTIVE CONTROL OF THE IRON ORE BENEFICIATION PROCESS BASED ON THE HAMMERSTEIN HYBRID MODEL

Olga PORKUIAN,* Vladimir MORKUN,** Natalia MORKUN,** Oleksandra SERDYUK**

*Faculty of Information Technology and Electronics, Department of Programming and Mathematics,
 Volodymyr Dahl East Ukrainian National University, pr. Central 59-a, Severodonetsk, 93400, Ukraine

**Faculty of Information Technologies, Computer Science and Technology Department, Kryvyi Rih National University,
 11 Vitaliy Matusevych St., Kryvyi Rih, 50027, Ukraine

oporkuian@gmail.com, morkunv@gmail.com, nmorkun@gmail.com, o_serdiuk@i.ua

received 2 August 2019, revised 13 January 2020, accepted 15 January 2020

Abstract: Non-linear, dynamic, non-stationary properties characterize objects of the iron ore beneficiation line. Therefore, for their approximation, it is advisable to use models of the Hammerstein class. As a result of comparing the three models of Hammerstein: simple, parallel and recursive-parallel, it was shown that the best result for identifying the considered processes of magnetic beneficiation of iron ore by the minimum error criterion was obtained using the Hammerstein recursive-parallel model. Hence, it is recommended for the identification of beneficiation production objects.

Key words: Predictive control, iron ore, beneficiation, Hammerstein model, recursive-parallel model

1. INTRODUCTION

Providing metallurgical production with high-quality raw materials remains an urgent problem. The growth in mineral consumption requires the expansion of the raw material base, ensuring the necessary quality of raw and marketable ore, and increasing the profitability of mining and processing enterprises (Abonyi et al., 2000; Babuska, 1998). Over the past 20–30 years, the iron content in the extracted ore at the mining enterprises of Ukraine decreased by an average of 12.9% (Babuska, 1998; Babuska, 1998). Considering the current characteristics of raw materials processed at processing plants and the state of technological equipment when forming control actions in automatic control systems allows optimizing the technological process and increasing its technical and economic indicators. Thus, increasing the iron content in the concentrate from 64 to 65% allows in the sintering redistribution – to reduce ore consumption by 29–32 kg/t and fluxes – by 30 kg/t; in the metallurgical division – to reduce the consumption of coke by 2.6–2.8%, to increase the relative productivity of the blast furnace by 4.5–5%. All this helps to reduce the total cost of iron production by about 4% (Abonyi et al., 2000). This work aims to increase the efficiency of the automated control of the magnetic beneficiation processes of iron ores by developing theoretical bases and building predictive control of these processes based on Hammerstein models. Based on the results of the study and analysis of the problem of increasing the efficiency of automated control of iron ore beneficiation processes, the control concept and research objectives are formulated:

- to develop and study the models (in the class of Hammerstein models) and methods for the rapid identification of iron ore beneficiation processes as nonlinear dynamic objects, considering the interchangeability of their properties;

- to develop algorithms for predictive control of iron ore beneficiation processes based on the Hammerstein models.

The object of the study is dynamic technological processes and transformations in the presence of fuzzy and incomplete information that occurs during the concentration of iron ores, methods, and systems for automatic control of these processes. The subject of the research is models and algorithms for identifying nonlinear dynamic objects, predictive control algorithms, an automated process control system (APCS) of iron ore beneficiation. An analytical review of the work on the problems of automatic control of iron ore beneficiation processes showed that under conditions when the ore characteristics and the condition of technological equipment change, the final performance of the processing plant is mostly dependent on the efficiency of automatic control of technological units, which is primarily determined by its quality information and algorithmic support. Effective control requires the constant and rapid provision of a significant amount of data on the state of the control object (the content of the useful component in the product, the particle size distribution of the pulp at various points in the process, the concentration of the solid phase and pulp density, etc.), as well as high-speed algorithms for their processing with the aim of identification of the object and definition of control actions.

The same tendency also occurs in mining enterprises of other countries. Reducing the metal content in raw ore increases the resource intensity of production and the cost of finished products. To solve the problems of the synthesis of automatic control systems of nonlinear non-stationary objects, operating under severe restrictions, which are imposed on state and control variables, the Model Predictive Control method (MPC) (Zubov, 2006) and its modifications – Adaptive Model Predictive Control have recently been actively used (Sanches and Rodellar, 1996). Simplified, the idea of these methods is to use the variable values extrapolated to

a certain depth in such a way as to minimize the future deviation of the system from the desired state during the formation of the control law, and thereby, ensure optimal control. At present, the Predictive Control paradigm has achieved such successes, including in industrial applications, which is considered by many authors as an alternative to PID regulation for complex multidimensional systems (Rossiter, 2003).

In (Zubov, 2006; Morkun and Tcvirkun, 2014; Sanches and Rodellar, 1996; Rossiter, 2003; Morkun et al., 2014a), various control schemes based on MPC are presented. The variant of the control structure proposed in Morkun et al. (2014a) allows multi-criteria optimization with ranking criteria by priority. Most control facilities at the processing plants have both dynamic and nonlinear properties. The identification of such objects often causes significant difficulties. Some methods for the identification of nonlinear dynamic objects are considered in Ivanov (1991), Morkun et al. (2015a), Morkun et al. (2014b), Yucai (1999), Leontaritis and Billings (1987), Stoica (1981) and Morkun et al. (2018). As the analysis of these works shows, a common technique for identifying dynamic nonlinearity is the artificial separation of these two properties. The object is represented by a set of nonlinear static and linear dynamic blocks. In this case, N. Wiener proposed to consider a sequential connection in the following order: a dynamic block, followed by nonlinearity (Morkun et al., 2014c; Li and Shchetsen, 1968; Yucai, 1999; Stoica, 1981). An alternative variant is a nonlinear block, followed by a dynamic one, proposed by Hammerstein and was considered in Shi and Sun (1990), Ivanov (1995), Narendra and Gallman (1966), Leontaritis and Billings (1987), Sjoberg (1995) and Stoica (1981).

In this case, a simple sequential Wiener model turns out to be more profitable for about half of the real objects than a simple Hammerstein model (Morkun et al., 2015b). However, in such a simple version, Wiener and Hammerstein models are used extremely rarely. In most cases, the object of identification is approximated by various combinations of these simple models. In this case, as shown by the studies carried out by the authors (Morkun et al., 2015b; Shi and Sun, 1990; Ivanov, 1995; Verhaegen and Westwick, 1996), parallel and recursive-parallel models turned out to be the best by the criterion of 'simplicity-quality'. These models are a parallel connection of single-type simple links. In papers (Morkun et al., 2015b; Shi and Sun, 1990), an essential feature of parallel models with an unlimited number of parallel branches was emphasized. The use of this class of models eliminates the solution of a complicated problem of choosing a model structure.

The question of choosing the parallel model structure is no longer determined by the accuracy of the model, but by the possibilities for effectively identifying its parameters. In this regard, the parallel Hammerstein model turns out to be more profitable, since it allows one-dimensional orthogonal identification algorithms (Ivanov, 1991), which do not impose any severe restrictions on the type of input test actions. The one-dimensional algorithms for identifying the parameters of the parallel Wiener model are not orthogonal (Young, 1977). Orthogonal algorithms for Wiener models are multidimensional and require significant computational resources.

In principle, it is possible to use not only parallel models but also sequential models containing a set of series-connected simple models of Hammerstein or Wiener. However, this approach is not used in practice since it has proven difficult to formalize and is associated with simulation modeling, which requires significant computational resources (Morkun et al., 2015b).

Recently, scientific papers have been published, which offer

various options for increasing the efficiency and ease of use of Hammerstein models. So, in Ikhouane and Girib (2014) a unified framework for the identification of Wiener and Hammerstein systems that is valid for SISO and MIMO systems, discrete- and continuous-time settings, and with the only a priori knowledge that the system belongs to the set including Wiener and Hammerstein models is presented. The paper Ozer et al. (2016) studies the application of system identification of the Hammerstein model, which is a cascade of nonlinear second-order Volterra and a linear FIR model. The recursive least squares algorithm is used to determine the parameters of the proposed Hammerstein model. In (Rébillat et al., 2010), it is shown that the cascade of Hammerstein models makes it possible to describe a large class of nonlinearities conveniently. A simple method is proposed based on the phase property of exponential sinusoids for identifying the structural elements of such a model using only one measured system response. Ma et al. (2016) discusses the problem of estimating the state and parameters for a class of Hammerstein state space systems with a time delay. Both process noise and measurement noise are taken into account in the system. Based on the observed space form of canonical states and the separation of critical terms, a pseudo-linear regressive identification model is obtained. For unknown states in the information vector, the Kalman filter is used to search for optimal state estimates. Least squares algorithms based on the Kalman filter and recursive least squares algorithms are proposed. In Chen and Wang (2015), the problem of parameter identification for a Hammerstein system with continuous nonlinearity is studied. Taking into account the unknown structure of continuous nonlinearity, a Weierstrass approximation theorem is introduced to simplify nonlinearity. Then a stochastic gradient algorithm and an algorithm for optimizing a swarm of particles to estimate all unknown parameters of the Hammerstein system are proposed. In Chen and Ding (2015), the hierarchical least-squares algorithm is developed using the principle of hierarchical identification, which decomposes the nonlinear system into several subsystems with smaller sizes and fewer variables and estimates the parameters of each subsystem, respectively.

Importantly, the degree of adequacy of the model obtained is determined mainly by considering different types of uncertainty in the identification of the object. A significant error in the input data leads to an error in the calculation of the target function and, consequently, to a significant area of uncertainty in the choice of optimal control and optimal operation of the system. In Tobi and Hanafusa (1991), it was shown that only the representation of several constraints as fuzzy makes it possible to obtain a stable solution under conditions of inaccuracy of information and fuzziness of production constraints, with an indication of a reduced degree of admissibility of this mode, that is, as membership functions. Setting the problem in fuzzy form also significantly reduces the possibility of obtaining incompatible solutions for the calculation and optimization. In Abba et al. (2019), Hammerstein-wiener (HW), general regression neural network (GRNN), and non-linear autoregressive with exogenous (NARX) neural network, least-square support vector machine (LSSVM) models were employed for multi-parametric (Hardness (mg/L), turbidity (Turb) ($\mu\text{s/cm}$), pH and suspended solid (SS) (mg/L)). The comparison of the results of modeling showed that HW served as the best model for the simulation of Hardness, Turb, and SS. Mete et al. (2016) present the Hammerstein model, which is obtained by cascade form of a nonlinear second-order Volterra (SOV) and a linear FIR model. Besides, the proposed Hammerstein model is optimized with a differential evolution algorithm (DEA). In Le et al. (2012), the

recursive identification of Hammerstein structures is investigated. A recursive algorithm is then developed to address the limitations in the approaches currently available. The linear and nonlinear parameters are separated and estimated recursively in a parallel manner, with each updating algorithm using the most up-to-date estimation produced by the other algorithm at each time instant. Chen and Wang (2015) study the parameter identification problem for a Hammerstein system with continuous nonlinearity. Considering the unknown structure of the continuous nonlinearity, the Weierstrass approximation theorem is introduced to simplify the nonlinearity. Then a stochastic gradient algorithm and a particle swarm optimization algorithm are proposed to estimate all the unknown parameters of the Hammerstein system.

In Falck et al. (2012), consider the identification of Wiener–Hammerstein systems using the Least-Squares Support Vector Machines based models. Their study illustrates that black-box models are a suitable technique for the identification of Wiener–Hammerstein systems. Wills A. and Ninness (2012) examine the use of a so-called ‘generalized Hammerstein–Wiener’ model structure that is formed as the concatenation of an arbitrary number of Hammerstein systems. This approach is profiled using a Wiener–Hammerstein Benchmark example, which illustrates it to be effective and, via Monte-Carlo simulation, relatively robust against capture in local minima. Piroddi et al. (2012) analyse the performance of several black-box nonlinear model identification techniques for input-output models with polynomial nonlinearities on a benchmark identification problem.

The number of works devoted to the construction of fuzzy models, fuzzy control, and its various aspects is growing steadily, an example of some of which may be Tobi and Hanafusa (1991), Abonyi et al. (2000), and Postlethwaite (1996). The Takagi-Sugeno models have found wide application for the approximation of nonlinear systems, some examples of which were considered in Babuska (1998), Babuska (1998), Morkun et al. (2015c), and Kazuo and Wang (2001), in particular, there is a positive experience of using them to control individual objects of iron ore processing lines (Morkun and Tcvirkun, 2014; Morkun et al., 2015c).

2. MATERIALS AND METHODS

A significant role in the application of MPC approaches is performed by the model, based on which the future behaviour of the system is calculated. In order to make full use of the control capabilities using the MPC theory, it is necessary to provide an effective and fast identification of the characteristics of the control object, which will allow forming a model of this object quickly.

Therefore, when developing effective process control systems, the following essential aspects are relevant:

- development of new control algorithms and identification methods that make it possible to effectively use the information obtained, as well as considering the inevitable uncertainty and inaccuracy in the description of the control object;
- improvement of information support (improvement of measurement accuracy, the ability to measure additional parameters in the course of process control, the efficiency of information provided for control).

It should be noted that in recent years there has been a sharp increase in the number of studies devoted to the extraction of the fullest possible information about the control object (Ozer et al., 2016; Ma et al., 2016; Chen and Wang, 2015; Chen and Ding,

2015). To fulfil the goals of control, it is currently possible to use information not only in a formalized numerical form but also in linguistics, in the form of expert conclusions. Such work initiated intensive research based on the use of new mathematical applications in the field of identification and control.

The ore beneficiation processes are spatially distributed multi-dimensional automation objects with a complex, multi-connected structure. The beneficiation technological lines usually consist of several successively arranged stages, each of which includes the following main technological operations: grinding, classification, magnetic separation. The technological processes of ore processing plants provide for multistage crushing and grinding of ore to prepare it for the next separation (Morkun et al., 2014b; Morkun et al., 2015a; Morkun et al., 2018). The purpose of these operations is to reveal ore aggregates and to isolate fractions of various minerals from each other by reducing the size of mineral grains to 0.1 mm or less. As control objects, grinding units can be represented in the form of some operators that convert the vectors of input variables into vectors of output parameters. In turn, the output parameters of the grinding process must be considered as input for the next stage of the beneficiation process. Elements of the vectors of the output parameters of the grinding department are their qualitative and quantitative indicators. The main quantitative indicators are feed productivity and finished class size productivity. The quality of the crushed product is characterized by the density or solid content in the pulp, the granulometric composition of the solid phase, as well as the quality indicators of the initial ore (content of useful components, mineral composition, etc.), not depending on the technological mode of operation of the grinding cycle. Thus, the elements of the vector of output parameters formed by the grinding redistribution (productivity and particle size distribution of the product) can be taken as control actions in solving problems of optimizing the beneficiation process.

Let’s consider the synthesis of control based on Hammerstein models for the first stage of iron ore beneficiation as an integral part of the entire iron ore beneficiation processing line, which makes a decisive contribution to the final result. As shown in Ozer et al. (2016), Morkun et al. (2014b), Sanches and Rodellar (1996), and Narendra and Gallman (1966), most technological devices of this stage of beneficiation correspond in their properties to the models of Hammerstein. The generalized control scheme is presented in Fig. 1.

The following notation was used: 1 – mill, 2 – classifier, 3 – magnetic separator, 4 – conveyor, 5 – bunker, 6 – drive motor, 7 – water flow valve, 8 – ore supply control system, 9 – the classifier water supply control system, 10 – an identification subsystem, 11 – a driver of control actions, 12 – an optimizer, 13 – a sensor of industrial product parameters, 14 – an ore consumption sensor; 15 – information support subsystem, 16 – pulp parameter sensor.

The Hammerstein model, on the basis of which the predictive control will be implemented, is a combination of a fuzzy nonlinear block and a crisp linear dynamic block. Thus, the term ‘hybrid model’ corresponds to the structure of the model.

Let a static nonlinear block represents the object of study with an input vector $u = [u_1, \dots, u_n]^T$, a vector of converted input variables $v = [v_1, \dots, v_n]^T$, related to u_h according to

$$v_h = f_h(u_h), h = 1, \dots, n, \quad (1)$$

where, $f_h(u_h)$ are the functions characterizing nonlinear block by control h -channel, and a dynamic linear block with a vector of output variables $y = [y_1, \dots, y_m]^T$.

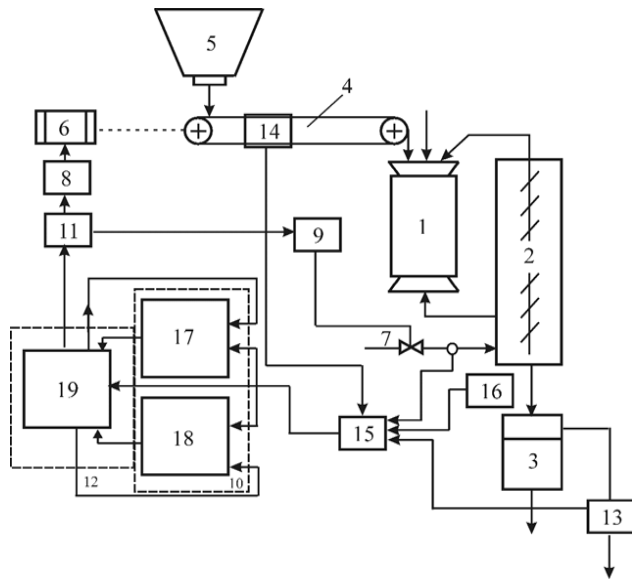


Fig. 1. The control scheme of the first stage of iron ore beneficiation

In the control circuit, we will use the combination of the control object and the inverse fuzzy model obtained by inversion of the fuzzy static block from the Hammerstein hybrid model. If we consider that the control object (CO) is identical to the Hammerstein hybrid model and its static nonlinearity corresponds to a fuzzy block, then the set of CO and the inverse fuzzy block can be considered as a linear dynamic block of the Hammerstein hybrid model. In this control scheme, the calculation results of \hat{y} corresponding to the linear block of the Hammerstein model is equal to the real initial variables y of CO. Based on the differences in 'model - real object', the control system is adapted. The proposed approach allows building control based on a standard linear generalized predictive controller (GPC). As follows from the studies published in Clarke et al. (1989), Fruzetti (1997), Garcia and Morari (1982), in the case of fuzzy modeling of systems such as one input - one output or multiple inputs - one output, the predictive GPC controller allows the efficient control. The proposed control circuit allows avoiding non-linear programming in the control algorithm or the use of linearization methods.

3. PROBLEM DEFINITION

When implementing a control algorithm, a sequence of controls is calculated $\{\Delta u(k + j)\}$, $j = 1, \dots, H_c$, which minimizes the cost function (Stoica, 1981):

$$J(H_{p1}, H_{p2}, H_{pc}, \lambda) = \sum_{j=H_{p1}}^{H_{p2}} (w(k + j) - \hat{y}(k + j))^2 + \lambda \sum_{j=1}^{H_c} \Delta u^2(k + j - 1), \quad (2)$$

where, $\hat{y}(k + j)$ are the process output parameters according to model; $w(k + j)$ are the modified state parameters, which are known in advance; H_{p1} is the minimum estimated horizon; H_{p2} maximum estimated horizon (forecast horizon); H_c is the control horizon; $\lambda = \lambda_0 K(u(k))^2$ is the limiting factor (Clarke and Mohtadi, 1989); $K(u(k))$ is the static transfer coefficient of a fuzzy block of the Hammerstein model:

$$K(u(k)) = \frac{\partial f(u(k))}{\partial u(k)}.$$

Then, considering (1), $\Delta v(k) \approx K(u(k))\Delta u(k)$ and (2) can be represented as:

$$J(H_{p1}, H_{p2}, H_{pc}, \lambda) \approx \sum_{j=H_{p1}}^{H_{p2}} (w(k + j) - \hat{y}(k + j))^2 + \lambda_0 \sum_{j=1}^{H_c} \Delta v^2(k + j - 1), \quad (3)$$

Thus, the linear dynamic model gives the output parameters $\hat{y}(k + j) = \sum_{i=1}^j g_i \Delta v(k + i - 1) + p_j$, based on which the GPC calculates the sequence of control actions $\{\Delta u(k + j)\}$; $j = 1, \dots, H_c$. At the same time, the response of the linear model on $k + j$ step p_j is determined based on the control signal in the previous steps and the value g_i :

$$p_j = \sum_{m=1}^j \sum_{i=m+1}^{N_g} g_i \Delta v(k + m - i), \quad j = 1, \dots, N_g,$$

$$g_j \begin{cases} 0, \forall j \leq n_d \\ -\sum_{i=1}^j a_i g_{j-i} + \sum_{i=1}^j b_i, f > n_d \end{cases}$$

where, N_g is the model horizon (Botto, 1999).

All predictable outputs can be formed into a vector $\hat{y} = [\hat{y}(k + H_{p1}), \dots, \hat{y}(k + H_{p2})]^T$, and write the basic equation of the GPC algorithm:

$$\hat{y} = G\Delta v + p, \quad (4)$$

where, $\Delta v = [\Delta v(k), \dots, \Delta v(k + H_c)]^T$,

$p = [p_{H_{p1}}, p_{H_{p1}+1}, \dots, p_{H_{p2}}]^T$, G - is the matrix $(H_{p2} - H_{p1} + 1) \times H_l$ with zero components for $j - i > H_{p1}$:

$$G = \begin{bmatrix} g_{H_{p1}} & g_{H_{p1}-1} & \dots & 0 \\ g_{H_{p1}+1} & g_{H_{p1}} & g_{H_{p1}-1} & \vdots \\ \vdots & \vdots & \ddots & \vdots \\ g_{H_{p2}} & g_{H_{p2}-1} & \dots & g_{H_{p2}-H_c+1} \end{bmatrix}.$$

If we do not consider the restrictions, then the optimal control can be calculated analytically from (4):

$$\Delta \bar{v} (G^T G + \lambda_0 I)^{-1} G (w - p). \quad (5)$$

If constraints are taken into account, we have to use quadratic programming to solve the optimization problem. To avoid this, a two-stage approach to the constraints of the optimization problem with restrictions is proposed. The optimal control problem is solved without considering the constraints, and for the obtained predictive controls, the fulfilment of the constraints is checked. If the result is positive, then the resulting controls are applied to the system. Otherwise, it is necessary to linearize the constraints and then calculate the optimal control by one of the known methods. Such a solution procedure is more computationally rational compared to the standard ones.

Let's consider the solution of the optimization problem (3) with prediction $\Delta \bar{v}$ in the presence of restrictions in the form of equality $M\Delta \bar{v} = k$ and restrictions in the form of inequality $L\Delta \bar{v} \leq c$.

In this case, a limited solution Δv^c can be found in the form:

$$\Delta v^c = \Delta \bar{v} - (G^T G + \lambda_0 I)^{-1} M^T \mu - (G^T G + \lambda_0 I)^{-1} \cdot L^T \eta, \quad (6)$$

where, μ and η are the Lagrange multipliers vectors, corresponding to restrictions in the form of equalities and inequalities.

We can find these vectors by solving a quadratic programming problem (Stoica, 1981):

$$\min_{\mu, \eta} \left\{ \begin{bmatrix} \mu \\ \eta \end{bmatrix}^T + H \begin{bmatrix} \mu \\ \eta \end{bmatrix} + g^T \begin{bmatrix} \mu \\ \eta \end{bmatrix} \right\}$$

$$\text{Where, } H = \begin{bmatrix} M(G^T G + \lambda_0 I)^{-1} M^T & M(G^T G + \lambda_0 I)^{-1} L^T \\ L(G^T G + \lambda_0 I)^{-1} M^T & L((G^T G + \lambda_0 I)^{-1} L^T) \end{bmatrix};$$

$$g = \begin{bmatrix} k - M\Delta\bar{v}^f \\ c - L\Delta\bar{v}^f \end{bmatrix}$$

At the same time, η is limited by positive evaluations. When solving practical problems, it is necessary from the limitations given for $u(k)$ and $\Delta u(k)$, go to $v(k)$ and $\Delta v(k)$, using dependencies $v(k) = f(u(k))$ and $\Delta v(k) \approx K(u(k))\Delta u(k)$. For example, from restrictions in the form:

$$\begin{pmatrix} I_{\Delta u} \\ -I_{\Delta u} \\ I_{H_c} \\ -I_{H_c} \end{pmatrix} \Delta u \leq \begin{pmatrix} u_{max} - I_u u(k-1) \\ -u_{min} + I_u u(k-1) \\ \Delta u_{max} \\ -\Delta u_{min} \end{pmatrix}, \quad (7)$$

we can go to restrictions $L\Delta v \leq c$ in the form:

$$\begin{pmatrix} I_{\Delta u} \\ -I_{\Delta u} \\ I_{H_c} \\ -I_{H_c} \end{pmatrix} \Delta v \leq \begin{pmatrix} v_{max} - I_v v(k-1) \\ -v_{min} + I_v v(k-1) \\ \Delta\bar{v}_{max} \\ -\Delta\bar{v}_{min} \end{pmatrix}, \quad (8)$$

where, $v_{min} = f(u_{min})$, $v_{max} = f(u_{max})$, $\Delta\bar{v}_{min} = \Delta v_{min}K$, $\Delta\bar{v}_{max} = \Delta v_{max}K$, $K = [K(u(k)), \dots, K(u(k + H_c))]$.

In order to calculate Δv_{min} and Δv_{max} , it is necessary to know the vector K , caused by the sequence of predicted controls, which are unknown at the time of calculations in step k . To determine this sequence, we can use algorithms, which are similar to the limited control method for linearized feedback.

Let's consider two algorithms for determining the control sequence (operating trajectory) for the fuzzy Hammerstein model with inversion of static nonlinearity. The first method allows choosing the optimal operating trajectory, considering the constraints imposed on it by inequality (8).

Algorithm 1.

1. Determine unlimited optimal control $\Delta\bar{v}$, by solving (5).
2. Transform $\Delta\bar{v}$ and Δu through non-linear mapping inversion f^{-1} .
3. Check the resulting control sequence for compliance with the constraints (7). If the constraints are satisfied, the resulting control is applied to the system in accordance with the methodology of the MPC (principle of prediction horizon, which moves away). If the restrictions are not met, then go to step 4.
4. Linear constraints are calculated in the form of inequalities (8), approximating the vector K with respect to the initially obtained sequence of controls.
5. Optimal forecast $\Delta\bar{v}^c$, calculated according to (6), using pre-computed constraints (Step 4).
Go to step 2.

Studies of similar algorithms show that the algorithm should converge to a suboptimal solution (Morkun et al., 2014b). If the resulting sequence of controls is not feasible, then it is recommended to strengthen the restrictions so that the solution is guaranteed to be feasible. To do this, take $\Delta v_{min} = \Delta v_{min}K_{max}$ and

$\Delta v_{max} = \Delta v_{max}K_{min}$, wherein K_{min} and K_{max} are calculated as follows:

$$\begin{aligned} K_{min,i} &= \min_u K(u), \\ \forall u &\in [u(k-1) - i\Delta u_{min}, u(k-1) + i\Delta u_{max}], \\ K_{max,i} &= \max_u K(u), \\ \forall u &\in [u(k-1) - i\Delta u_{min}, u(k-1) + i\Delta u_{max}]. \end{aligned} \quad (9)$$

Now for optimal prediction $\Delta\bar{v}^c$, found from (6), the restriction $L\Delta\bar{v} \leq c^*$ is applied in accordance with (7) and (8), which ensures the known feasibility of the solution. The proposed algorithm may increase the constraints imposed on the control too much. Therefore, as an alternative variant, it is possible to propose a different algorithm, which adapts NOT for control, but control constraints (in the form of linear inequalities).

Algorithm 2.

1. Calculate the constraints c^* similar to (7) considering (9).
2. Determine the vector \hat{c} as the initial approximation of the constraints, calculated in accordance with Step 4 of Algorithm 1 for the last iteration.
3. Set new restrictions $L\Delta\bar{v} \leq c$, where c is a linear combination c^* and \hat{c} , that is,
 $c = \eta c^* + (1 - \eta)\hat{c}$ (η - a certain step size).
4. Calculate the optimal prediction $\Delta\bar{v}^c$ according to (6), considering (8), and transform $\Delta\bar{v}^c$ to the real sequence of controls Δu (by inverse nonlinear mapping).
5. If restrictions (7) are not violated, apply to the system the received controls in accordance with the MPC procedure. Otherwise, go to Step 3. The scheme of this algorithm is shown in Fig. 2.

The determination of unlimited optimal control Δv^f according to (5):

$$\Delta v^f = (G^T G + \lambda_0 I)^{-1} G(w - p),$$

$$\text{where } \Delta v = [\Delta v(k), \dots, \Delta v(k + H_c)]^T,$$

$$p = [p_{Hp1}, p_{Hp1+1}, \dots, p_{Hp2}]^T,$$

$$p_j = \sum_{m=1}^j \sum_{i=m+1}^{N_g} g_i \Delta v(k + m - i), j = 1, \dots, N_g, \text{ is performed in block 6.}$$

Then the resulting control sequence Δv^f let's transform into a sequence of real controls Δu by the non-linear mapping inversion f^{-1} (block 8).

Block 9 is used to verify the received control sequence for compliance with the restrictions (7). If the restrictions are satisfied, then the resulting control is applied to the system in accordance with the predictive control methodology based on the MPC model. If the restrictions are not met, then the parameters of the fuzzy block in the hybrid model of Hammerstein are specified in accordance with (8) according to the initial control sequence (block 11).

Block 12 according to the updated data calculates a new prediction Δv^{fc} according to (6) $\Delta v^c = \Delta v^f = (G^T G + \lambda_0 I)^{-1} M^T \mu - (G^T G + \lambda_0 I)^{-1} L^T \eta$, by which the specified sequence of controls is determined. If $\eta = 1$, then we get a case of severe restrictions corresponding to the worst-case analysis, which gives a guaranteed feasible solution for control and convergence of the procedure.

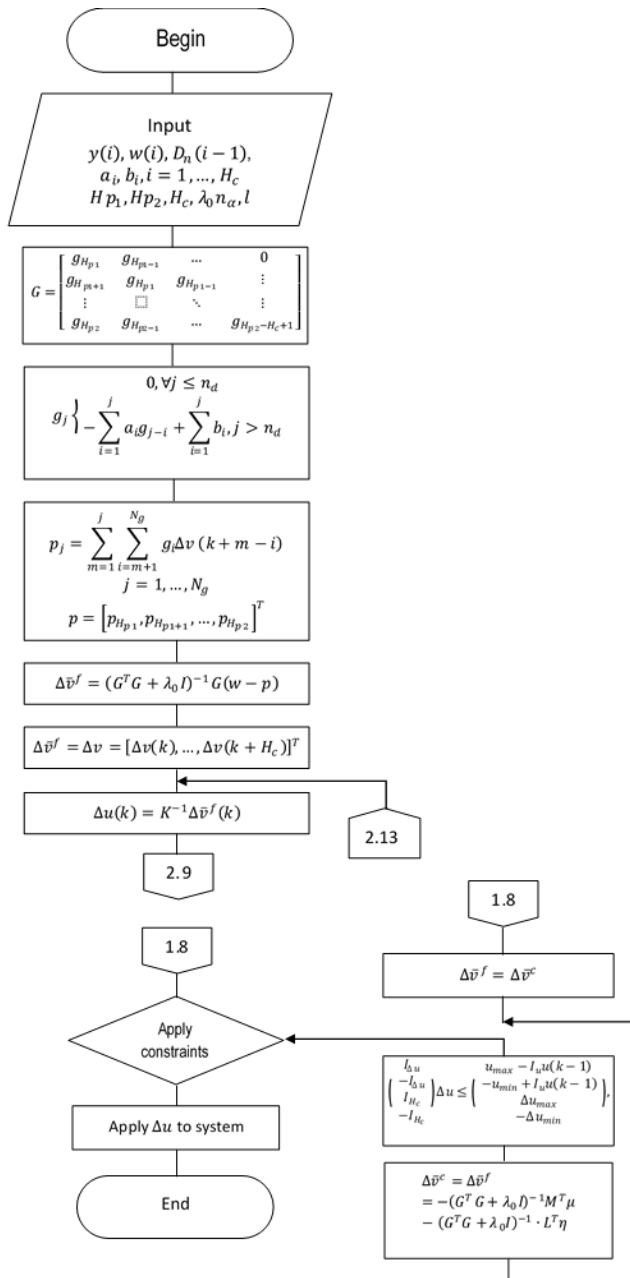


Fig. 2. Scheme of the control algorithm

4. RESULTS AND ANALYSIS

When implementing the control according to the scheme shown in Fig. 1, the value of the mill productivity by ore $u_1 = Q_1$ and water flow rate in the classifier $u_2 = Q_2$ were used as control actions. As output indicators – performance on the intermediate product $y_1 = Q_{pr}$, iron content in the solid phase of the intermediate product $y_2 = \beta_{pr}$ and the loss of a useful component in the tails $y_3 = \beta_t$ were used. In the course of control, the water flow rate into the mill was calculated while observing the ratio of ore to water within the limits of given parameters.

The control actions were formed based on measuring the iron content of the magnetic and solid phases in the pulp (sensors 13, 16), the concentration of particles of control size grades in the pulp at the discharge of classifier 2 (sensor 16), processed by the information support subsystem 15, the structure and operation principles of which are described in Morkun et al. (2015b).

For approximation, a discrete model with a fuzzy nonlinear block was used. For each input variable, three terms were applied, according to the Hammerstein hybrid model. Three terms with kernels of 16%; 24%; 32% for the pulp density of the classifier discharge and two terms with kernels of 220; 230; 240 for mill productivity by ore.

According to the measured input and output variables, the subsystem 10 identifies the control object, builds the Hammerstein hybrid model. The linear dynamic block is approximated by a model:

$$\hat{y}(k + 1) = \sum_{i=1}^{n_y} A_i \hat{y}(k - i + 1) + \sum_{i=1}^{n_u} \sum_{j=1}^{N_1} \sum_{l=1}^{N_2} \sum_{p=1}^{N_3} B_i d_{jlp} \beta_{jlp} (u(k - i - n_d + 1)),$$

where, matrices A_i and B_i for the considered case, have dimension 3×3 , N is the number of fuzzy sets for the corresponding input ($N_1 = 3, N_2 = 3, N_3 = 3$), $\hat{y}(k + i)$ is the vector of output indicators (three components of the vector - $y_1 = Q_{pr}, y_2 = \beta_{pr}, y_3 = \beta_t$).

By measurements of input and output indicators step by step, according to algorithms, matrices A_i, B_i , coefficients d_j the values β_j are determined. The resulting model is specified at each step (see block diagram in Fig. 2). The optimizer 12 operates on the principle of predictive control with an inverse fuzzy model. In order to obtain optimal control effects in accordance with the obtained model, a minimum target function is found:

$$J(H_{p1}, H_{p2}, H_{pc}, \lambda) \approx \sum_{i=H_{p1}}^{H_{p2}} (y(k + i) - \hat{y}(k + i))^2 + \lambda_0 \sum_{i=1}^{H_c} \Delta v^2(k + i - 1),$$

where, $y(k + i)$ are the set values of output variables; $\hat{y}(k + i)$ are the output variable values predicted by the model; $\Delta v(k + i - 1)$ are the control actions determined from the condition of the minimum of the target function.

This considers the restrictions imposed on Δv , according to (7). Based on $\hat{y}(k + i)$, the predictive controller calculates the sequence of control impacts. The target function is quadratic, so the problem was considered as quadratic programming and solved using the simplex method. The resulting controls were applied to the object in order to obtain at the output of y_1 a consistently high value of the intermediate product output and at the output of y_2 a stable specified value of the iron content in the intermediate product. Using the simplex method in accordance with the requirements $Q_{int} \rightarrow \max, \beta_1 \leq \beta_{pr} \leq \beta_2$, we previously found the maximum performance $y_1 = Q_{pr}$ on the intermediate product with imposed restrictions on quality $52\% \leq y_2 \leq 55\%$.

The estimation of the quantity of the output product of a closed grinding cycle (discharge of a hydro cyclone) $Q(t)$ with a given particle size characteristic in the presence of disturbances in the inputs w and measurements v is shown in Fig 3. The results of $Q(t)$ prediction, obtained based on the developed hybrid fuzzy model are shown in Fig. 4. The standard deviation between accurate and formed estimates of the values of $Q(t)$ is 0.57.

The results of the research were implemented at the enterprises of the Kryvyi Rih iron ore basin, which are part of the Ukrudprom Association, which allows adequate structural and parametric identification of control objects (determination coefficient $R^2 \geq 0.96$, identification error is in the range 0.005–0.067). This made it possible to maximize the productivity of technological units, increase the content of the useful component in the concen-

trate by 0.15% and reduce energy consumption by 1.85%. Tests have shown that the use of control algorithms based on hybrid models reduces the variance of parameters (by more than 27%) and the duration of transients (by more than 22%).

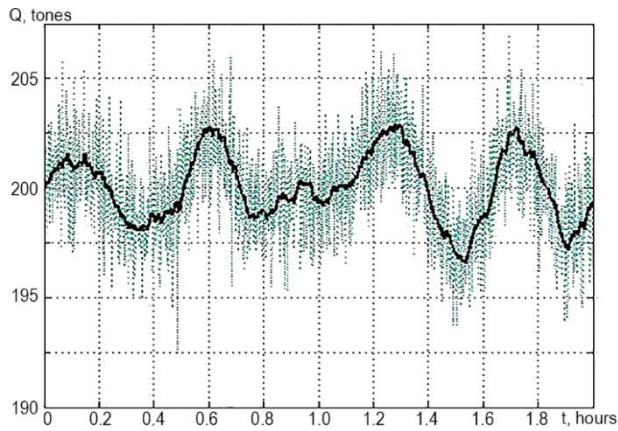


Fig. 3. Estimation of the quantity of the output product of a closed grinding cycle

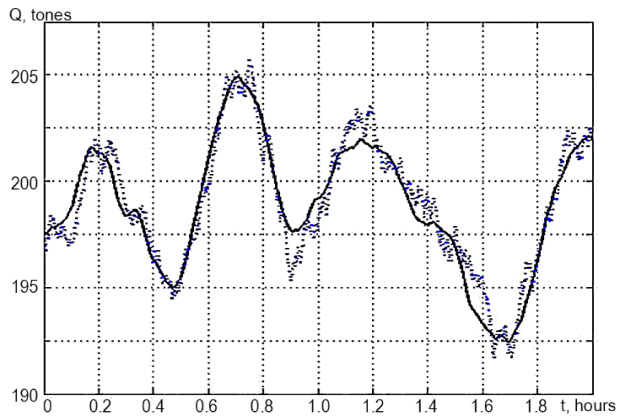


Fig. 4. The results of $Q(t)$ prediction, obtained based on a hybrid fuzzy model

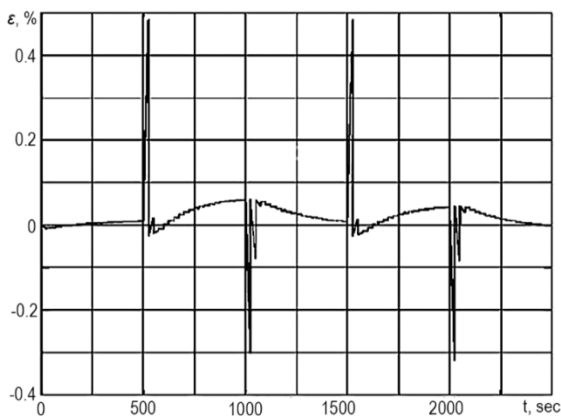


Fig. 5. The change in control error when changing the value of the setting of the ore grinding degree in the hydrocyclone discharge

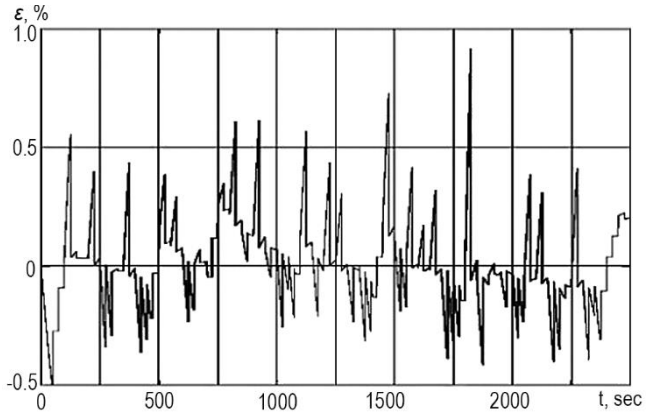


Fig. 6. Change of regulation error when changing the particle size distribution of the pulp solid phase in the mill discharge

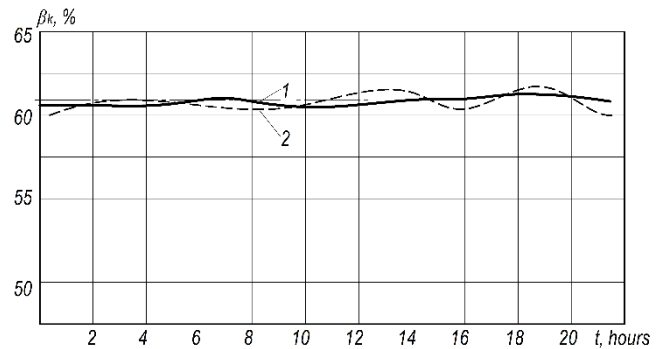


Fig. 7. Graphs of changes in the magnetic iron content in the intermediate product of the steady-state iron ore processing line:
 1 – the control system based on the Hammerstein hybrid model;
 2 – the control system with reconfigurable PID controllers

The effectiveness of the considered control system was evaluated concerning the hierarchical structure based on local automatic control systems with reconfigurable PID controllers and the calculation of optimal tasks for these systems. Figure 7 shows graphs of changes in the magnetic iron content in the intermediate product of the steady-state iron ore processing line.

Thus, the proposed algorithm based on the Hammerstein hybrid model ensures convergence of the procedure and ensures efficient control of the objects under consideration

5. CONCLUSIONS

1. Non-linear, dynamic, non-stationary properties characterize objects of the iron ore beneficiation line; therefore, it is advisable to use models of the Hammerstein class for their approximation. The hybrid model of Hammerstein, in which the non-linear block is represented by fuzzy Takagi-Sugeno models of zero and first order, built based on linguistic rules about the control object, makes it possible to visually and conveniently approximate the control object during magnetic beneficiation of iron ores. Therefore, it is advisable to use such models as predicting when controlling the beneficiation processes according to the principles of MPC in the context of incomplete and fuzzy information about the state of the control object.
2. The developed algorithms allow identification by automatically extracting information from a fuzzy knowledge base about the ore beneficiation process, which allows them to be used for

real-time identification. The proposed identification mechanisms based on Hammerstein's hybrid models allow us to avoid non-linear optimization with non-linear res, which greatly simplifies the process of model coefficients calculating. The restrictions imposed on the model parameters guarantee the convergence of the procedure.

3. The application of the model fuzzy block inversion in the synthesis of predictive control based on the Hammerstein hybrid model allows determining the prediction based on the linear model, which greatly simplifies the calculation of optimal control actions.
4. The proposed Hammerstein hybrid model makes it possible to consider the information of various mathematical classes for the implementation of adequate structural and parametric identification of the control objects of the beneficiation production (determination coefficient $R^2 \geq 0.96$. Depending on the dynamic characteristics of the object, the relative error of identification varies from 0.005 to 0.067; therefore, models allow the approximation of control objects with various dynamic properties, which are used at processing plants.

REFERENCES

1. **Abba S.I., Nourani V., Elkiran G.** (2019), Multi-parametric modeling of water treatment plant using AI-based non-linear ensemble, *Aqua*, 68 (7), 547–561.
2. **Abonyi J., Nagy L., Szeifert F.** (2000), Hybrid fuzzy convolution modelling and identification of chemical process systems, *International Journal of Systems Science*, 31, 457–466.
3. **Babuska R.** (1998), *Fuzzy Modeling for Control*, Kluwer Academic Publishers, Boston.
4. **Babuska R., Roubos J.A., Verbruggen H.B.** (1998), Identification of MIMO systems by input-output TS fuzzy models, *Proceedings FUZZ-IEEE'98, Anchorage, Alaska*, 57–69.
5. **Botto M. Ayala, van den Boom T.J.J., Krijgsman A., S'a da J.** (1999), Costa Constrained nonlinear predictive control based on input-output linearization using a neural network, *International Journal of Control*, 72(17), 1538–1554.
6. **Chen H., Ding F.** (2015), Hierarchical least-squares identification for Hammerstein nonlinear controlled autoregressive systems, *Circuits, Systems and Signal Processing*, 34(1), 61–75.
7. **Chen J., Wang X.** (2015), Identification of Hammerstein systems with continuous nonlinearity, *Information Processing Letters*, 115(11), 822–827.
8. **Clarke D. W., Tuffs P.S., Mothadi C.** (1989), Generalized predictive control – part I. the basic algorithm, *Automatica*, 23, 137–148.
9. **Clarke D.W., Mohtadi C.** (1989), Properties of generalized predictive control, *Automatica*, 25(6), 859–875.
10. **Falck T., Dreesen P., Brabanter K., Pelckmans K., De Moor B., Suykens J.A.K.** (2012), Least-Squares Support Vector Machines for the identification of Wiener–Hammerstein systems, *Control Engineering Practice*, 20(11), 1165–1174.
11. **Fruzetti K.P., Palazoglu A., McDonald K.A.** (1997), Nonlinear model predictive control using Hammerstein models, *Journal of Process Control*, 7(1), 31–41.
12. **Garcia C.E., Morari M.** (1982), Internal model control: 1.A unifying review and some new results, *Ind. Eng. Chem. Process Res. Dev.*, 21, 308–323.
13. **Ikhouane F., Giri F.** (2014), A unified approach for the parametric identification of SISO/MIMO Wiener and Hammerstein systems, *Journal of the Franklin Institute*, 351(3), 1717–1727
14. **Ivanov A.I.** (1991), *Ortogonalnaya identifikatsiya nelineynykh dinamicheskikh sistem s konechnoy i beskonechnoy pamyatyu pri odnom i neskol'kikh vkhodakh* [Orthogonal identification of nonlinear dynamical systems with finite and infinite memory at one or several inputs], NIKIRET, Penza (*In Russian*),
15. **Ivanov A.I.** (1995), *Bystryye algoritmy sinteza nelineynykh dinamicheskikh modeley po eksperimental'nym dannym* [Fast algorithms for the synthesis of nonlinear dynamic models from experimental data], NPF "Kristall", Penza (*In Russian*),
16. **Junhao Shi, Sun H.H.** (1990), Nonlinear system identification for cascaded block model: an application to electrode polarisation impedance, *IEEE Trans. Biomed. Eng.*, 6, 574–587.
17. **Kazuo T., Wang H.O.** (2001), *Fuzzy Control Systems Design And Analysis*, John Wiley&Sons.
18. **Le F., Markovsky I., Freeman C.T., Rogers E.** (2012), Recursive identification of Hammerstein systems with application to electrically stimulated muscle, *Control Engineering Practice*, 20(4), 386–396
19. **Leontaritis I.J. Billings S.A.** (1987), Experimental design and identifiability for nonlinear systems, *International Journal of Systems Science*, 18, 189–202.
20. **Li Yu., Shchetsen M.** (1968), *Opredeleniye yader Vinera-Khopfa metodom vzaimnoy korrelyatsii. Tekhnicheskaya kibernetika za rubezhom* [Determination of Wiener-Hopf kernels by cross-correlation. Technical cybernetics abroad], Mashinostroyeniye, Moscow (*In Russian*),
21. **Ma J., Ding F., Xiong W., Yang E.** (2016), Combined state and parameter estimation for Hammerstein systems with time-delay using the Kalman filtering, *International Journal of Adaptive Control and Signal Processing*, 00:1–17. DOI: 10.1002/acs
22. **Mete S., Ozer S., Zorlu H.** (2016), System identification using Hammerstein model optimized with differential evolution algorithm, *AEU - International Journal of Electronics and Communications*, 70(12), 1667–1675.
23. **Morkun V., Morkun N., Pikilnyak A.** (2014a), Ultrasonic phased array parameters determination for the gas bubble size distribution control formation in the iron ore flotation, *Metallurgical and Mining Industry*, 6(3), 28–31.
24. **Morkun V., Morkun N., Pikilnyak A.** (2014b), Ultrasonic facilities for the ground materials characteristics control, *Metallurgical and Mining Industry*, 6(2), 31–35.
25. **Morkun V., Morkun N., Pikilnyak A.** (2014c), The adaptive control for intensity of ultrasonic influence on iron ore pulp, *Metallurgical and Mining Industry*, 6, 8–11.
26. **Morkun V., Morkun N., Pikilnyak A.** (2015c), Adaptive control system of ore beneficiation process based on Kaczmarz projection algorithm, *Metallurgical and Mining Industry*, 2, 35–38.
27. **Morkun V., Morkun N., Tron V.** (2015a), Formalization and frequency analysis of robust control of ore beneficiation technological processes under parametric uncertainty, *Metallurgical and Mining Industry*, 5, 7–11.
28. **Morkun V., Morkun N., Tron V.** (2015b), Model synthesis of nonlinear nonstationary dynamical systems in concentrating production using Volterra kernel transformation, *Metallurgical and Mining Industry*, 10, 6–9.
29. **Morkun V., Morkun N., Tron V., Hryshchenko S.** (2018), Synthesis of robust controllers for the control systems of technological units as iron ore processing plants, *Eastern European Journal of Enterprise Technologies*, 1(2-91), 37–47.
30. **Morkun V., Tcvirkun S.** (2014), Investigation of methods of fuzzy clustering for determining ore types, *Metallurgical and Mining Industry*, 5, 11–14.
31. **Narendra K.S., Gallman P.G.** (1966), An iterative method for the identification of nonlinear systems using the Hammerstein model, *IEEE Trans. Automatic Control*, 12, 546.
32. **Ozer S., Zorlu H., Mete S.** (2016), System identification application using Hammerstein model, *Sadhana*, 41(6), 597–605.
33. **Piroddi L., Farina M., Lovera M.** (2012), Black box model identification of nonlinear input–output models: A Wiener–Hammerstein benchmark, *Control Engineering Practice*, 20(11), 1109–1118.
34. **Postlethwaite B.E.** (1996), Building a model-based fuzzy controller, *Fuzzy Sets and Systems*, 79, 3–13.

36. Rébillat M., Hennequin R., Corteel E., Katz B. (2010), Identification of cascade of Hammerstein models for the description of nonlinearities in vibrating devices, *Journal of Sound and Vibration*, 330(5), 1018–1038.
37. Rossiter J.A. (2003), *Model-Based Predictive Control: a Practical Approach*, CRC Press.
38. Sanches J.M.M., Rodellar J. (1996), *Adaptive predictive control: from the concepts to plant optimization*, Prentice Hall International (UK) Limited.
39. Sjöberg J., Zhang Q., Ljung L., Benveniste A., Deylon B., Glorennec P.-Y., Hjalmarsson H., Juditsky A. (1995), Nonlinear black-box modeling in system identification: a unified overview, *Automatica*, 31, 1691–1724.
40. Stoica P. (1981), On the convergence of an iterative algorithm used for Hammerstein system identification, *IEEE Trans. Automatic Control*, 26, 967–969.
41. Tobi T., Hanafusa T. (1991), A practical application of fuzzy control for an airconditioning system, *International Journal of Approximate Reasoning*, 5, 331–348.
42. Verhaegen M., Westwick D. (1996), Identifying MIMO Hammerstein systems in the context of subspace model identification, *International Journal of Control*, 63, 331–349.
43. Wills A., Ninness B. (2012), Generalised Hammerstein–Wiener system estimation and a benchmark application, *Control Engineering Practice*, 20(11), 1097–1108.
44. Young A.D. (1977), State of the art and trends in computers and control equipment, *2-nd IFAC Symp. "Automat. Mining, Miner. and Metal. Proc."*, Pretoria, 41–46.
45. Yucai Z. (1999), Parametric Wiener model identification for control, *Proceedings IFAC World Congress, Beijing, China*, 3a–02–1, 34–46.
46. Zubov D.A. (2006), *Passifikatsiya i sintez algoritma avtomaticheskogo upravleniya odnim klassom SISO-obyektov ugleobogashcheniya s ispolzovaniyem algebrы Li* [Passification and synthesis of an automatic control algorithm for one class of SISO objects for coal enrichment using Lie algebra], *Zbagachennya korisnikh kopalin*, 24(65), 80–87 (In Russian),

MODELLING METHODOLOGY OF PISTON PNEUMATIC AIR ENGINE OPERATION

Dariusz SZPICA,* Michal KORBUT*

*Faculty of Mechanical Engineering, Bialystok University of Technology, ul. Wiejska 45c, 15-351 Bialystok, Poland

d.szpica@pb.edu.pl, korbutmichal@gmail.com

received 16 December 2019, revised 16 January 2020, accepted 18 January 2020

Abstract: The article presents a mathematical model describing the operation of a piston pneumatic air engine. Compressed air engines are an alternative to classic combustion solutions as they do not directly emit toxic exhaust components. In the study, a modified internal combustion piston engine was adopted as pneumatic engine. The mathematical model was divided on the two subsystems, that is, mechanical and pneumatic. The mechanical subsystem describes a transformation of compressed air supply process parameters to energy transferred to the piston and further the conversion of the translational to rotary motion; in turn, in the pneumatic part, the lumped elements method was used. Calculations were carried out using the Matlab-Simulink software, resulting in the characteristics of external and economic indicators. The presented mathematical model can be ultimately developed with additional elements, such as the intake or exhaust system, as well as timing system control.

Key words: Mechanical engineering, drive sources, pneumatic engine, modelling

1. INTRODUCTION

In the subsequent years, the emission limits of the exhaust toxic components for the transport sector are successively reduced. The proposed *WLTP* (<http://wltfacts.eu/>) and *RDE* (Commission Regulation 2017/1154, 2017) driving tests necessitating the vehicles' producers' finding the new emission reduction methods. There are still non-road vehicles (Wargula et al., 2018) in case of which steps are taken to reduce their emission (Walus et al., 2018). In general, the European Union regulations indicate on the reduction of *GHG* by ca. 20% by 2030 compared to the emissions in 2008 (A policy framework for climate and energy..., 2014).

Many possible solutions of reducing the exhaust toxic components in the powertrains of transport means can be distinguished:

- a) The organisation of processes related to the operation of internal combustion engine:
 - *ATAC* (Onishi et al., 1979),
 - *CAI / HCCI* (Jeuland et al., 2004),
 - *HPDI* or *RCCI* (Mikulski et al., 2018),
 - usage of exhaust purification systems (Fox et al., 2019; Senthil Kumar et al., 2019; Resitoglu et al., 2020),
 - design changes,
 - more efficient control algorithms.
- b) Use of alternative energy sources:
 - for example, *LPG* or *CNG* (Raslavicius et al., 2014; Borawski, 2015; Pulawski and Szpica, 2015), biogas (Mikulski et al., 2015) and others,
 - electric drive (Grigor'ev et al., 2015),
 - hydraulic/pneumatic drive (Simon, 2017),
 - hybrid systems (Brejaud et al., 2011; Dimitrova and Marechal, 2015; Raslavicius et al., 2017).

Pneumatics drives used in road transport are not popular. Only MDi company (<https://www.mdi.lu/>) attempted to introduce a series of cars using the pneumatic engines in the powertrain system. The Engineair Company (<http://www.engineair.com.au/>) is conducting advanced researches on the efficiency improvements of the pneumatic engines. Pneumatic engines have many possible variants, that is, reciprocating, rotary, unconventional, for example, Di Pietro (Zwierzchowski, 2017). In many cases presented in the literature, the pneumatic engine is a modification of a two or a four stroke internal combustion engine (Mitianiec, 2008; Allam and Zakaria, 2018). The researches also concern vane (Badr et al., 1985; Librovich and Nowakowski, 2004) and rotary (Dvorak et al., 2017) engines.

Many studies can be found in the literature regarding the operation of the piston pneumatic engine (i.e., Michael et al. (2012), Kalekin et al. (2014), or Semenchukova et al. (2018), Fang et al. (2018)). In the mechanical part, the mathematical models are based on the description of a piston machine. The pneumatic part describes the air flow through the inlet and outlet valves and a variable volume chamber representing the cylinder. Dvorak et al. (2017) used a standard subsystems blocks from the Matlab environment in the course of the mathematical modelling, demonstrating the compatibility of model and experimental courses for the transition states of the rotary engines.

The modelling methods described above were based on the values averaged over a working cycle. It has become significant to indicate the variability of these values within one cycle, constituting the basis for further simulation or strength calculations of working elements. The study proposes a methodology for modelling an operation of the pneumatic piston engine combining two subsystems, mechanical and pneumatic. In the pneumatic part, it was proposed that the lumped element method be used (Kaminski, 2013; Kaminski 2014, Szpica, 2018b).

2. THE RESEARCH OBJECT

The object of the research was conceptual piston pneumatic air engines with the parameters presented in Table 1. The engine (Fig. 1a) was based on a JAWA 50 (<http://www.jawa-50.cz>) combustion engine, which was a 2-stroke unit with a gas exchange operated by the piston motion. The scope of the engine modification for compressed air supply included:

- the intake system in which the carburettor was removed and the intake channel was plugged (1 in Fig. 1b),
- in the spark plug place, the solenoid valve enabling cyclically air supply was mounted (2 in Fig. 1b),
- a custom plate was used between the cylinder head and the cylinder to lower the compression ratio (3 in Fig. 1c),
- a custom plate was mounted between the engine block and the cylinder for blocking the scavenging system operation (4 in Fig. 1c),

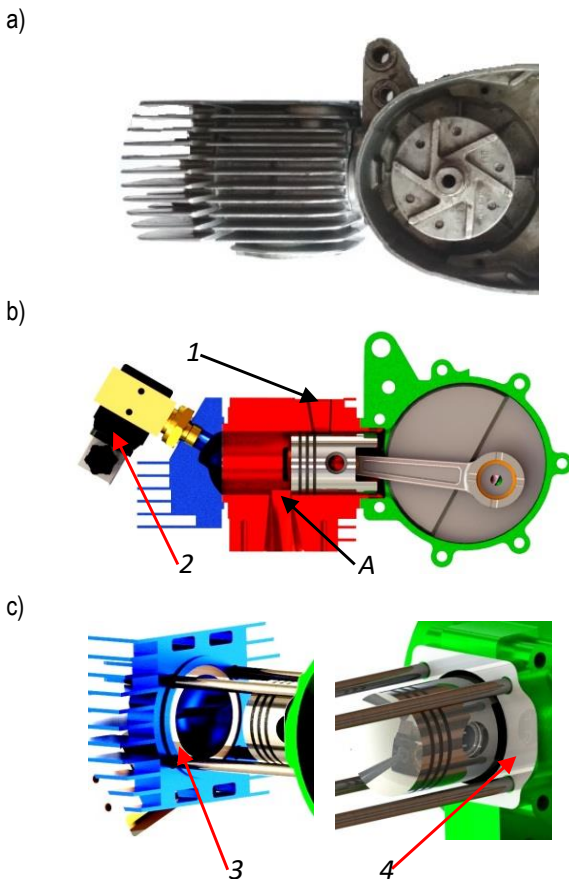


Fig. 1. Subject of the modelling: a – real view, b – CAD model, c – modifications (description in the main text)

The use of a custom plate 3 (Fig. 1b) was necessary as the engine with a base compression ratio of 9:1 could generate about $10e^5$ Pa at the end of the compression stroke. Initially, assuming a compressed air supply pressure value at $10e^5$ Pa, it would be tough to expect measurable engine energy effects. Hence, the decision to reduce the compression ratio. The custom plate 4 and plate 1 was used to block the operation of the crankcase as the pump pumping over the piston.

The modified engine works as a two-stroke engine, with the processes occurring only over the piston, without the crankcase involvement. As a result of the crankshaft rotation, the piston closes the outlet window (A in Fig. 1b) and the compression process starts. Close to the TDC, intake of the compressed air starts realized by solenoid valve 2. Compressed air is responsible for producing pressure force on the piston to create a crankshaft torque in a work stroke. The pressure generated in the crankcase is neutralised by the gearbox, which is originally locked to the engine. The holes between the engine crankcase and the gearbox, in addition to the neutralisation, provide the lubrication of the crankshaft bearings.

Tab. 1. The two stroke piston pneumatic air engine technical data

parameter	unit	value
number of cylinders	–	1
timing system (max. throughput): inlet	m ²	12.723e-6
	outlet	238.400e-6
displacement / volume	m ³	0.5479e-6
bore	m	40.000e-3
stroke	m	43.600e-3
connecting rod length	m	100.000e-3
compression ratio	–	4:1
weight of the components involved in the reciprocal motion	kg	0.142
substitute mass of the part of the connecting rod rotating on radius R of the x-th crank	kg	0.140

3. SIMULATION METHODOLOGY

The scheme presented in Fig. 2 was used for the model description.

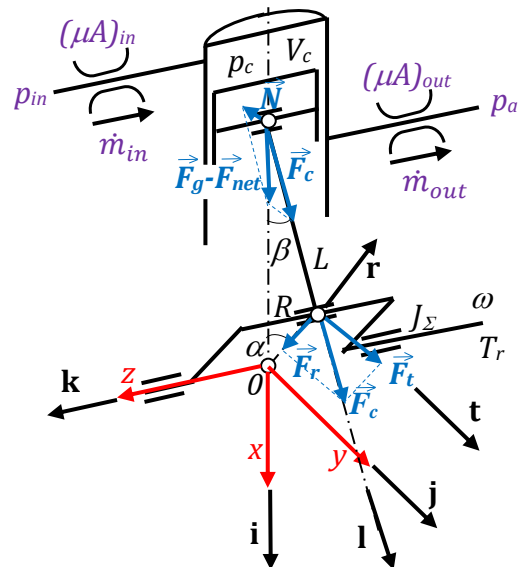


Fig. 2. Scheme of the mechanical and pneumatic subsystem (description in the main text)

The relevant assumptions for building the mathematical representation of both subsystems were as follows:

- a) mechanical subsystem:
- the torque transfer system was perfectly stiff,
 - the influence of elastic vibrations was omitted,
 - energy flow flowed without loss,
 - the pressure course depended on the timing and input and output pressure as well as the position of the piston,
 - the moment of inertia of the crankshaft and flywheel were omitted at angular velocity analysis.
- b) pneumatic subsystem:
- the air was regarded as a thermodynamically ideal gas, while being viscous and compressible,
 - the flow took place without internal friction and heat exchange with the surroundings,
 - the state of the air was constant in a given volume and depended on time,
 - the joints of the individual elements of the tested object were perfectly airtight,
 - the air properties were assumed to be uniform both in the local volume and in the entire cross-section of the flow through the local resistance,
 - the air temperature was constant in the process.

In the model description, two presented subsystems were combined, where as a result of the compressed air supply (replacement of the combustion, as it was in the original design), force was generated on the piston that created torque and engine speed. The engine load conditions determined filling and emptying of the cylinder.

In the description of the mechanical part, based on the scheme presented in Fig. 2 and Appendix, the general equation of the process in mechanical subsystem was:

$$\begin{bmatrix} \omega \\ T_r \end{bmatrix} = \begin{bmatrix} 0; & \left(RA_p (\sin \alpha + \frac{\lambda}{2} \sin 2\alpha) \right)^{-1} \\ \frac{RA_p \sin(\alpha+\beta)}{\cos \beta}; & -\frac{Rm_A \sin(\alpha+\beta)}{A_p \cos \beta} \end{bmatrix} \begin{bmatrix} p_c(\alpha) \\ \dot{V}_c(\alpha) \end{bmatrix} \quad (1)$$

In two stroke, one-cylinder engines that work cycle of which involves one full crankshaft revolution, the $S(\alpha)$ function for the one-cylinder engine was:

$$S(\alpha) = \frac{\sin(\alpha+\beta)}{\cos \beta} = \frac{\lambda \sin 2\alpha}{2-\lambda^2 \sin^2 \alpha} + \sin \alpha \quad (2)$$

The equation of engine torque was presented in the form:

$$T_r = RA_p S(\alpha) p_c(\alpha) - R^2 m_A S(\alpha) (\cos \alpha + \lambda \cos 2\alpha) \omega^2 \quad (3)$$

The engine torque calculated from Eq. 3 is the indicated engine torque. To obtain effective power, the mechanical efficiency of the system should be taken into consideration.

The description omits the influence of many factors, that is, friction, the coefficient of which can be determined using the methods presented in (Borawski, 2016; Borawski, 2019).

When the instantaneous torque is greater than the average one, the instantaneous speed increases, when is smaller – decreases. This is the result of the fact that mechanical work of the engine is equal with the increase in the kinetic energy accumulated in the rotating masses of the engine components. When we compared the work and the energy, we could calculate the instantaneous angular crankshaft speed:

$$\omega_i = \begin{cases} \sqrt{\omega_{i-1}^2 - \frac{2T_r \Delta \alpha}{J_E^\Sigma}}, & T_r \leq T_{mean} \\ \sqrt{\omega_{i-1}^2 + \frac{2T_r \Delta \alpha}{J_E^\Sigma}}, & T_r > T_{mean} \end{cases} \quad (4)$$

The mass moment of inertia of the rotating elements of the engine was:

$$J_E^\Sigma = 0.64 m_B R^2 \quad (5)$$

The main problem in the modelling processes was the determination of mean torque value T_{mean} in cycle, which depended directly on the supplying conditions and angular crankshaft speed ω . It was necessary to change the T_{mean} value in subsequent approximations, to get closer to the ω reference value.

Pressure in cylinder (Fig. 2 and Appendix) was described:

$$\frac{dp_c}{dt} = \frac{\kappa R_g T_g}{V_c} \left(\dot{m}_{in} - \dot{m}_{out} - \frac{p_c}{R_g T_g} \frac{dV_c}{dt} \right) \quad (6)$$

where:

$$\dot{m}_{in} = (\mu A)_{in} \frac{p_{in}}{\sqrt{R_g T_g}} \psi_{max} b \frac{p_{in}-p_c}{b p_{in}-p_c} \quad (7)$$

and

$$\dot{m}_{out} = (\mu A)_{out} \frac{p_c}{\sqrt{R_g T_g}} \psi_{max} b \frac{p_c-p_a}{b p_c-p_a} \quad (8)$$

because $p_{out} = p_a$.

4. NECESSARY PARAMETER TO INITIATE CALCULATION

To initiate the calculation, it was necessary to specify the input parameters that should be distinguished:

- inlet pressure: $p_{in} = 10e^5$ Pa,
- atmospheric pressure: $p_a = 1e^5$ Pa,
- air temperature: $T_g = 293.15$ K,
- adiabatic exponent: $\kappa = 1.4$,
- gas constant: $R_g = 287.15$ J/(kg K),
- max. value of the SVW function: $\psi_{max}(\sigma) = 0.578$,
- factor of the MA function: $b = 1.13$,
- throughput of the timing system: see Fig. 3 and Fig. 4.

The Inlet side flow characteristics were determined on the basis of the solenoid valves dynamical characteristics analysis, in this case LPG vapour phase pulse injector (Duk and Czarnigowski, 2012; Czarnigowski, 2012; Szpica, 2016). Initially, for the compressed air supply, the solenoid valve 2M-15 1/2" 0-16 bar 24 V with flow diameter $d_v = 4.5$ mm was provided. In this type of final control elements, specified inlet time t_{inlet} (Fig. 3 – throughput absolute values) consisted of: opening time t_o , time of full opening t_{fo} and closing time t_c . It follows that the inlet time must contain imperfections in the opening and closing process. The solenoid valve opening and closing process analysis allowed on describing the inlet process in three time dependent ranges:

$$\frac{(\mu A)}{(\mu A)_{max}}(t) = \begin{cases} \frac{1}{t_o^2} t^2, & 0 \leq t < t_o \\ 1, & t_o \leq t < t_o + t_{fo} \\ -\frac{1}{t_c^2} t^2 + 1, & t_o + t_{fo} < t \leq t_{inlet} \end{cases} \quad (9)$$

In the case of the solenoid valve supply, IVO can be implemented in any way in regard of the TDC . To increase the supply efficiency, the solenoid valve with piezoelectric actuator can be

used (Mieczkowski, 2017; Mieczkowski, 2018; Mieczkowski, 2019, Mieczkowski et al, 2020), which significantly reduce the opening and closing time if used in a double version.

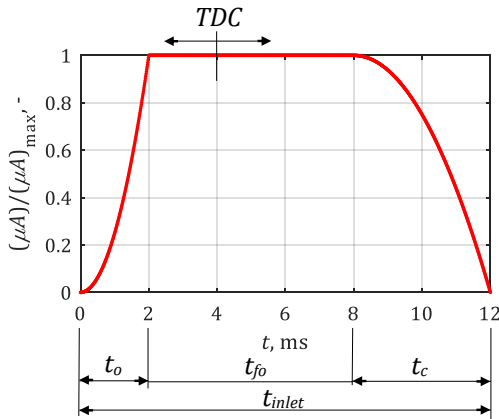


Fig. 3. Example course of the inlet process as a time function:
 $t_o = 2 \text{ ms}$, $t_c = 4 \text{ ms}$, $t_{fo} = 3 \text{ ms}$, $t_{inlet} = 12 \text{ ms}$

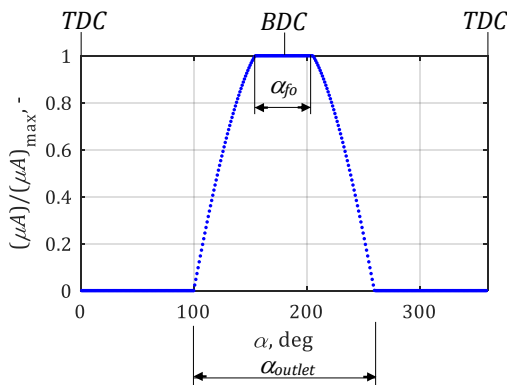


Fig. 4. Course of the outlet process as a crankshaft rotation angle function

To determine the course of the cylinder outlet port opening was used engine CAD model. After developing the outlet port surface, the change of the flow area cross section in a function of a crankshaft rotation angle was determined in absolute values of throughput, which is presented in Fig. 4. In this case, the opening is symmetrical relative to the BDC. The value of t_{fo} depended on the position of the bottom edge of the port relative to the BDC.

Boundary conditions of simulation for $t = 0 \text{ s}$ was established as:

- angle of crankshaft rotation: $\alpha = 0 \text{ rad}$,
- displacement of pistons: $x = 0 \text{ mm}$,
- volume of cylinder: combustion chamber $V_c = V_{\min}$,
- pressure in cylinder: depending on load conditions and rotational speed,
- timing system: $(\mu A)_{in}$ – depending on the adopted variant of analysis, $(\mu A)_{out} = 0 \text{ m}^2$ (Fig. 4),
- number of cycles analysing for determining the mean – 10.

5. RESULTS OF THE SIMULATION

The simulations were carried out using the Matlab-Simulink environment. The differential (Eq. 6) was solved numerically with

the implicit trapezoidal method combined with reverse differentiation (*ode23tb*, variable-step, max step size 0.0001, min step size *auto*). Solution Eq. 6 is obtained as a function of time t ; so, before starting the simulation, the angle increment α was calculated with a determined value ω . Knowing the angle increment α allowed the camshaft phases $(\mu A) = f(\alpha)$ to be loaded into the working space. To calculate T_r (Eq. 3), a value of $\alpha = f(t)$ and $p_c = f(\alpha)$ was required, which was obtained from (Eq. 6). With $T_r = f(\alpha)$ and T_{mean} , it was possible to calculate $\omega = f(\alpha)$ with Eq. 4.

At the beginning of the calculation, it is important to specify the initial pressure at the simulation start. It affects the shape of the indicator diagram. Examples of the indicator diagrams with different value of initial pressure in cylinder were shown in Fig. 5. The simulation initial pressure value should be corrected each time for load conditions and rotational speed.

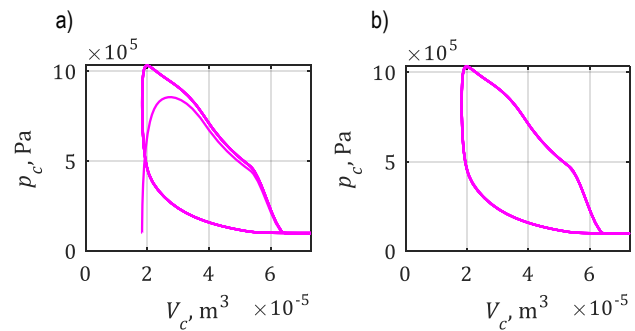


Fig. 5. Examples of the indicator diagrams: a – low pressure at the start of the simulation ($1e5 \text{ Pa}$), b – proper value of the pressure at the start of the simulation ($8e5 \text{ Pa}$)

In the next step, the determined mean load torque value T_{mean} should be approximated due to the fact that it has direct influence on the achieved angular speed. Therefore, the simulation is performed several times, for questing a compliance between the specified T_{mean} torque and the resulting mean torque from a certain number of cycles (crankshaft rotations). On this basis, the power could be calculated:

$$P = T_{mean} \omega = T_{mean} 2\pi n \quad (10)$$

where: $n = \omega/2\pi$.

and

$$BSAC = \dot{m}_{in}/P \quad (11)$$

For simulation initialization, into the program workspace should be loaded the courses of the inlet and outlet process as a function of crankshaft rotation (Fig. 6).

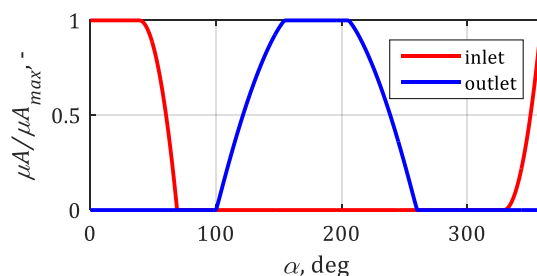


Fig. 6. Example courses of the inlet and outlet process as a crankshaft rotation ($n = 2000 \text{ rpm}$)

As a result of the calculations carried out, the courses of the inlet and outlet process $\mu A/\mu A_{max}$, pressure in cylinder p_c , torque T_r and rotation speed n as a time function were received (Fig. 7). The results are presented as a function of time t with regard to the specificity of solving Eq. 6, where pressure dp_c/dt is the determining factor for T_r and n . Fig. 7 presents the last 5 cycles out of the 10 performed due to the fact that there is a possibility of interference in the first cycles with inadequate selection of pressure p_{cstart} and T_{mean} . Significant rotational speed fluctuations can be observed resulting from *IVO*, and the assumption of only the mass m_B was the rotational inertia load (Eq. 5), without taking into account the crankshaft and flywheel mass moment of inertia.

The results presented in Fig. 7 were obtained with *IVO* = 30 deg *BTDC*, inlet time t_{inlet} equal to the 100 deg of a crankshaft rotate (control disc on a crankshaft with impulse transmitter for opening and closing), opening and closing time $t_o = t_c = 2.5$ ms. For adopted values and input courses, the values of mean torque $T_{mean} = 4.46$ Nm, rotational speed $n = 880$ rpm, power $P = 0.41$ kW and the stream of supplying air $\dot{m} = 0.053$ kg/s were obtained. Due to that, *BSAC* = 46.38 kg/(kWh).

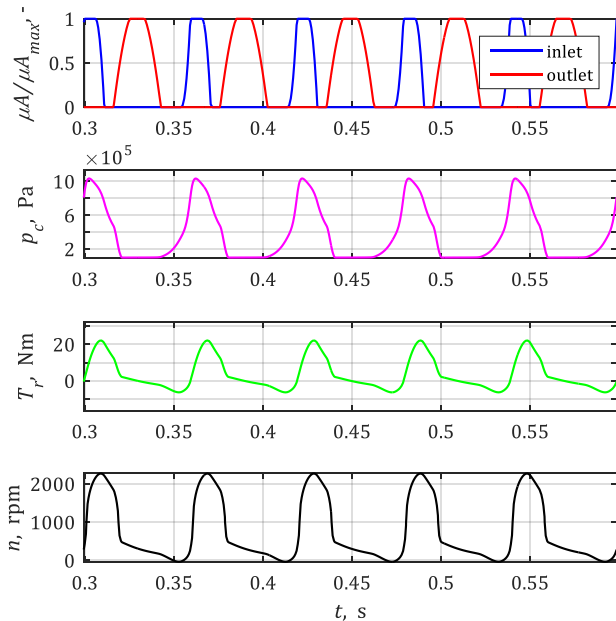


Fig. 7. Example calculation results

Using created calculation algorithm, the engine full load characteristics and performance were determined (Fig. 8) in relation to the energy and the economic indicators based on the indicated values. The shape of the characteristics is similar to the shape of the characteristics of internal combustion engines. The main difference consists of the rotational speed range, especially the lower value of speed in which the pneumatic engine is able to operate in situated below combustion engine possibility. The points of occurrence of the maximum torque T_{rmax} and the minimum *BSAC* occur on opposite sides of the characteristic, as in a combustion engine (Heywood, 1988). From around 2000 rpm is revealing a decrease in the mass stream of air supplying the engine $dm/dt = \dot{m}$. The assumed range of inlet valve opening angle seems to be correct, however, the operation of it is deter-

mined by the opening time t_o and closing time t_c , which at higher speeds often do not allow to achieve full opening.

In order to compare a pneumatic engine and its basing combustion engine, it is necessary to take into account the mechanical efficiency, for which the values for internal combustion piston engines are in the range $\eta_m = 0.80 \dots 0.92$ (Heywood, 1988) and can be taken as reference value for pneumatic engines. In the calculations, it was assumed $\eta_m = 0.85$. Statement of the energetic indicators is presented in Table 2. The maximum computational power of the pneumatic engine is 50% lower than the basic combustion variant. In turn, the maximum torque is 30% higher. In the case of torque, the decisive factor is the rotation speed, which is nearly 3 times lower than in the combustion equivalent. The pneumatic engine from 4000 rpm is characterized by a significant decrease in energy indicators.

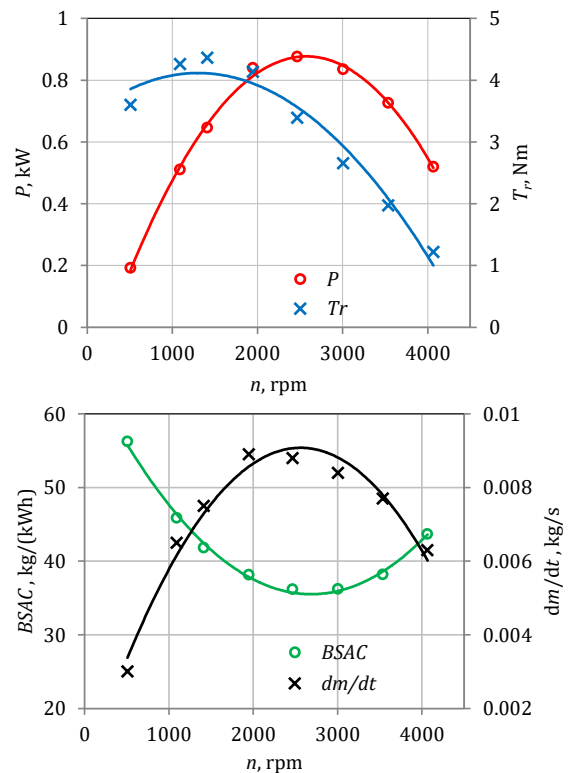


Fig. 8. Full load pneumatic engine speed characteristics

Tab. 2. The combustion and pneumatic engine comparison

parameter	combustion	pneumatic
maximum power	1.49 kW	0.78 kW
rotation speed of the maximum power	6500 rpm	2467 rpm
maximum torque	2.85 Nm	3.71 Nm
rotation speed of the maximum torque	4500 rpm	1413 rpm

The mathematical model presented in the study was used to determine the engine full load characteristics and performance. It is possible to use it in regulatory characteristics such as the impact of *IVO*, t_{inlet} or p_{in} on T_r or *BSAC*. At present, a prototype of the piston pneumatic engine proposed in the study was built. Work is underway to verify the mathematical model in relation to the real object, what will be the subject of subsequent publications.

6. CONCLUSIONS

The study presents a mathematical model of a piston pneumatic air engines. As a research object, a two-stroke JAWA 50 combustion engine was selected, which has been subjected to the necessary modifications to enable compressed air supply. In the scope of the simplifications adopted, engine modelling was divided into two sub-subsystems: mechanical, which described the transformation of compressed air energy into reciprocating machine torque, and pneumatic, where lumped elements method was used. The connecting part of both subsystems was the engine cylinder, which on the one hand determined the generated torque and speed, however, its filling and emptying was a result of the timing system. Carried out calculations allowed the assessment of the engine parameters within one working cycle. Significant torque and speed fluctuations have been indicated as a result of the low filling frequency and operation setting of the inlet valve operation. As a result, the engine full load characteristics and performance were determined. The maximum computational power of a pneumatic engines is 50% lower than the basic combustion variant. In turn, the maximum torque is 30% higher. In the case of torque, the decisive factor is the rotation speed, which is nearly 3 times lower than in the combustion equivalent. The pneumatic engines from 4000 rpm is characterized by a significant decrease in energy indicators. The structure of the presented mathematical model and calculation methodology allow to use it in the initial assessment of the impact of selected input parameters of the pneumatic and mechanical system on both, the energy and the economic external indicators.

Nomenclature: ATAC – Active Thermo-Atmosphere Combustion, BDC – Bottom Dead Centre, BTDC - Before TDC, BSAC – Brake-Specific Air Consumption, CAD – Computer Aided Design, CAI – Controlled Auto-Ignition, CNG – Compressed Natural Gas, GHG – GreenHouse Gas, HCCI – Homogeneous Charge Compression Ignition, HPDI – High Pressure Direct Injection, IVO – Inlet valve opening, LPG – Liquefied Petroleum Gas, MA – Metlyuk-Avtushko, RCCI – Reactivity Controlled Compression Ignition, RDE – Real Driving Emissions, SVW – St'Veinant and Wantzel, TDC – Top Dead Centre, WLTP – World Harmonized Light Vehicle Test Procedure.

Glossary: a – acceleration, A_p – piston area, b – constant parameter value of MA flow function, F_c – force acting in the connecting rod axis, F_g – gas force acting on the piston, F_{net} – resistance force of mass inertia in reciprocating motion, F_t – the force tangent to the crank radius, \dot{V} – rate of change in volume, V_c – volume of cylinder, m_A – weight of the components involved in the reciprocal motion, m_B – the substitute mass of the part of the connecting rod rotating on radius R of the x -th crank, L – the length of the connecting rod, p – pressure, R – the crank radius, R_g – gas constant, T_g – air temperature, V – volume, x – displacement of pistons.

Greek symbols: α – the angle of crankshaft rotation, κ – adiabatic exponent, λ – the connecting rod coefficient, (μA) – throughput, σ – pressure ratio, $\psi(\sigma)$ – dimensionless function of flow.

Indexes: c – closing, f – full, $inlet$, in – inlet, max – maximum volume, o – opening, $outlet$, out – outlet.

APPENDIX

A1. MECHANICAL SUBSYSTEM

The displacement of the piston without taking in account displacement of the cylinder axis related to the crankshaft axis was presented in the form (Szpica, 2018a):

$$x = R[(1 - \cos \alpha) + \frac{\lambda}{4}(1 - \cos 2\alpha)]$$

where: $\lambda = L/R$.

The movement of the piston was described by vector equation:

$$\vec{F}_g + \vec{F}_c + \vec{N} = m_A \vec{a}$$

where: $\vec{F}_g = p_c(\alpha)A_p \mathbf{i}$, $\vec{F}_c = \frac{F_g - F_{net}}{\cos \beta} \mathbf{i}$, $\vec{F}_{net} = -m_A \ddot{x}$, $\alpha = \dot{x} = \frac{D\dot{V}_c}{A_p}$, \mathbf{i} and \mathbf{l} – see Fig. 2.

Engine torque is described:

$$\vec{T}_r = \vec{R} \times \vec{F}_t = (\mathbf{r} \times \mathbf{t})(F_g + F_{net}) \frac{R \sin(\alpha + \beta)}{\cos \beta}$$

Because $\mathbf{r} \times \mathbf{t} = -\mathbf{k}$:

$$\vec{T}_r = -R(F_g + F_{net}) \frac{\sin(\alpha + \beta)}{\cos \beta} \mathbf{k}$$

where: \mathbf{k} – see Fig. 2.

$$T_r = \frac{RA_p \sin(\alpha + \beta)}{\cos \beta} p_c(\alpha) - \frac{Rm_A \sin(\alpha + \beta)}{A_p \cos \beta} \dot{V}_c(\alpha)$$

A2. PNEUMATIC SUBSYSTEM

Having considered the above assumptions, the stream of air flowing through the local drag was expressed as (Fig. 2) (Kaminski, 2013, Kaminski 2014, Szpica, 2018b):

$$\dot{m} = \frac{dm}{dt} = (\mu A) \frac{p}{\sqrt{R_g T_g}} \psi_{max} \psi(\sigma)$$

The air pressure change in the lumped elements with a variable volume V was described:

$$\frac{dp}{dt} = \frac{\kappa R_g T_g}{V} \left(\dot{m} - \frac{p}{R_g T_g} \frac{dV}{dt} \right)$$

The dimensionless two-range SVW flow function was inconvenient during the modelling, hence the single-range MA hyperbolic function (Szpica, 2018c) $\psi(\sigma) b \frac{1-\sigma}{b-\sigma}$, where $\sigma = p_{in}/p_{out}$.

REFERENCES

1. A policy framework for climate and energy in the period from 2020 to 2030. 2014. *Communication From The Commission To The European Parliament, The Council, The European Economic And Social Committee And The Committee Of The Regions*.
2. Allam S., Zakaria M. (2018), Experimental investigation of compressed air engine performance, *International Journal of Engineering Inventions*, 7(1), 13–20.
3. Badr O., Probert S.D., O'Callaghan P.W. (1985), Multi-vane expanders: internal-leakage losses, *Applied Energy*, 20(1), 1–46.
4. Borawski A. (2015), Modification of a fourth generation LPG installation improving the power supply to a spark ignition engine, *Eksploatacja i Niezawodnosc – Maintenance and Reliability*, 17(1), 1–6.

5. **Borawski A.** (2016), Suggested research method for testing selected tribological properties of friction components in vehicle braking systems, *Acta Mechanica et Automatica*, 10(3), 223–226.
6. **Borawski A.** (2019), Common methods in analysing the tribological properties of brake pads and discs – a review, *Acta Mechanica et Automatica*, 13(3), 189–199.
7. **Brejaud P., Higelin P., Charlet A. et al.** (2011), Convective Heat Transfer in a Pneumatic Hybrid Engine, *Oil & Gas Science and Technology*, 66(6), 1035–1051.
8. Commission Regulation (EU) 2017/1154 of 7 June 2017 amending Regulation (EU) 2017/1151 supplementing Regulation (EC) No 715/2007 of the European Parliament and of the Council on type-approval of motor vehicles with respect to emissions from light passenger and commercial vehicles (Euro 5 and Euro 6) and on access to vehicle repair and maintenance information, amending Directive 2007/46/EC of the European Parliament and of the Council, Commission Regulation (EC) No 692/2008 and Commission Regulation (EU) No 1230/2012 and repealing Regulation (EC) No 692/2008 and Directive 2007/46/EC of the European Parliament and of the Council as regards real-driving emissions from light passenger and commercial vehicles (Euro 6), *Official Journal of the European Union*, L175, 7.7.2017, page 708.
9. **Czarnigowski J.** (2012), *Teoretyczno-empiryczne studium modelowania impulsowego wtryskiwacza gazu*, Politechnika Lubelska, Lublin.
10. **Dimitrova Z., Marechal F.** (2015), Gasoline hybrid pneumatic engine for efficient vehicle powertrain hybridization, *Applied Energy*, 151, 168–177.
11. **Duk M., Czarnigowski J.** (2012), The method for indirect identification gas injector opening delay time, *Przegląd Elektrotechniczny*, 88(10b), 59–63.
12. **Dvorak L., Fojtasek K., Rehacek V.** (2017), Calculations of parameters and mathematical model of rotary air motor, *EPJ Web of Conferences*, 143, 02018, 4p.
13. **Fang Y.D., Lu Y.J., Yu X.L., Roskilly A.P.** (2018), Experimental study of a pneumatic engine with heat supply to improve the overall performance, *Applied Thermal Engineering*, 134, 78–85.
14. **Fox J.T., Yang K., Hunsicker R.** (2019), Diesel Particulate Filter Cleaning Effectiveness: Estimated Ash Loading, Quantified Particulate Removal, and Post-cleaning Filter Pressure Drop. *Emission Control Science and Technology*, 1–11 (on-line).
15. **Grigor'ev M.A., Naumovich N.I., Belousov E.V.** (2015), A traction electric drive for electric cars, *Russian Electrical Engineering*, 86(12), 731–734.
16. **Heywood B.H.** (1988), *Internal combustion engine fundamentals*, McGraw-Hill Series in Mechanical Engineering, New York, USA.
17. <http://wtpfacts.eu/> [online cit.: 2019.11.10].
18. <http://www.engineair.com.au/> [online cit.: 2019.11.10].
19. <http://www.jawa-50.cz/clanek/jawa-23-mustang-technicke-udaje.html> [online cit.: 2019.11.10].
20. <https://www.mdi.lu/> [online cit.: 2019-03.01].
21. **Jeuland N., Montagne X., Duret P.** (2004), New HCCI/CAI combustion process development: Methodology for determination of relevant fuel parameters, *Oil & Gas Science and Technology*, 59(6), 571–579.
22. **Kalekin V.S., Kalekin D.V., A. N. Nefedchenko A.N.** (2014), A Mathematical Model of a Piston Pneumatic Engine with Self-Acting air Distribution, *Chemical and Petroleum Engineering*, 50(1-2), 91–98.
23. **Kaminski Z.** (2013), Experimental and numerical studies of mechanical subsystem for simulation of agricultural trailer air braking systems, *International Journal of Heavy Vehicle System*, 20(4), 289–311.
24. **Kaminski Z.** (2014), Mathematical modelling of the trailer brake control valve for simulation of the air brake system of farm tractors equipped with hydraulically actuated brakes, *Eksplotacja i Niezawodność – Maintenance and Reliability*, 16(4), 637–643.
25. **Librovich B.V., Nowakowski A.F.** (2004), Analysis, design, and modeling of a rotary vane engine (RVE), *Journal of Mechanical Design*, 126(4), 711–720.
26. **Michael M., Voser C., Onder C et al.** (2012), Design methodology of camshaft driven charge valves for pneumatic engine starts, *IFAC Proceedings*, 45(30), 33–40.
27. **Mieczkowski G.** (2017), The constituent equations of piezoelectric cantilevered three-layer actuators with various external loads and geometry, *Journal of Theoretical and Applied Mechanics*, 55(1), 69–86.
28. **Mieczkowski G.** (2018), Optimization and prediction of durability and utility features of three-layer piezoelectric transducers, *Mechanika*, 24(3), 335–342.
29. **Mieczkowski G.** (2019), Criterion for crack initiation from notch located at the interface of bi-material structure, *Eksplotacja i Niezawodność – Maintenance and Reliability*, 21(2), 301–310.
30. **Mieczkowski G., Borawski A., Szpica D.** (2020), Static electromechanical characteristic of a three-layer circular piezoelectric transducer, *Sensors*, 20, 222, 14p.
31. **Mikulski M., Balakrishnan P.R., Doosje E. et al.** (2018), Variable Valve Actuation Strategies for Better Efficiency Load Range and Thermal Management in an RCCI Engine, *SAE Technical Papers*, 2018-01-0254, 14p.
32. **Mikulski M., Wierzbicki S., Pietak A.** (2015), Numerical studies on controlling gaseous fuel combustion by managing the combustion process of diesel pilot dose in a dual-fuel engine, *Chemical and Process Engineering - Inżynieria Chemiczna i Procesowa*, 36 (2), 225–238.
33. **Mitianiec W.** (2008), Pneumatic two-stroke engine as an alternative power source, *Journal of KONES Powertrain and Transport*, 15(3), 357–366.
34. **Onishi S., Hong J.S., Do J.S. et al.** (1979), Active thermo-atmosphere combustion (A.T.A.C.) - A new combustion process for internal combustion engines, *SAE Paper 790501*.
35. **Pulawski G., Szpica D.** (2015), The modelling of operation of the compression ignition engine powered with diesel fuel with LPG admixture, *Mechanika*, 21(6), 501–506;
36. **Raslavicius L., Kersys A., Makaras R.** (2017), Management of hybrid powertrain dynamics and energy consumption for 2WD, 4WD, and HMMWV vehicles, *Renewable and Sustainable Energy Reviews*, 68(1), 380–396.
37. **Raslavicius L., Kersys A., Mockus S. et al.** (2014), Liquefied petroleum gas (LPG) as a medium-term option in the transition to sustainable fuels and transport, *Renewable & Sustainable Energy Reviews*, 32, 513–525.
38. **Resitoglu I.A., Altinisik K., Keskin A. et al.** (2020), The effects of Fe₂O₃ based DOC and SCR catalyst on the exhaust emissions of diesel engines, *Fuel*, 262, 116501.
39. **Semenchukova V., Grishin Y., Malastowski N.** (2018), Mathematical modeling of a piston engine pneumatic start, *International Russian Automation Conference (RusAutoCon)*, 1–4.
40. **Senthil Kumar J., Ramesh Babu B.R., Sivasaravanan S. et al.** (2019), Experimental studies on emission reduction in DI Diesel engine by using nano catalyst coated catalytic converter, *International Journal of Ambient Energy*, 1–17 (on-line).
41. **Simon M.** (2017), Pneumatic vehicle, research and design, *Procedia Engineering*, 181, 200–205.
42. **Szpica D.** (2016), The influence of selected adjustment parameters on the operation of LPG vapor phase pulse injectors, *Journal of Natural Gas Science and Engineering*, 34, 1127–1136.
43. **Szpica D.** (2018a), Modelling of the operation of a Dual Mass Flywheel (DMF) for different engine-related distortions, *Mathematical and Computer Modelling of Dynamical Systems*, 24(6), 643–660.
44. **Szpica D.** (2018b), Research on the influence of LPG/CNG injector outlet nozzle diameter on uneven fuel dosage, *Transport*, 33(1), 186–196.
45. **Szpica D.** (2018c), The determination of the flow characteristics of a low-pressure vapor-phase injector with a dynamic method, *Flow Measurement and Instrumentation*, 62, 44–55.

46. **Walus K.J., Wargula L., Krawiec P. et al.** (2018), Legal regulations of restrictions of air pollution made by non-road mobile machinery - the case study for Europe: a review, *Environmental Science and Pollution Research*, 25(4), 3243–3259.
47. **Wargula L., Walus K. J., Krawiec P.** (2018), Small engines spark ignited (SI) for non-road mobile machinery-review, *Proceedings of 22nd International Scientific Conference. Transport Means 2018*, T.2, 585–591.
48. **Zwierzchowski J.** (2017), Design type air engine Di Pietro, *EPJ Web Conf.*, 143 02149.

The research has been carried out within work no. S/WMM/1/18 realized at Bialystok University of Technology and financed from the funding allocated for science by the Ministry of Science and Higher Education, Poland.